Nanoparticulate Cathode Films for Low Temperature Solid Oxide Fuel Cells

Vom Fachbereich Material- und Geowissenschaften
der Technischen Universität Darmstadt

zur Erlangung des akademischen Titels
Doktor-Ingenieur (Dr.-Ing.)

genehmigte Dissertation von
MSc. Azad Jaberi Darbandi
aus Teheran

Referent:	Prof. Dr.-Ing. Horst Hahn
Koreferent:	Prof. Dr. Christina Roth
Tag der Einreichung:	27. März 2012
Tag der mündlichen Prüfung:	29. Mai 2012

Darmstadt 2012
D17

CONTENTS

LIST OF FIGURES

List of Tables

Chapter one

1 Introduction

New energy resources with comparable effectiveness as fossil energy carriers have achieved increasing interest over the last decades. In order to become less dependent on fossil fuels the search for new or improved, highly efficient and sustainable energy conversion systems is ongoing. High temperature electrochemical devices such as solid oxide fuel cells (SOFC) are ambitious technologies with the potential to fulfill these requirements. Fuel cells are energy conversion devices in which a fuel (e.g. hydrogen, synthetic gas, methane) and an oxidant (e.g. air, oxygen) react in order to produce electrical energy and heat. Except for the chemical reaction products (e.g. water in the case of hydrogen as fuel and oxygen as oxidant or additionally CO_2 when carbon-containing fuels are utilized) there are no further by-products. Therefore, fuel cells are regarded as a pollution-free energy conversion device for the future. Compared to the thermo-mechanical energy conversion processes which are used nowadays fuel cells are very efficient (up to 60% efficiency in conjunction with steam turbines) since they are not subject to the Carnot-limitation. On the other hand, miniaturized type of SOFCs, well-known as Micro-SOFCs are anticipated for battery replacement and should enter the market for power supplies for small electronic equipment, such as portable phones, laptops and electronic handhelds. These devices are predicted to have a 3-4 times higher energy density and specific energy than traditional Ni-metal hydride and Li-ion batteries.

Typical operating temperatures for current thick-film-based two-chamber SOFCs are 800 – 1000 °C since the system kinetics are mostly thermally activated. The high temperature puts heavy demands on the materials and complicates the sealing mechanism. Therefore, current research is focused towards lowering the operating temperature down to 500 – 600 °C.

Consequently, the general trend in solid oxide fuel cell research leads to lower operating temperatures in order to reduce degradation phenomena due to reactions between adjacent cell components and sealing problems. Since the system kinetics are mostly thermally activated lower temperatures introduce severe problems regarding the overall efficiency of the SOFC system. The cathode material is known to limit the overall system performance and therefore research focuses on the development of new cathode materials with similar or even superior properties such as electrical conductivity, electrochemical activity, and oxygen exchange properties even at lower temperatures. Thus, the high efficiency compared to standard thermo-mechanical energy conversion processes could be kept or even be improved. This would be a small step towards sustainable and highly efficient energy conversion systems which are quiet and pollution-free.

The aim of this thesis is the realization of nanoparticulate (nanocrystalline and nanoporous) thin film cathodes for solid oxide fuel cells in order to study the highest achievable electrochemical activity by nanostructuring the cathode architecture. This includes identification, development and understanding of a suitable process for fabrication of thin film cathodes that is compatible with SOFC fabrication and considers production costs and technical feasibility. The cathodes need to be characterized in terms of structure, microstructure and electrochemical performance in the temperature range applicable for SOFCs (500–800°C).

Chapter two

2 Basics

2.1 Fuel Cells

A fuel cell can be described as an energy converter which takes fuel as an input and produces electricity. As long as fuel is supplied a fuel cell will continue to generate electricity. This is the main difference between a fuel cell and a battery. Although both rely on electrochemistry to generate electricity, a fuel cell is not consumed when it produces electricity. It is rather a generator which transforms the chemical energy stored in a fuel into electrical energy.

With this description, combustion engines are also chemical factories. Combustion engines also take the chemical energy stored in a fuel and transform it into useful mechanical or electrical energy. However, in a combustion engine, fuel is burned, releasing heat. The simplest example of the combustion of hydrogen as be considered as following:

$$H_2 + \frac{1}{2}O_2 = H_2O \qquad 2.1$$

On the molecular scale, atomic level collisions between hydrogen molecules and oxygen molecules result in a reaction. The hydrogen molecules are oxidized, producing water, and releasing heat.

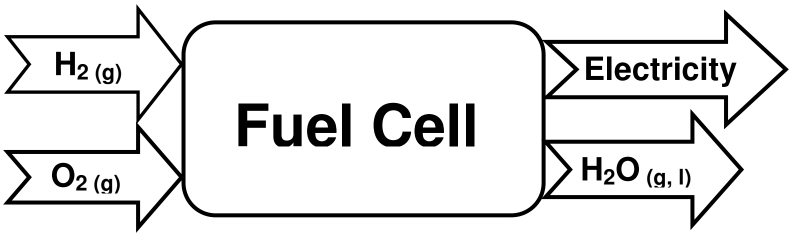

Figure 2-1: General concept of hydrogen / oxygen fuel cell.

At the atomic scale, in a scale of picoseconds, hydrogen-hydrogen bonds and oxygen-oxygen bonds are broken, while hydrogen-oxygen bonds are formed. Formation or splitting of these bonds results in transfer of electrons between the molecules. The energy of the bond configuration of the product (water) is lower than the bond configurations of the initial hydrogen and oxygen gases. This difference is released as heat. Although the energy difference between the initial and final states occurs by a reconfiguration of electrons as they move from one bonding state to another, this energy is recoverable only as heat because the bonding reconfiguration occurs in picoseconds at an intimate sub-atomistic scale. In order to produce electricity, this heat energy must be converted into mechanical energy, and then into electrical energy. Each stage of energy conversion is associated with loss of energy [1].

A more efficient solution is to produce electricity directly from the chemical reaction by using the electrons as they move from high-energy reactant bonds to low-energy product bonds. In principle, that is exactly how a fuel cell works. In a fuel cell the electron reconfigurations which are occurring in picoseconds at sub-atomic length scales occur by spatial separation of the hydrogen and oxygen reactants, so that the electron transfer is necessary to complete the bonding reconfiguration. This occurs over an extended length scale. Therefore, since the electrons move from the fuel species to the oxidant species, they represent an electrical current. In a fuel cell, the hydrogen combustion reaction is split into two electrochemical half reactions:

$$H_2 \leftrightarrow 2H^+ + 2e^- \qquad 2.2$$

$$\frac{1}{2}O_2 + 2H^+ + 2e^- \leftrightarrow H_2O \qquad 2.3$$

By spatially separating these reactions, the electrons transferred from the fuel are forced to flow through an external circuit (thus constituting an electric current) and do useful work before they can complete the reaction.

2.2 Fuel Cell Generalities

Advantages of fuel cells

Since fuel cells produce electricity as long as they are supplied with fuel, they share some characteristics in common with combustion engines. On the other side fuel cells are electrochemical energy conversion devices that rely on electrochemistry and they share some characteristics in common with batteries. In fact, fuel cells combine many of the advantages of both engines and batteries, while retaining few disadvantages of both. As fuel cells produce electricity directly from chemical energy, they are often far more efficient than combustion engines. Fuel cells are generally all solid state and mechanically ideal (no moving parts). This can result in highly reliable and long-lasting systems. This also means that fuel cells are silent. Because combustion is avoided, NO_x, SO_x, and particulate emissions are virtually zero. Unlike batteries, fuel cells allow easy independent scaling between power (determined by the fuel cell size) and capacity (determined by the fuel reservoir size). In batteries, power and capacity are often convoluted. Batteries scale poorly at large sizes while fuel cells scale well from the 1W range (cell phone) to the MW range (power plant). Fuel cells offer potentially higher energy densities compared to batteries, and can be instantly recharged by refueling, while batteries must be thrown away or plugged in for a time-consuming recharge.

Disadvantages of fuel cells

Currently, fuel cell technology's single greatest disadvantage is cost. After cost, fuel availability and storage are the next greatest problems. Fuel cells work best on hydrogen gas, a fuel which is not widely available, has a low volumetric energy density, and is difficult to store. Use of alternative fuels as hydrogen carriers (e.g. methane, methanol, formic acid) is limited by lower performance and increased requirements for equipment. Additional problems include operational temperature compatibility concerns, susceptibility to environmental poisons, and durability under start/stop cycling.

Fuel Cell Types

There are five major types of fuel cells, differentiated from one another by their electrolyte:

1. Solid Oxide Fuel Cell (SOFC)
2. Molten Carbonate Fuel Cell (MCFC)
3. Phosphoric Acid Fuel Cell (PAFC)
4. Alkaline Fuel Cell (AFC)
5. Polymer Electrolyte Membrane Fuel Cell (PEMFC)

While all five fuel cell types are based upon the same underlying electrochemical principles, they all operate at different temperature regimes, incorporate different materials, and often differ in terms of their fuel tolerance and performance characteristics, as shown in Table 2-1. The research presented in this thesis addresses Solid Oxide fuel cells (SOFCs). Therefore, all further background discussion in this thesis will be restricted to SOFCs.

Table 2-1: All five fuel cell types and the typical operating temperatures and materials

	PEFC	AFC	PAFC	MCFC	SOFC
Electrolyte	Ion Exchange Membranes	Mobilized or Immobilized Potassium Hydroxide	Immobilized Liquid Phosphoric Acid	Immobilized Liquid Molten Carbonate	Ceramic
Operating Temperature	80°C	65-220°C	205°C	650°C	600-1000°C
Charge Carrier	H^+	OH^-	H^+	$CO3^-$	O^-
External Reformer for CH_4	Yes	Yes	Yes	No	No
Prime Cell Components	Carbon-Based	Carbon-Based	Graphite-Based	Stainless-Based	Ceramic
Catalyst	Platinum	Platinum	Platinum	Nickel	Perovskite
Product Water Management	Evaporative	Evaporative	Evaporative	Gaseous Product	Gaseous Product
Product Heat Management	Process Gas+ Independent Cooling Medium	Process Gas + Electrolyte Circulation	Process Gas+ Independent Cooling Medium	Internal Reforming+ Process Gas	Internal Reforming + Process Gas

Solid Oxide Fuel Cell (SOFC)

2.2.1.1 Principle of operation

As schematically shown in Figure 2-2, a SOFC consists of three active layers: an air electrode (cathode), an electrolyte and a fuel electrode (anode). In a SOFC, all three layers contain ceramic materials, except for the anode which is a composite material consisting of ceramic and metal (cermet). Air enters at the cathode side, where the oxygen molecules are reduced to oxygen ions [2] [3] [4, 5]:

$$O_2 + 2e^- \rightarrow \tfrac{1}{2}O^{2-} \tag{2.4}$$

Usually, the cathode is porous to allow gas access and is catalytically active towards reduction of oxygen; furthermore it is capable of conducting electrons and preferably also ions. The most

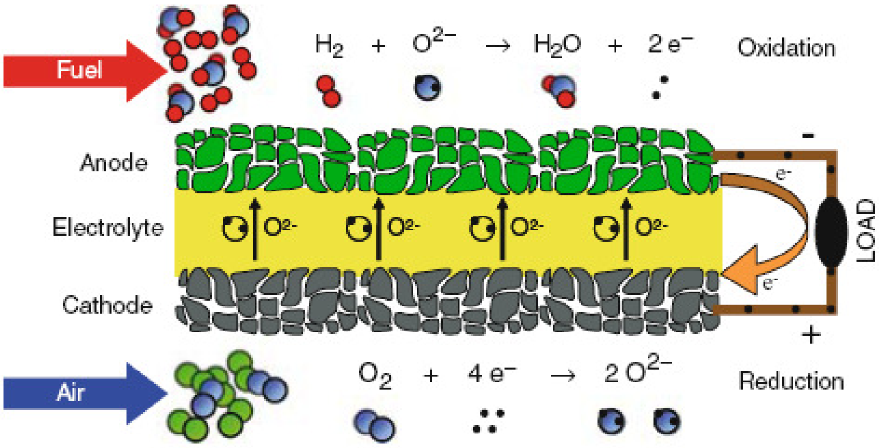

Figure 2-2: Schematic cross section through a SOFC element.[6]

common materials are $La_xSr_{1-x}MnO_3$ (LSM) and $La_xSr_{1-x}Co_yFe_{1-y}O_3$ (LSCF), more cathode materials will be discussed in this chapter. The oxygen ions diffuse through the gas tight electrolyte, which is predominately an ionic conductor. Usually, Yttria doped Zirconium oxide (YSZ) or gadolinium doped cerium oxide (CGO) are used as materials. In the anode compartment, the oxygen ions recombine with the fuel and release the electrons to an external circuit, which conducts the electrons again to the cathode. In the simplest case, the fuel is hydrogen, but hydrocarbons can be used as well. The exhaust products are water and carbon dioxide.

Unlike other types of fuel cells, SOFCs can be operated with a variety of fuels such as methane, carbon monoxide, naphta, gas oil, kerosine, biogas, gases from biomass and landfill wastes due to their high operating temperature. They are partially reformed to CO and H_2, which both maintain a low oxygen partial pressure at the anode due to the low enthalpies of formation of CO_2 and H_2O. For hydrogen, the reaction at the anode is given by:

$$½O^{2-} + H_2 \rightarrow H_2O + 2e^- \qquad 2.5$$

The metal phase, usually Ni, of the porous cermet anode is catalytically active towards fuel oxidation and conducts electrons whereas the ceramic phase is a predominantly ionic conductor and often identical with the electrolyte material. Several of these cells are normally connected by ceramic or metal interconnectors to form a stack of cells with higher voltage and therefore also higher power output. The open circuit voltage (OCV) i.e. when no current is drawn is typically 1V for one cell. Cells are usually operated at the working conditions of maximum power output, e.g. at 0.6 to 0.7 V at temperatures between 900 and 1000°C.

2.2.1.2 Thermodynamics

It was previously stated that fuel cells can be more efficient than heat engines because they directly convert chemical energy to electrical energy. The efficiency of a heat engine is limited by the Carnot cycle: [7]

$$\eta = \frac{T_H - T_L}{T_H} \qquad 2.6$$

where T_H is the maximum temperature of the heat engine and T_L is the minimum temperature of the heat engine. For a typical heat engine that operates at 400±°C (675K) and rejects heat at 50±°C (325K), the maximum theoretical efficiency limit is 52%. In contrast, the ideal efficiency of a fuel cell is given by the ratio of the thermodynamically extractable energy of the reaction (the "free energy", ΔG) to the total heat energy that would have been released by the reaction in a combustion (the "enthalpy", ΔH):

$$\eta = \frac{\Delta G}{\Delta H} \qquad 2.7$$

At standard conditions, ΔH^0 for the hydrogen/ oxygen reaction is -285.83kJ/mole, and the ΔG^0 is -237.14 kJ/mole, giving a theoretical efficiency limit of 83%. Although ΔG^0 represents the energy potential that can be extracted by a fuel cell at standard conditions, this energy is expressed by the fuel cell as an electrical potential, or voltage (E_0):

$$E_0 = \frac{\Delta G^0}{2F} \qquad 2.8$$

where F is the Faraday constant (96485 C/mole).

At standard conditions, this equation yields 1.23 V. This voltage is referred to as the fuel cell open circuit voltage (OCV). ΔG is a function of temperature and pressure, therefore the fuel cell open circuit voltage changes depending on the operating conditions. These dependencies are described by the Nernst equation:[8]

$$E_{Nernst} = E_0 + \frac{RT}{2F} \ln \frac{P_{H_2} P_{O_2}^{\frac{1}{2}}}{P_{H_2O}} \qquad 2.9$$

where,

R= the universal gas constant (8.314 J/mole.K)

T= temperature (K)

P_t= partial pressure of the species i

E_0 is also a function of temperature since $\Delta G\pm$ changes with temperature. As temperature increases, E_0 decreases as shown in Figure 2-3. The Nernst equation is useful in determining the OCV of a fuel cell at arbitrary operating temperatures and gas pressures [9, 10].

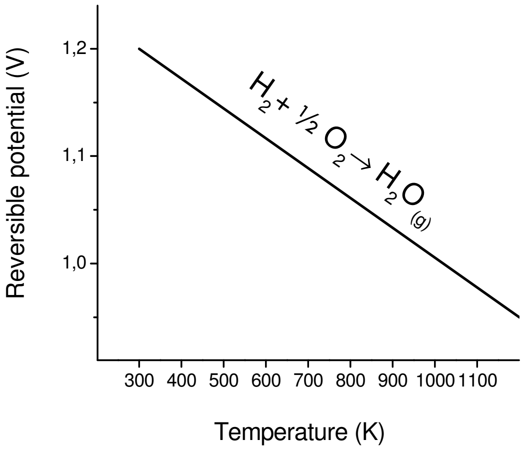

Figure 2-3: The dependence of the ideal fuel cell potential on temperature. The ideal fuel cell voltage decreases with increasing temperature, but usually the opposite is true for the actual fuel cell efficiency due to accelerated electrochemical reaction kinetics at higher temperatures.

2.2.1.3 Kinetics

An ideal fuel cell would supply an infinite current while maintaining the constant voltage determined by the Nernst equation. In practice, however, the actual voltage output of a real fuel cell is less than the ideal thermodynamically predicted voltage. Furthermore, the more current that is drawn from a real fuel cell, the more the voltage output of the cell decreases, limiting the total power that the fuel cell can deliver. The performance of a real fuel cell device can be summarized with a graph of its current vs. voltage characteristics. This graph, called an I-V curve, shows the real voltage output of the fuel cell for a given current output. An example of a typical I-V curve for a fuel cell is shown in Figure 2-4. The current has been normalized by the area of the fuel cell (this gives a current density, A/cm^2). The normalization is done because a larger area fuel cell can produce more electricity than a smaller area fuel cell, IV curves are normalized by fuel cell area to make results comparable. The voltage output of a real fuel cell is less than the thermodynamically predicted voltage output due to irreversible kinetic losses. The more current drawn from the cell, the greater are the losses. There are four major types of fuel cell losses, which give characteristic shape of the I-V:

1. Fuel crossover
2. Activation losses
3. Ohmic losses
4. Concentration losses

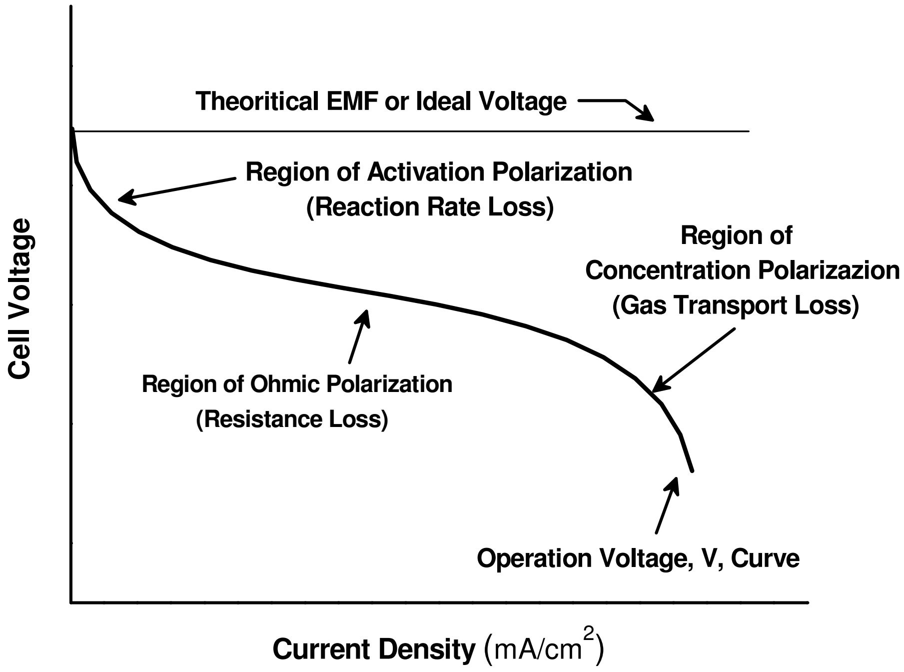

Figure 2-4: Ideal vs. actual fuel cell IV curves. Four major losses accounts for the difference between the two curves [11].

An equation for the true fuel cell IV behavior can thus be written by starting with the thermodynamically predicted voltage output of the fuel cell and then subtracting the various loss terms:

$$E_{real} = E_{Nernst} - jR - \eta_{act} - \eta_{conc} \tag{2.10}$$

where:

E_{real} : real output voltage of the fuel cell
E_{Nernst} : thermodynamically predicted voltage output of the fuel cell from Eq. 1-9
jR : ohmic losses based on total fuel cell current, including fuel crossover loss
η_{act} : activation losses based on total fuel cell current
η_{conc} : concentration losses based on total fuel cell current

The kinetic origins from each of these loss terms will briefly be discussed below. Fuel crossover take place even when no current is being drawn from a fuel cell, the voltage output of the cell is less than the thermodynamically predicted voltage. This initial decrease is due to fuel and electron leaking across the electrolyte membrane. Even though the electrolyte is only supposed to permit oxygen ions to pass, a certain amount of gas leakage and electron flow is always possible. These small leaks act as a "partial internal shortage" for the fuel cell and thus reduce the voltage.

Activation losses: At low current densities, the voltage of a fuel cell drops rapidly. This rapid decline in voltage is due to the cathode and the anode. The oxygen reduction reaction at the cathode is especially sluggish and can account for most of the activation losses. Although the final state of the product water is lower in energy than the initial reactants, an energy barrier impedes the conversion of reactants into products. A portion of the fuel cell voltage is sacrificed to lower this barrier and thus increase the rate at which reactants are converted into product, allowing the fuel cell to output more current. The relationship between the applied activation overvoltage and the current density output is exponential in nature, and can be described by the Butler-Volmer equation [17]:

$$j = j_0\left(\frac{C_O}{C_O^*} e^{-\frac{\alpha F \eta_{act}}{RT}} - \frac{C_R}{C_R^*} e^{-\frac{(1-\alpha) F \eta_{act}}{RT}}\right) \qquad 2.11$$

where,

j : current density (A/cm^2)

j_0 : exchange current density (A/cm^2)

C_O : oxidant concentration at reaction surface (mole/m^2)

C_O^* : oxidant concentration in the bulk (mole/m^2)

C_R : redox concentration at the reaction surface (mole/m^2)

C_R^* : redox concentration in bulk (mole/m^2)

α : transfer coefficient

η_{act} : activation overvoltage = voltage loss due to activation (V)

When the overvoltage is greater than 50 mV, the Butler-Volmer equation can be approximated by a much simpler form called the Tafel equation [17]:

$$\eta_{act} = \frac{RT}{\alpha F} \ln \frac{j}{j_0} \qquad 2.12$$

Activation losses are minimized by maximizing the exchange current density. The exchange current density is a function of the catalyst material and the total reaction surface area. As mentioned earlier, the electrodes are highly porous to maximize the total reaction surface area. This maximizes the amount of triple phase boundary (i.e., the zones where the reaction can occur), thus maximizing the exchange current density.

Ohmic losses: Ohmic losses arise due to the internal resistance of the materials in the fuel cell to the flow of electrons and oxygen ions. These losses are called "Ohmic losses" because they generally follow Ohms law, V=I.R. Both the electrochemically conductive electrodes and the ion conductive electrolyte contribute to the resistance losses. Usually, ionic resistance is dominant in a well-designed fuel cell. The linear drop in the middle of the IV curve in Figure 2-4 distinctly manifests the Ohmic loss effects. In fuel cell systems, most of the Ohmic loss arises from the electrolyte.

Concentration losses: At high current densities, the voltage output of the fuel cell once again drops rapidly, declining quickly to zero. The current density output at zero voltage is known as the short-circuit current, and represents the maximum current that can be produced by the fuel cell. However, at this current level, the voltage output of the fuel cell is zero, so the total power delivered by the fuel cell is also zero. Power (given by the product of the fuel cell voltage and the fuel cell current) peaks somewhere in the middle of the IV curve. The reason for the final steep decline in fuel cell voltage at high current density is due to mass-transport limitations. At high current densities, the fuel or the oxidant gases are consumed on the reaction surfaces faster than they can be replenished. At a certain limiting current density, the partial pressures of the reactant gasses at the reaction surfaces fall towards zero. From the Nernst equation, it is clear that this rapid decline in the partial pressures of reactants causes a dramatic decline in output voltage. The voltage drop from this mass transportation limit is approximated by [16]:

$$\eta_{conc} = A \ln(1 - \frac{j}{j_l}) \qquad 2.13$$

where, A is a fitting parameter (V) and j_l is the limiting current density (A/m^2). Obviously, the concentration loss is dominant at high current density. Well-designed flow structures and thin, highly porous electrodes may reduce the concentration overvoltage.

SOFC components and materials

A SOFC cell consists of a three- or multi-layer ceramic composite structure (Figure 2-5). The gas tight solid electrolyte separates the two porous electrodes and conducts only oxygen ions from cathode to anode. At the cathode side oxygen ions are created after oxygen molecules receive electrons and migrate through the electrolyte. At the anode side oxygen ions give off the electrons and react with fuel. The material requirements at working temperatures between 700 up to 1000°C are extremely demanding. The materials should fulfill various properties such as electric and electrocatalytic properties as well as chemical and thermomechanical properties.

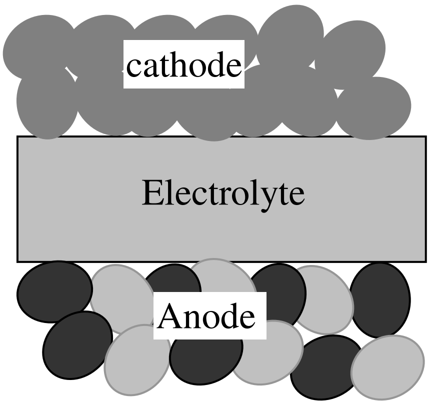

Functional properties	Thermomechanical properties
Mixed conductivity $(\delta_{el} + \delta_{ion})$ Catalytic activity	Stable porosity Expansion coefficient Adhesion to electrolyte
Ionic conductivity $(\delta_{ion} \gg \delta_{el})$	Gas tightness strength
Mixed conductivity $(\delta_{el} + \delta_{ion})$ Catalytic activity	Adhesion to electrolyte Expansion coefficient Stable porosity

Figure 2-5: SOFC components and materials

Electrolyte

In case of SOFC the electrolyte consists of an oxygen-ion conductive material. The most relevant property of the electrolyte is the high oxygen-ion conductivity and low electron conductivity at the same time. A significant electronic conductivity in the electrolyte would lead to internal electric short circuit. The oxygen ion will be still transferred from oxidizing side to reducing side, however a part of created electron flows internally against the oxygen ions. The ratio of electronic to ionic conductivity is called transfer number t:

$$t = \sigma_i / (\sigma_i + \sigma_e) \tag{2.14}$$

For an electrolyte, t should be 1, showing no electronic conductivity. The standard electrolyte material for SOFC is yttrium stabilized zirconium oxide. The compound is predominately ionic and possesses excellent chemical stability and high melting point of 2000 °C. YSZ is created by doping ZrO_2 with a certain percentage (typically around 8 mol%) Y_2O_3. The fluorite crystal structure of the zirconia host is retained. In the YSZ structure, with the replacement of two Zr^{4+} by two Y^{3+}, one oxygen site (O^{2-}) will be left vacant to maintain charge balance. Increasing the yttria content increases the number of these vacant oxygen sites and thereby leads to significant increase of O^{2-} conductivity. If more vacancies are available, more oxygen ions can be transported per time unit, and hence the conductivity will increase. However, there is an upper limit to the amount of doping, beyond which conductivity begins to decrease rather than continue to increase. With increasing defect concentration the electrostatic interaction between dopants and vacancies increases, ultimately impeding oxygen ion and oxygen ion vacancy mobility. In fact, vacancies and dopants may form low-energy associates. The closer the spacing between vacancies and dopants, the more associates will be formed. Closer vacancy-dopant distances are linked to higher barriers for oxygen ion mobility, or stronger associates between vacancies and dopants. The balance between increased vacancy concentration for improved conductivity and simultaneous formation of impeding associates result in a conductivity peak at a concentration of 6% to 8% Y_2O_3, on molar basis.

Doped ceria is another commonly used oxygen-ion-conducting ceramic material with characteristics compatible with SOFC applications. The primary advantage of doped ceria is that it generally shows higher ionic conductivity than YSZ. This relative conductivity advantage is particularly important at lower temperatures. Ionic conductivity is highly dependent on the type and concentration of the dopant and in case of ceria, doping with Samarium and Gadolinium gives the highest values of conductivity. The optimal dopant concentration for SDC and GDC are typically in the range of 10-20%. However, doped ceria has several significant disadvantages. In doped ceria, under reducing atmosphere (i.e. at the anode), Ce^{4+} is partially reduced to Ce^{3+}. This induces n-type electronic conductivity, which can lead to partial internal electronic short circuits, this problem becomes more pronounced at higher temperatures. The second disadvantage is that ceria expands under reducing conditions and the lattice expansion can lead to mechanical failure.

Oxygen-ion-conducting perovskites are the third material class investigated to date as electrolyte. Lanthanum gallate ($LaGaO_3$) has so far emerged as the most promising candidate for SOFC electrolyte applications. High oxygen-ionic conductivity in $LaGaO_3$ is achieved by substituting some of the lanthanum with alkaline earth elements such as strontium, calcium or barium. Minimum lattice distortion yields the highest oxygen-ion mobility. Due to this, strontium is the best choice. The oxygen vacancy concentration can be further increased by substituting some of the gallium with divalent metal cations, such as Mg^{2+}. These dual substitution gives rise to complex oxide stoichiometries like $La_{1-x}Sr_xGa_{1-y}Mg_yO_{3-\delta}$, which is known as the LSGM series. It has been shown that the conductivity of LSGM can be further enhanced by introducing small amounts (below 3-7%) of an additional transition-metal cation that has variable valence, such as cobalt, onto the gallium sites. This additional doping further increases the ionic conductivity in LSGM while generating almost no electronic conductivity. The conductivity of LSGM is entirely ionic and higher than of YSZ over a wide temperature range up to 1000°C. However, at temperatures below 700°C, LSGM's ionic conductivity is less than GDC. Disadvantages of $LaGaO_3$-based materials include possible volatization of gallium oxide, formation of undesired secondary phases during processing and the reactivity with many most common cathode materials under oxidizing conditions. This problem can be potentially addressed by incorporating ceria buffer layers between electrolyte and cathode.

Anode materials

Ni-YSZ cermet is the most commonly used anode material employed in SOFCs as it meets most of the requirements. Ni-YSZ cermet anodes are normally prepared by sintering NiO and YSZ powders together. During the initial exposure to the fuel gases the oxide composite is partially reduced resulting in a porous Ni-YSZ cermet structure.

In the anode structure, Nickel particles provide electronic conductivity and catalytic activity and YSZ particles provide ionic conductivity within the bulk of the electrode, thus effectively expanding the three phase boundaries. YSZ particles act also as an inhibitor for grain growth of Ni phase and improve thermal expansion matching with the electrolyte.

The ionic and electronic conductivity of Ni-YSZ cermet depends strongly on the Nickel content. The electronic conductivity of the anode layer as a function of nickel content follows a sigmoidal-shaped curve, as predicted also by percolation theory. The percolation threshold for the electronic conductivity is approx. at 30 vol% nickel. Below this threshold, the cermet possesses predominately ionic conduction behavior and above this threshold, the conductivity increases and is dominated by electronic conduction through the metallic phase. The ability to match the thermal expansion coefficient by tuning the Ni:YSZ ratio, Ni:YSZ particle size ratio and the porosity is the major advantage of Ni-YSZ cermet. However, several disadvantages of Ni-YSZ cermets are also well documented. They show performance degradation during extended operation. The degradation is caused by grain growth of the Nickel particles, agglomeration and/or oxidation. A low tolerance to sulfur impurities in the fuel stream and a propensity to form carbon deposits (in case of hydrocarbon fuels) are the other most important disadvantages of Ni-YSZ cermets.

In recent years, ceria based materials as SOFC anodes has been investigated as an alternative to Ni-YSZ cermets. The main advantage of ceria based anodes versus Ni-YSZ anodes is their ability to suppress carbon deposition, which facilitates the use of hydrocarbon fuels in SOFC. Since doped ceria shows oxygen-ion conductivity as well as electronic conductivity in reducing environments, the electrochemical reaction (oxidation of fuel) can proceed directly on the surface of doped ceria. However, pure ceria has a substantial mechanical problem in reducing environments, due to the partial reduction of Ce^{4+} to Ce^{3+}. The valence transition results in a lattice expansion, which can cause subsequently mechanical failure due to cracking at the electrode-electrolyte interface. In order to increase the dimensional stability of the anode, ceria can be doped with lower valent cations such as Gd^{3+}, Sm^{3+} and Y^{3+}.

Cathode materials

A cathode material in a SOFC has to exhibit several general properties: (1) high electronic conductivity (>100 $S.cm^{-1}$), (2) non-negligible anionic (oxygen) conductivity (~10^{-1} S cm^{-1}) and chemical stability under fuel cell operating conditions, in particular in contact with the electrolyte. The compatibility with respect to the electrolyte refers not only to chemical inertness both during operation and preparation (usually at considerably higher temperatures), but also to the thermo-mechanical properties of the two materials in contact, i.e. the expansion coefficients have to be similar. The key feature for a cathode material, however, is a high catalytic activity with respect to the dissociation of oxygen molecules and the oxygen reduction, i.e. a low electrochemical polarization resistance.

Perovskite Structure

Traditionally, the perovskite structure has exhibited the most desirable properties as a cathode material. For SOFC the most ceramic materials with mixed conductivity crystallize in the perovskite structure. This structure is named after the mineral perovskite, which has a chemical formula of $CaTiO_3$ and is a naturally occurring mineral that is abundant in chlorite, talc, and serpentine rocks. However, in this case, the term perovskite refers to the ABO_3 structure that is used for a wide variety of mixed conductor systems. The ABO_3 perovskite structure has technological applications that make use of this structure's ability to form oxygen vacancies with proper amounts of doping ions with different oxidation states. This relates to the fact that the perovskites have a good tolerances to deviations from the ideal stoichiometry [12]. The principal perovskite structure is cubic containing three distinct sites for ions: A, B, and O, shown in Figure 2-6. In general terms, the ABO_3 structure can be described as face-centered cubic with A ions at the corners, O^{2-} ions on the faces, and a B ions occupying the octahedral site in the center. The cation with the larger ionic radius occupies the A site

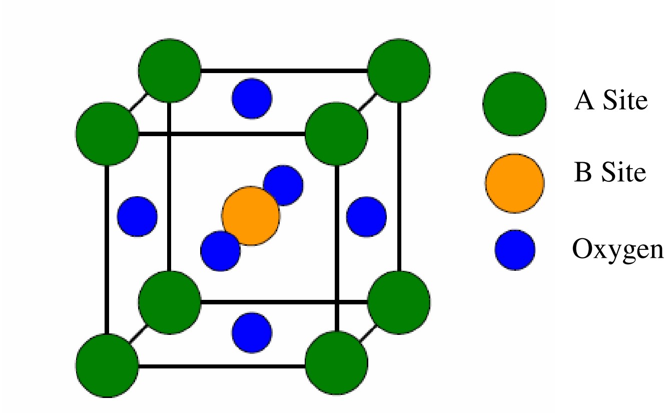

Figure 2-6 Typical Perovskite structure

Whether a composition crystallizes in the perovskite structure depends not only on the stoichiometry but also on the ratio of the ionic radius of the cations. Goldschmidt [13] suggested a formula to determine whether perovskite composition crystallizes in cubic anisotype or in a distorted variant with lower symmetry. For the cubic perovskite phase the tolerance factor t should be between $0.89 \leq t \leq 1.0$, while t for distorted perovskites is smaller than 0.89. For $t< 0.8$ the ilmenit structure forms.

$$t = \frac{r_A + r_B}{\sqrt{2}(r_B + r_X)} \qquad 2.15$$

where,

r_A: Radius of larger A-cation

r_B: Radius of smaller A-cation

r_X: Radius of X-anion

“A” Site Deficiency

In Figure 2-6 a typical perovskite structure is shown. Using Lanthanum and Strontium as A site ions and Manganese as the B site ions, the A site ions, especially La ions, are larger than the Mn ions in the B site. This means that the A site ions dominate the overall crystalline structure. Considering perovskite structure consisting of more A site ions than B site, the larger A site ions will expand the crystalline structure in the direction of the La ions, which will deform and constrian the structure creating a non-cubic or nonideal structure. In order to eliminate this phenomenon, a B site rich or A site deficient structure is created.

Influence of Doping

The ability of the perovskite structure to tolerate changes in its stoichiometry means that the material can be altered by the substitution of different cations in the A and B sites. Several functional properties of a perovskite can be modified by the total or partial replacement of the A and B site cations. The main reason for doping a material with ions with different oxidation states is to increase the ionic conductivity. One of the most common methods of doing this is an A-site substitution to facilitate the formation of oxygen vacancies [14]. Transition metals are normally used for the B site ions as they can assume a mixed-valence state. The partial substitution of the A site cations by other metal cations with lower valence states can cause the formation of oxygen vacancies. This is accompanied by a decrease of the B site cation valence states. This allows the material to maintain charge neutrality [15]:

$$[A'_A] = [B^{\bullet}_B] + [V^{\bullet\bullet}_O] \qquad 2.16$$

Where, $[A'_A]$ refers to doping the A site with a cation with one less positive valence state, $[B^{\bullet}_B]$ refers to the B site cation increasing one valence charge and $[V^{\bullet\bullet}_O]$ refers to the formation of an oxygen vacancy. The Kröger-Vink notation, where the brackets indicate concentrations of the species, is utilized in this equation. The equation means that for every substitution made on the A site, where the new cation has a valence one less than the original cation, there must be a compensation for the charge difference created by this substitution. The compensation can either come from an increase in the valence of the B site cations (electronic compensation) or the formation of oxygen vacancies (ionic compensation). The increase in oxygen vacancy comcentration leads to an increase in ionic conductivity. to the adjacent components a number of the above requirements are more or less fulfilled by the ABO_3 oxide systems of perovskite structure, where A is a rare earth element and B a transition metal (Fe, Ni, Co, Mn). $LaMnO_3$-based systems are considered to be the most promising cathode materials and so were extensively studied. In most cases, alkaline earth (Sr^{2+}, Ca^{2+}) cations are partially substituted for the rare earth element. The charge compensation operates by a valence change of the transition metal cations and, under certain operating conditions, by the formation of oxygen vacancies. Thus, the cathode material behaves as a mixed (ionic + electronic) conductor. The transition metal Mn may also be substituted by other transition metals, mainly Co. Substitution operations are intended to “tailor” the most appropriate cathode with regard to the above mentioned requirements. The $La_{1-x}Sr_xMnO_3$

is the most widely studied system. Introduction of Sr-dopant significantly modifies several properties: The electrical conductivity increases with increasing x. A conductivity maximum is observed for x $\approx$0.5 [16]. A semiconducting type of behavior is observed for low Sr contents (x < 0.4) and a metallic behavior for the most conductive compositions. Furthermore, substituting cobalt for manganese significantly improves conductivity [17].

Cathode material systems

(La,Sr)$MnO_{3\pm\delta}$

$LaMnO_3$ doped with about 10-25% Sr (LSM) is the traditional SOFC cathode material, and the most studied and technologically developed one at the moment. La and Sr ions occupy the A-sites, Mn the B-sites in the perovskite lattice. Replacing La^{3+} by Sr^{2+} ions introduces a charge imbalance, which is compensated either by a valence change from Mn^{3+} to Mn^{4+} or by the formation of oxygen vacancies, depending on oxygen partial pressure and temperature [18-20]. Under SOFC operating conditions, the electronic defects are predominant; a considerable concentration of oxygen vacancies is only formed below ~10^{-12} bar oxygen pressure [18, 20]. A special feature of the $La_{1-x}Sr_x$ $MnO_{3\pm\delta}$ system with $x \leq 0.2$ is the existence of an oxygen excess region for high P_{O_2} [21]. The defects introduced by the doping lead to a high electronic conductivity (σ_{el} > 100 S/cm at 800°C in air [20, 22]) but only to a moderate oxygen ion conductivity (σ_{ion}~10^{-7} S/cm at 800°C in air [21, 23, 24]).

The performance of LSM is acceptable at high temperatures, but insufficient below 800°C. Nevertheless it was the material of choice for the first generation of SOFCs as it represents a fairly good compromise with respect to the different requirements mentioned above. The thermal expansion coefficient of LSM can be matched to that of the electrolyte material YSZ [2, 25-27], and its chemical stability is relatively high. However, it is known that LSM reacts with YSZ at high temperatures to form secondary phases such as $La_2Zr_2O_7$ and $SrZrO_3$ at the interface [28]. These reaction products are detrimental for the performance of the cathode, probably due to their low electrical conductivities [29, 30]. One strategy to avoid the problems associated with the slow oxygen transport is to add a certain amount of electrolyte material (YSZ) into the LSM to form a composite cathode. In such a heterogeneous system, the number of three-phase contacts is strongly increased, and macroscopically the composite behaves similar to a homogeneous material with an effective ionic conductivity that is considerably higher than that of pure LSM. Today, LSM and LSM/YSZ composite cathodes are technically well developed, but it is generally accepted that the electrochemical performance of these systems will not be sufficient for future SOFCs operating in the intermediate temperature range. Therefore, the research focus has shifted towards other materials that offer a high electrochemical performance already at lower temperatures, and particularly the mixed conducting perovskites of the (La,Sr)(Co,Fe) $O_{3\pm\delta}$ family are considered as promising candidates.

(La,Sr)(Co,Fe)$O_{3\pm\delta}$

The unique material properties of the $La_{1-x}Sr_xCo_{1-y}Fe_yO_{3-\delta}$. perovskites suggest an application as SOFC cathode, especially at lower operating temperatures. Experiments on porous $La_{1-x}Sr_xCo_{1-y}Fe_yO_{3-\delta}$ based electrodes have indeed demonstrated a superior electrochemical performance compared to conventional LSM-based cathodes[31, 32]. However, there are also serious drawbacks associated with the use of these materials as SOFC cathodes, which have prevented a widespread technological application so far. Major problems are the chemical stability and the thermo-mechanical compatibility with the electrolyte material YSZ. $La_{1-x}Sr_xCo_{1-y}Fe_yO_{3-\delta}$. /YSZ interfaces are less stable against the formation of $La_2Zr_2O_7$ and $SrZrO_3$ secondary phases than LSM/YSZ interfaces, and this is in particular the case for compositions with a high Co content [33]. Moreover, the thermal expansion coefficients of $La_{1-x}Sr_xCo_{1-y}Fe_yO_{3-\delta}$ and YSZ are substantially different. In this respect the Co-rich compositions, which are usually assumed to show the best electrochemical performance, are most problematic. The thermal expansion coefficient mismatch can be reduced by using Fe-rich compositions (e.g. $La_{0.6}Sr_{0.4}Fe_{0.8}Co_{0.2}O_{3-\delta}$), but a perfect compatibility with zirconia-based electrolytes can not be achievable. A possible solution for these problems might be the use of ceria-based electrolytes, such as $Ce_{1-x}Gd_xO_{2-\sigma}$ or $Ce_{1-x}Sm_xO_{2-\sigma}$ (with x ~ 0.1), instead of YSZ. The ionic conductivity of doped ceria exceeds that of YSZ by roughly one order of magnitude in the relevant temperature range81, and both chemical stability and thermo-mechanical compatibility with $La_{1-x}Sr_xCo_{1-y}Fe_yO_{3-\delta}$ are much less problematic than for YSZ. On the other hand, the major disadvantage of ceria is that it does not only possess an extraordinarily high ionic but also a significant electronic conductivity under fuel cell operating conditions. YSZ/ceria double layer electrolytes have been suggested as one way to overcome this problem, another one would be a reduction of the operating temperature to 500°C. Around this temperature, the electronic contribution to the total conductivity of doped ceria becomes negligible. However, for such a device, cathodes with an extremely low electrochemical resistance would be required. The present work is a contribution to the ongoing search for such high-performance cathodes.

Electrochemical processes at SOFC cathodes

The overall reaction at the cathode is easily expressed by the following formula:

$$O_2(gas) + 4e^-(electrode) \rightarrow 2O^{2-}(electrolyte) \qquad 2.17$$

On a more detailed level this reaction is quite complex and comprises a number of single steps such as diffusion, adsorption, dissociation, ionization and, finally, incorporation of oxygen ions into the crystal lattice of the electrolyte. In general, one may distinguish two reaction mechanisms: the surface and the bulk path (Figure 2-7).

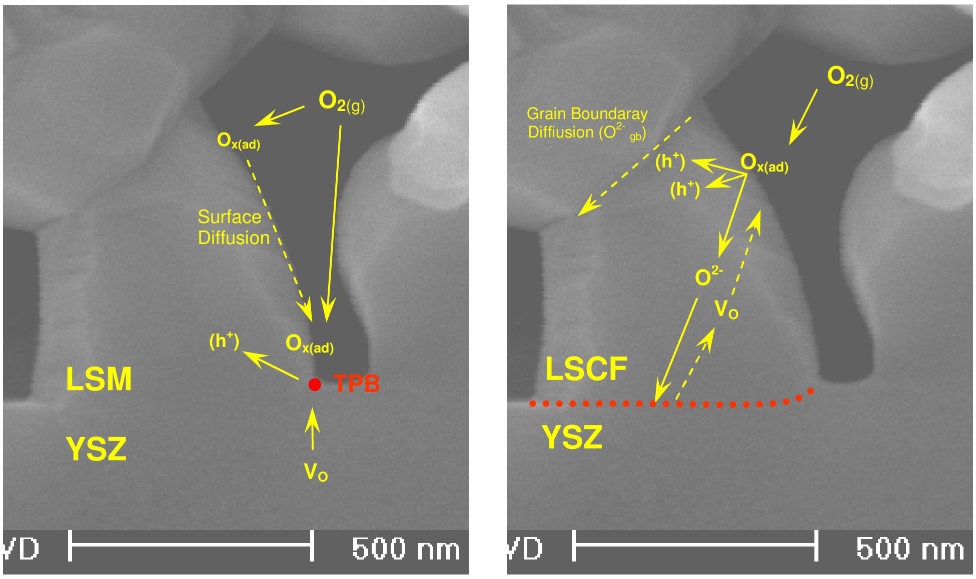

Figure 2-7 Two mechanisms of cathodic oxygen reduction: If the cathode material is a pure electronic conductor (e.g. LSM), the reaction can only proceed via the surface path, where the incorporation of oxygen into the electrolyte occurs at the three phase boundaries. In case of a mixed conducting cathode material (e.g. LSCF), additional to the surface path, the bulk path is also possible.

Following the surface path, O_2 molecules from the gas phase adsorb on the surface and diffuse to a so-called “three phase boundary” (TPB) where electrode, electrolyte and gas phase are in contact. At these electrochemically active regions, oxygen is incorporated as O^{2-} into vacancies of the electrolyte. If the electrode material is a pure electronic conductor (e.g. LSM), the surface path is the only possible mechanism (neglecting adsorption and diffusion on the electrolyte surface, which is unlikely to occur to any significant degree). If the electrode material itself is an oxygen ion conductor, an alternative reaction pathway becomes possible. In this case, oxygen incorporation is not restricted to the TPB zone, but can occur on the whole surface of the electrode. The incorporated O^{2-} ions then diffuse through the bulk of the electrode material towards the electrode/electrolyte boundary, followed by ion transfer across this interface. The surface path is of course not excluded for mixed conducting electrode materials, but may be negligible in special geometries if the electrode material has a high ionic conductivity. In multistep chemical reactions, the exchange rate of one particular step is often much lower than the rates of all other serial processes involved. The kinetics is then rate limited by this “slow” process only, while all others are “fast”, i.e. in equilibrium. The slow process in such a situation is referred to as rate determining step (RDS). Usually, the existence of one single RDS is also assumed for electrochemical electrode reactions.

Table 2-2: Elementary steps in the cathodic oxygen reduction reaction on a mixed conducting electrode material. Each of them could in principle determine the overall reaction kinetics. Parallel TPB processes are neglected.

#	Reaction Step
1	Diffusion of O_2 molecules in the gas phase to the electrode
2	Adsorption of O_2 on the surface of the electrode
3	Dissociation of molecular into atomic oxygen species
4	Charge transfer from the electrode to oxygen species before or after dissociation
5	Incorporation of oxide ions into vacancies of the crystal lattice of the electrode
6	Bulk transport of O^{2-} ions through the electrode to the electrode/electrolyte interface
7	Transfer of O^{2-} ions across the electrode/electrolyte interface

However, the knowledge about the details of these reactions is still limited, despite considerable research efforts. Little is known, for example, about the nature of the oxygen species on the surface of the electrode, and frequently not even the RDS in the total reaction kinetics can be identified for a particular system. Each one of the single steps could in principle be rate limiting, and the kinetic situation may change completely with material, geometry and experimental conditions. Table 2-2 lists reaction steps to be considered as potentially rate limiting for the case of a mixed conducting electrode material.

Thin films for SOFC

Typical operating temperatures for current thick-film SOFCs are 800–1000 °C which places heavy demands on the materials and complicating the sealing mechanism. Therefore, research trends towards lowering the operating temperature down to 500–600 °C. To compensate for the performance losses associated with a lower operating temperature, thin film components with lower ohmic resistance have been developed. Thin film components facilitate the fabrication of SOFCs, leading to new applications for SOFCs, namely portable electronic devices such as laptops, personal digital assistants (PDAs) and scanners [34, 35]. The scope of this part is to summarize the thin film deposition techniques which are applied for SOFC components.

Sputtering

All three components of a fuel cell – anode, electrolyte and cathode – have been studied and realized in thin film form. Thin film electrolytes have been prepared, particularly YSZ [36, 37] and CGO [38, 39]. However, porous Ni/YSZ anodes [40] on dense YSZ substrates as well as anodes and electrolytes on porous substrates such as alumina [41] have been successfully grown as thin films. The deposition of the cathode material lanthanum strontium cobaltite (LSC) was also reported [42]. Deposition is usually performed at low temperature (<400 ◦C) in a partial pressure of oxygen in the order of 10mTorr. Post-deposition thermal treatment in air is then necessary for crystallization and densification of the electrolytes. The deposition of an entire SOFC was reported [43] but the electrolyte (YSZ) was rather thick (15–20 μm) and not fully dense.

Pulsed laser deposition (PLD).

The most important challenge for the application of PLD in industrial production is the difficulty in scaling-up the process. However, possible evolutions of PLD that would allow for large-scale deposition have been proposed. Porous and dense perovskite electrodes [44, 45], electrolytes such as CGO [46, 47], lanthanum strontium gallium manganite (LSGM) [48] have all been deposited by PLD. An entire thin-film-based SOFC was produced by PLD [49] comprising a YSZ electrolyte and LSC cathode both on top of a micro-structured Ni grid that served as an anode.

Chemical vapor deposition (CVD)

CVD processes have been mainly used to produce dense, gas-tight, electrolyte films, 1–10 μm thick, on dense and porous substrates [50-52]. Because the pores of the substrate can be easily closed by this process, CVD is particularly convenient when the electrolyte has to be grown on a porous anode substrate. Furthermore, porous cathodes were also realized [53].

Electrostatic spray deposition (ESD)

Wet-chemical processes are used extensively to produce coatings and thin films for fuel cells, protective coatings or microelectronic devices. The different techniques used to apply the solutions to the substrate can be divided into brush painting, the most basic method, spraying, dipping and spinning.

ESD involves applying a high potential to the surface of a conducting liquid or precursor, which, under the forces of the electric field, generates an almost mono-sized spray from the charged repulsion between droplets. orous and regular structures were produced by Schoonman and coworkers [54]. Porous electrode films of LSCF [55, 56], LSM [57], LSM/YSZ [58] and dense electrolyte films of YSZ [59, 60] are also reported in literature.

Flame spray deposition

Flame or combustion spray synthesis is a method for one-step synthesis and deposition of porous or dense ceramic layers onto heat resistant surfaces. The process can be either a mainly physical process when a suspension of fine oxide particles in a flammable liquid carrier is utilized, or physical and chemical when metal salts in a flammable solvent mixture are used as educts for the ceramic coating formation. On burning in the combustion flame, collision and sintering of the particles in the flame occurs and a coating is formed on the substrate placed in or near the tip of the flame. YSZ [61] and LSM [62] have been produced by this technique.

Pressurized gas spray deposition (PSD).

In PSD, atomization of the precursor is achieved by a pressurized carrier gas, e.g. air. Setoguchi et al. [63] were among the first to utilize the PSD technique for thin film production related to SOFCs. They fabricated a calcia-doped zirconia thin film from acetylacetonate in ethanol on a porous LSM substrate. Perednis et al. published the successful deposition of dense YSZ films with thicknesses <500 nm and porous buffer layers of yttria doped ceria (YDC) [64].

Ultrasonic spray pyrolysis (USP)

Randomly and preferentially oriented YSZ films were prepared by Matsuzaki et al. [65] with ultrasonic spray pyrolysis. The liquid precursor was ultrasonically nebulized and a carrier gas stream was used to transport the fine mist towards the substrate. Films based on lanthanum chromite [66] and ceria layers have also been produced with USP [67].

Electrophoretic deposition (EPD)

EPD is a simple and fast deposition technique to produce thin films from colloidal particles. Powder particles are charged and suspended in a colloidal system. Under the forces of an externally applied electric field, the particles move to the substrate surface and coagulate in a dense layer. Peng et al. [68] utilized EPD to deposit dense YSZ layers on porous LSM cathode substrates, others [69, 70] deposited YSZ on NiO-YSZ anode substrates.

Spin- and dip-coating

The spin- and dip-coating processes are widely utilized to produce thin ceramic coatings on a variety of substrate materials. Thin film deposition with spin-coating consists of applying a precursor solution on one side of a rapidly rotating substrate whereas during the dip-coating process the substrate is partly or fully immersed in the precursor solution with both sides and then withdrawn from the liquid. A huge variety of precursors may be used for these techniques.

Metal organic decomposition (MOD).

In this technique, the precursor is a chemical solution containing metal salts and one or more organic species. The organic compounds evaporate partly during or after deposition and the resulting film pyrolysis upon annealing to form a ceramic coating with the desired stoichiometry. Metal carboxylates are often used as metal salts and dissolved in a suitable solvent. Hayashi et al. [71] produced LSM/YSZ composite film electrodes by the MOD technique. The solution used was a mixture of octylates of La, Sr and Mn in a solution of iso-propanol containing triethanolamine and butoxides of Zr and Y in a solution of isopropanol and diethanolamine. LSC and lanthanum manganite films doped with Ca, Sr or Ba [72] were synthesized in much the same way as above with a solution based on neodecanoates in xylene.

2.3 Cathode performance

The performance of cathodes (electrocatalytic activity for oxygen reduction) is evaluated by the area specific resistance (ASR), which is not only influenced by the choice of the material, but also by the microstructure and the processing. To provide an overview of cathode performance Table 2-3 contains the ASRs for many different cathodes. Different performances of the same material are included on purpose, to illustrate the wide range of performance that can be achieved by nominally the same material.

Table 2-3: Area specific resistance (ASR) of different cathode materials at different temperatures, stoichiometry and composition of multiphase cathodes. The given ASR values are the measured values at 600 and 800 °C.

Material	ASR/(Ω·cm²)		Ref.
	650°C	800°C	
$La_{0.72}Sr_{0.18}MnO_3$ + $Ce_{0.9}Gd_{0.1}O_{1.95}$ + $La_{0.6}Sr_{0.4}Co_{0.2}Fe_{0.8}O_3$	0.4	0.08	[73]
$(La_{0.75}Sr_{0.25})_{0.95}MnO_3$ + 50 vol % YSZ	5.6	0.63	[74]
$(La_{0.75}Sr_{0.25})_{0.95}MnO_3$ + 50 vol % YSZ	3.2	0.25	[74]
$La_{0.8}Sr_{0.2}MnO_3$	223	1.4	[75]
$La_{0.8}Sr_{0.2}MnO_3$	1100	60	[76]
$La_{0.8}Sr_{0.2}MnO_3$ + YSZ		7.6	[39]
$(La_{0.8}Sr_{0.2})_{0.98}MnO_3$ + 50 vol % YSZ	0.5		[40]
$La_{0.8}Sr_{0.2}MnO_3 + La_{0.5}Sr_{0.5}CoO_3$		1.3	[77]
$La_{0.8}Sr_{0.2}MnO_3 + LaCoO_3$		0.2	[77]
$La_{0.8}Sr_{0.2}MnO_3 + LaNi_{0.6}Fe_{0.4}O_3$		0.4	[77]
$La_{0.85}Sr_{0.15}MnO_3$ + YSZ		0.08	[76]
$La_{0.85}Sr_{0.15}MnO_3$ + YSZ		0.58	[78]
$La_{0.85}Sr_{0.15}MnO_3$ + YSZ		1.2	[78]
$La_{0.85}Sr_{0.15}MnO_3$ + YSZ		2.4	[78]
$La_{0.85}Sr_{0.15}MnO_3 + Sm_{0.2}Ce_{0.8}O_{1.9}$		0.63	[79]
$La_{0.85}Sr_{0.15}MnO_3$ + YSZ		1.2	[78]
$La_{0.85}Sr_{0.15}MnO_3$ + YSZ		2.4	[78]
$La_{0.85}Sr_{0.15}MnO_3$ + YSZ + $La_{0.8}Sr_{0.2}CoO_3$		1.2	[80]
$La_{0.85}Sr_{0.15}MnO_3$ + YSZ + $La_{0.84}Sr_{0.16}CoO_3$		3.7	[81]
LSM + $Ce_{0.9}Gd_{0.1}O_{1.95}$	0.6	0.04	[82]
$La_{0.7}Sr_{0.25}FeO3$	5.5	0.13	[33]
$La_{0.8}Sr_{0.2}FeO_3$	120	9	[33]
$La_{0.6}Ca_{0.4}MnO_3$	10	0.48	[75]
$Pr_{0.8}Sr_{0.2}FeO_3$	65	3.5	[77]
$La_{0.2}Sr_{0.8}Co_{0.8}Fe_{0.2}O_3$	14	1.6	[83]
$La_{0.6}Sr_{0.4}Co_{0.2}Fe_{0.8}O_3$	1.2		[84]
$La_{0.6}Sr_{0.4}Co_{0.2}Fe_{0.8}O_3$	6.5		[85]

$La_{0.6}Sr_{0.4}Co_{0.2}Fe_{0.8}O_3$	1.9	0.52	[83]
$La_{0.6}Sr_{0.4}Co_{0.2}Fe_{0.8}O_3$	0.65	0.05	[82]
$La_{0.6}Sr_{0.4}Co_{0.2}Fe_{0.8}O_3$	0.8		[33]
$La_{0.6}Sr_{0.4}Co_{0.2}Fe_{0.8}O_3$	2.9		[79]
$La_{0.6}Sr_{0.4}Co_{0.2}Fe_{0.8}O_3$	0.67		[86]
$La_{0.6}Sr_{0.4}Co_{0.2}Fe_{0.8}O_3$+25vol% $Ce_{0.9}Gd_{0.1}O_{1.95}$	0.95		[87]

2.4 Electrochemical Impedance Spectroscopy

The experimental method of electrochemical impedance spectroscopy (EIS) originates from liquid electrochemistry but it is equally used for solid state electrochemistry. The method of EIS is discussed in detail in [88, 89]. This chapter merely focuses on some specific aspects which are of particular importance for the understanding of the EIS analyses in chapter five of this thesis. Electrode measurements can be carried out with respect to a reference electrode. This kind of experimental set-up is referred to as three point mode (Figure 2-8). The three contact points are the working, the reference, and the counter electrode. If one uses two different wires for the current and for the voltage at the working electrode, one refers to a four lead configuration. A schematic diagram of the wire connections for a three point, four lead configurations for impedance measurements of SOFC electrodes is illustrated in Figure 2-8a. In the case of an anode measurement, the terms working and counter electrode refer to the anode and to the cathode, respectively. In this study the reference electrode is always associated with the working electrode: it is composed of the same material and it is situated in the same gas atmosphere as the working electrode.

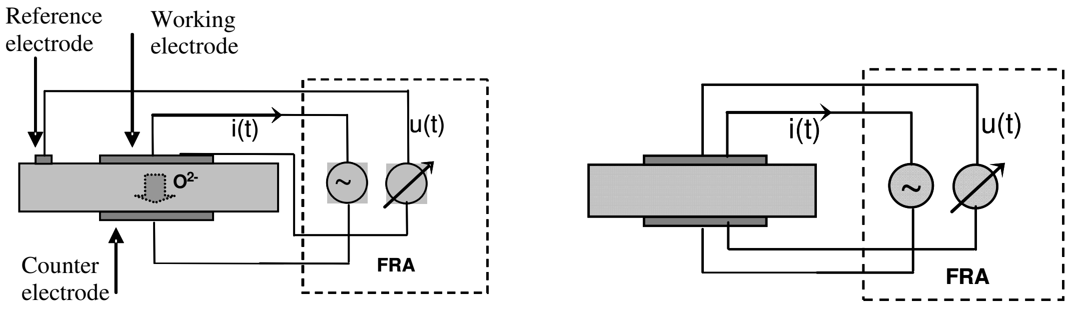

Figure 2-8: Schematic diagram of the wire connections for a three point, four lead and two points four leads configurations for impedance measurements of SOFC electrodes.

In order to study the polarization characteristic of the working electrode, a certain potential, the so-called overpotential, is applied between the working and the reference electrode. A positive potential signifies an anodic overpotential, whereas a negative potential signifies a cathodic overpotential. In case of impedance measurements under equilibrium conditions, the working and the reference electrode are set at the same potential. Figure 2-8b demonstrates the cell configuration for a symmetrical sample by four leads and two points. The symmetrical cell consists of two similar electrodes. This configuration is applied for electrochemical impedance measurements under equilibrium conditions. A small alternating voltage is applied across the sample and the current response is measured simultaneously.

$$\Delta U(\omega,t)=U_m.e^{-i\omega t} \qquad 2.18$$

$$\Delta I(\omega,t)=I_m.e^{-i(\omega t+\varphi)} \qquad 2.19$$

where t is the time, U_m and I_m the amplitudes, ω the angular frequency, φ the phase difference between the voltage and the current. The impedance, Z, is then defined as

$$Z(\omega)=\frac{\Delta U(\omega,t)}{\Delta I(\omega,t)}=\frac{U_m}{I_m}.e^{i\varphi} \qquad 2.20$$

Using the Euler relation

$$e^{i\varphi}=\cos\varphi+i\sin\varphi \qquad 2.21$$

the impedance becomes :

$$Z(\omega)=Z'(\omega)+iZ''(\omega) \qquad 2.22$$

where

$$Z'=real(Z)=|Z|.\cos\varphi \qquad 2.23$$

$$Z''=imag(Z)=|Z|.\sin\varphi \qquad 2.24$$

$$|Z|=\frac{U_m}{I_m}=\sqrt{Z'^2+Z''^2} \qquad 2.25$$

$$\tan\varphi=\frac{Z''(\omega)}{Z'(\omega)} \qquad 2.26$$

Impedance spectra can be plotted in two ways: in the Nyquist representation where the negative imaginary part of the impedance, Z", is plotted vs. the real part of the impedance, Z (Figure 2-9) or in the Bode representation where the absolute impedance, | Z |, as well as the phase shift are plotted vs. the angular frequency. Both representations contain, in principle, the same information and can be transformed into each other. However, depending on the data, one or the other representation is preferred because specific details can be resolved more precisely. Hence, in impedance analyses, both representations should always be considered.

Characteristic Parameters

The following characteristic parameters are obtained from the impedance data:

- The so-called electrolyte resistance, Re, which is caused by the electrolyte and leads. It can be determined from the high frequency part of the Nyquist plot at the intersection of the impedance data with the real axis (Figure 2-9).
- The polarization resistance, R_p , which is originating from electrode/electrolyte interface. It can be determined from both the Nyquist as well as from the Bode plot, as the ohmic difference between high and low frequency intersections (Figure 2-9).
- The relaxation frequency, ω, which is defined as the frequency at the maximum imaginary impedance value. In the case of several relaxation processes, there exist several relaxation frequencies which can be identified as local maxima in the Nyquist plot (Figure 2-9).

Two serial RC elements lead to two well-separated semicircles in the complex impedance plane if their relaxation frequencies are sufficiently different. In a real system, this may for example be realized by a large difference in the magnitude of the capacitances and similar values for the resistances. Hence, if a measurement yields one or several well separated semicircles, the resistances and relaxation frequencies of the underlying processes can immediately be read from the Cole-Cole plot, and thus a capacitance can be calculated for each process. The magnitude of a capacitance is often already a strong indication of its physical origin. Typical orders of magnitude of some capacitances in solid state electrochemistry are given in Table 2-1 [90-92].

The analysis of the measured impedance spectra is performed by describing the electrochemical processes as a combination of electrotechnical impedance elements in series or parallel connection. Table 2.4 presents an overview of the most important impedance elements [88]. The main challenge is the introduction of an electrochemically reasonable equivalent circuit built up of ideal resistors, capacitors, inductances, and possibly distributed elements, which allows the approximation of the experimental impedance data.

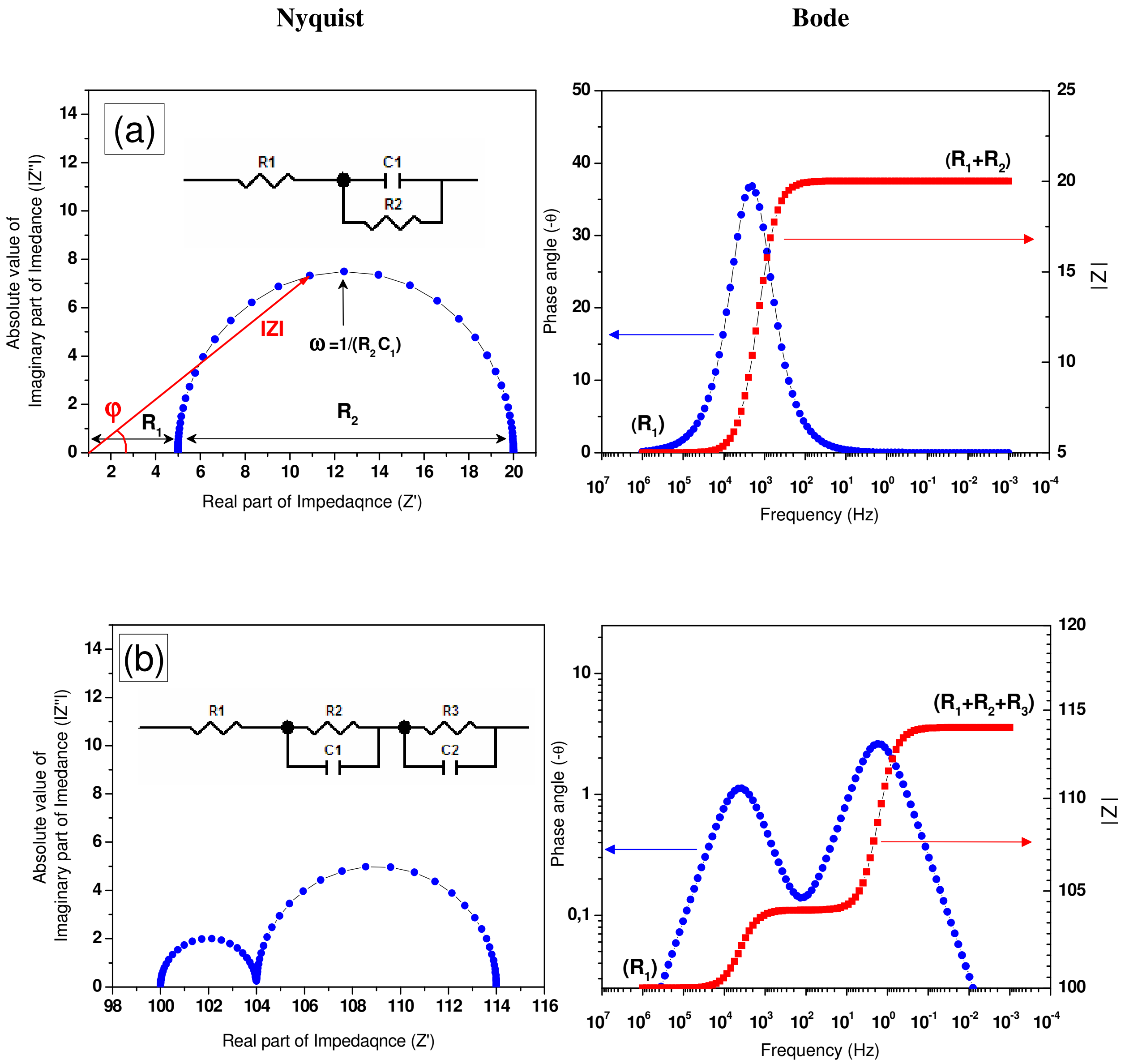

Figure 2-9: Simulated impedance spectra of (a) one RC-element with the parameters: R1 = 5 Ω , C = 10 µF, R2 = 15 Ω, (b) two serial RC elements with substantially different relaxation times with the parameters: R1 = 100 Ω , C1 = 10 µF, R2 = 4 Ω, R3 = 10 Ω, C2 = 0.01 F, C2 = 10 µF; frequency range: 10^{-3} - 10^{6} Hz.

Table 2-4: Description of the most important impedance elements, * describes the capacitance of a not ideally flat electrode surface, ** W: Warburg-Parameter containing reaction parameters and the diffusion coefficient [88].

Impedance Element	**Imedance**	**Phase angle**	**Origin**
Ohmic Resistance	R	0°	Conductivity path(electrolyte resistance, charge transfer resistance)
Capacitance	$\frac{1}{j\omega C}$	-90°	Double layer (adsorption)
Constant Phase Element *	$\frac{1}{\omega_0 v(j\omega/\omega_0)^{\alpha}}$	$\frac{(-\alpha).\pi}{2}$	Modification of capacitance for porous electrodes
Induction	$j\omega L$	90°	Voltage build up due to self-induction in current carrying conductors
Warburg Impedance **	$\frac{W}{\sqrt{j\omega}}$	-45°	Linear diffusion of reactants

Figure 2-9 presents an equivalent circuit of a very simplified electrochemical system. Any electrode material system has a capacitance and a bulk resistance in parallel. In addition, the electrolyte resistance is connected serially. In case of porous electrodes the ideal capacitance sometimes has to be replaced by a constant phase element to consider the deviations from the ideal capacitative behavior [93, 94]. Even though approximation of the measured impedance data by equivalent circuits is widespread, complex electrode processes lead again to complex equivalent circuits. Since different circuits can describe the same set of data one has to keep in mind that with increasing complexity the possibility of interpretational errors increases [95]. In most situations, however, the required equivalent circuit representation and thus the interpretation of impedance spectra is more complicated. Some of the difficulties frequently encountered when interpreting impedance spectra shall be briefly mentioned in the following: Obviously, difficulties emerge if two serial processes have similar relaxation frequencies. In such a case the two semicircles overlap, and the resulting impedance behavior may appear as a single, distorted arc in the complex impedance plane.

Table 2-5: Typical orders of magnitude of some capacitances observed in solid state ionics

Capacitance	**Corresponding physical process**	**Typical value per area (F/cm²)**
C_{Bulk}	Dielectric relaxation in bulk material	~ 10^{-12}
C_{gb}	Grain boundary polarisation in a polycrystalline material	~ 10^{-8}
C_{dl}	Electrical double layer polarization at solid/solid interface	~ 10^{-5}
C_{chem}	Oxygen stoichiometry polarisation in the bulk of a mixed conducting thin film electrode	~ 10^{-2}

The decision on whether or not such a distorted semicircle consists of two components is aggravated by the empirical fact that experimental semicircles are always “non-ideal” to some degree, i.e. more or less depressed, even if they are caused by a “single” electrochemical process. Apparently, an RC element generally oversimplifies the real situation. A path frequently followed in order to deal with depressed semicircles is to replace the capacitor of an RC element by a so-called constant phase element Q, with impedance

$$\bar{Z}_Q = \frac{1}{Q(i\omega)^n} \qquad 2.27$$

A constant phase element may thus be regarded as a generalization of a capacitance, which takes account of the “non-ideality” of experimentally observed semicircles. The parameter n, a constant defined by Eq. 2.27, is essentially a measure of the degree of “depression” of such an arc. For n = 1, the constant phase element is identical to a capacitance, corresponding to a perfect semicircle in the Cole-Cole plot. For n < 1, one obtains more or less depressed arcs. By introducing constant phase elements one can often achieve an accurate fitting also for non-ideal impedance arcs. From the fitting parameters Q and n, a capacitance C can then be calculated according to [21].

$$C = (R^{1-n}Q)^{1/n} \qquad 2.28$$

In this thesis the interpretation of impedance spectra was carried out by the equivalent circuit models for pure electron conductive (LSM), composite cathodes (LSM-YSZ and LSM-GDC) and mixed conductive cathodes as proposed frequently in literature.

3 Experimental procedures

3.1 Synthesis

The spray pyrolysis set up consists of a system for atomization (nebulization) of the precursor, a reactor for the pyrolysis of the nebulized precursor, collection (filtration) of synthesized particles and a system for gas flow and pressure control within the entire setup. [96-101]

Nebulization of precursor: The nebulization is carried out in a glass chamber with several connections for carrier gas inlet and outlet and precursor supply. An ultrasonic generator (Dr. Hielscher UM20-1.6MHz) is flanged connected at the bottom of the glass chamber. A micro dosage pump supplies the precursor dropwise to the ultrasonic active membrane. The generated mist in the glass chamber is transported to the reactor by means of the carrier gas.

Reactor: The reactor consists of a resistively heated furnace (Thermal Technology, Bayreuth) and an Aluminum oxide tube (Friatec Degussit AL23, Mannheim) with an inner diameter of 20 mm.

Deposition (Filtration) of particles: After the reaction zone the carrier gas passes through a paperfilter (Sartorius, Göttingen) and the particles are collected on the filter. The temperature of the collected chamber is held at 110°C in order to avoid condensation of water vapor on the filter. At the end of the synthesis the particles are collected as a filter cake.

Gas flow and pressure control system: A gas flow controller (MKS Instruments 1179A, Wilmington, Massachuset, USA) supplies a constant gas flow of 5 sLm O_2. A rotary vane pump

(Leybold Sogevac SV 65, Bourg-les-Valence, France) is connected to the end of the system after the filtration chamber and pumps the carrier gas through the paper filter. The pumping speed of the pump is controlled by an automatic valve (MKS Instrument 248A) in combination with a pressure sensor (MKS Instrument 722A) which are located between the filter and vacuum pump. A central controller (MKS Instrument 647B) conducts all controlling tasks.

Preparation of precursors: The water based precursors are prepared by the citrate method, as described in different variations in the literature [102]. The aim of the method is to stabilize a homogeneous distribution of different metal salts in the water based solution. Citric acid serves as a complexing agent and forms a carboxilate-network. Three different precursors are prepared for the following target material systems; $La_{0.75}$ $Sr_{0.2}$ Mn $O_{3-\delta}$, $La_{0.6}Sr_{0.4}Co_{0.2}Fe_{0.8}O_{3-\delta}$ and $La_{0.25}Ba_{0.25}Sr_{0.5}Co_{0.2}Fe_{0.8}O_{3-\delta}$. The starting chemicals are lanthanum nitrate hexahydrate (99.99%, Alfa Aesar, Karlsruhe, Germany), strontium nitrate (99.996%, Alfa Aesar), barium nitrate (99%, Sigma-Aldrich Chemie GmbH, Munich, Germany), cobalt(II) nitrate hexahydrate (99%, Sigma-Aldrich Chemie GmbH, Munich, Germany) and iron(III) nitrate nonahydrate (99%, Merck KGaA, Darmstadt, Germany) and manganese nitrate tetrahydrate (99.5%, Merck KGaA, Darmstadt, Germany). The equivalent amounts of nitrates in the desired ratio are dissolved in deionized water at 80 °C. Afterwards, citric acid is added to the solution at 90 °C. The molar ratio of citric acid to metal ions is adjusted to 1.5. After addition of citric acid the solution is stirred for 30 min. By adding ammonium hydroxide the pH-value is adjusted to 9.

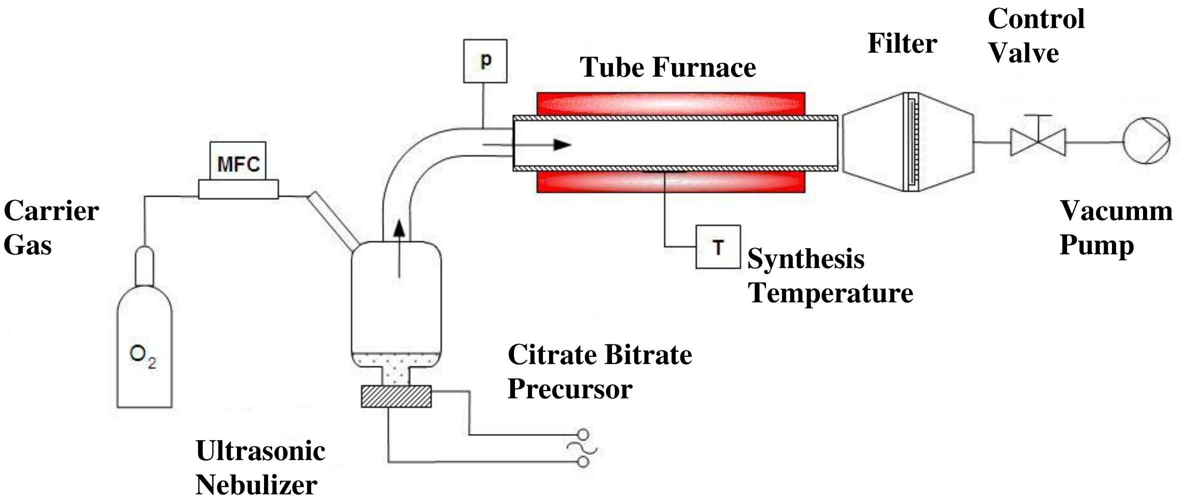

Figure 3-1: Synthesis setup for Nebulized Spray Pyrolysis

3.2 Characterization methods

Inductively Coupled Plasma Optical Emission Spectrometry

In order to verify the ratio between cations Inductively Coupled Plasma Optical Emission Spectrometry (ICP-OES) is used. The measurements are carried out with a Perkin Elmer Optima 3000 device (Perkin Elmer, Waltham, USA). The powders are dissolved in nitric acid and diluted to 1:100 ratio with water for sample preparation.

Thermoanalysis

Thermal analysis is performed with a Netzsch STA 429 (Netzsch, Selb) in the thermogravimetery (TG) and differential thermoanalysis (DTA) modes. Platin crucibles are used for the measurements.

Scanning electron microscopy

Scanning Electron Microscopy is performed using either LEO GEMINI 1530 (Carl Zeiss, Oberkochen) or a Philips XL30 FEG. The micrographs are taken using secondary electron detector. Carbon pads are adhered on the aluminum sample holder and coated slightly with the loose powder. The samples are finally sputtered with Gold-Paladium in order to avoid electrical charging caused by the electron beam.

Nitrogen Adsorption

The adsorption of nitrogen for the determination of the specific surface area is carried out with a Quantachrome Autosorb-3b (Quantachrome, Boynton Beach, Florida, USA). Prior to the measurement of adsorption and the desorption isotherms all samples are heated up at 200 °C under vacuum for at least 12 hours. The analysis of the results are made according to the Brunauer, Emmett and Teller method (BET method) [103].

X-ray diffraction

The X-ray diffraction (XRD) is measured with a diffactometer type of Bruker AXS D8 Advance (Bruker AXS, Karlsruhe) in the classical Bragg-Brentano-Geometry. The diffractometer is equipped with a high temperature chamber and a position sensitive detector (PSD). Copper radiation is used in conjunction with a variable slit assembly to illuminate a constant sample length of 12 mm. The axial divergence is reduced by primary and secondary Soller slits with 2.5° angle of acceptance. Each diffraction pattern was recorded with an energy dispersive detector (Bruker AXS Sol-X) with a 0.2 mm detector slit mounted using a step size of 0.021. From the emission spectrum of the X-ray tube Cu-Kα radiation with a wavelength of 0,154 nm is selected. In the high temperature chamber (Anton Paar HTK 1200N, Graz, Austria) the sample is positioned on an aluminum oxide rotating sample holder. A position sensitive detector (Bruker AXS VANTEC,

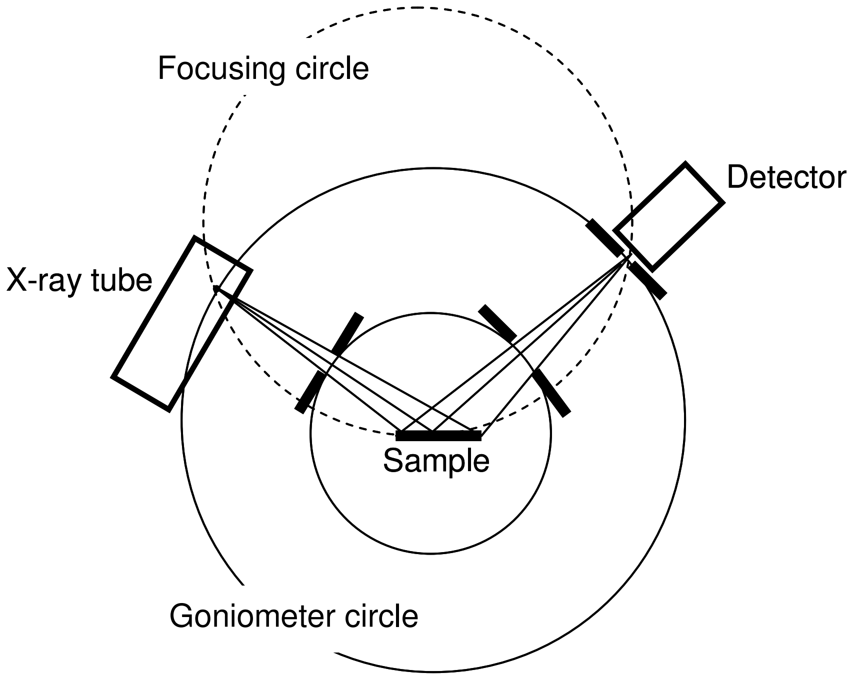

Figure 3-2: X-ray diffraction setup for room temperature and in-situ high temperature measurements

Karlsruhe) is used for the high temperature measurements. In front of the detector a Ni-foil for filtering the Cu-Kα beam and a soller slit with 2.5° opening angle are used. The PSD is adjusted in order to be able to measure simultaneously a 2θ angle range of 10°.

Characterization of dispersions

3.2.1.1 Zeta potential

Zeta potential is the electrical potential that exists at the shear plane of a particle, which is some small distance from the surface. Colloidal particles dispersed in a solution are electrically charged due to their ionic characteristics and dipolar attributes. The development of a net charge at the particle surface affects the distribution of ions in the neighboring interfacial region, resulting in an increased concentration of counter ions (ions of charge opposite to that of the particles) close to the surface. Each particle dispersed in a solution is surrounded by oppositely charged ions called fixed layer. At larger distances beyond the fixed layer, there are varying compositions of ions of opposite polarities, forming a cloud-like area. Thus an electrical double layer is formed in the region of the particle-liquid interface. The double layer may be considered to consist of two parts: an inner region which includes ions bound relatively strongly to the surface and an outer or diffuse region in which the ion distribution is determined by the balance of electrostatic forces and random thermal motion.

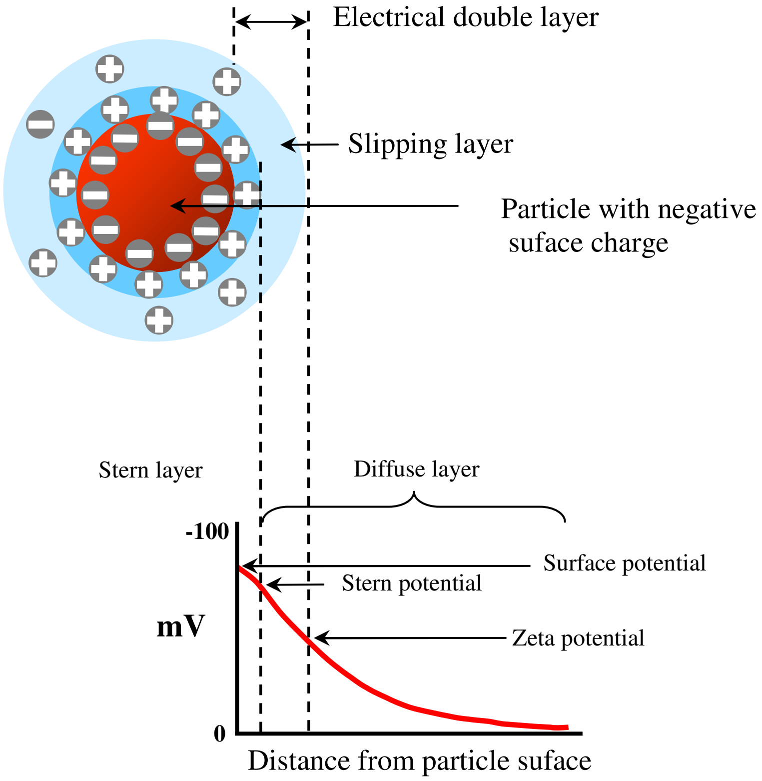

Figure 3-3: Schematic representation of Zeta potential

The potential in this region, therefore, decays with the distance from the surface, until at a certain distance it becomes zero [104]. When a voltage is applied to the solution in which particles are dispersed, particles are attracted to the electrode of the opposite polarity, accompanied by the fixed layer and part of the diffuse double layer. The potential at the boundary between this unit, that is to say at the above-mentioned shear plane between the particle with its ion atmosphere and the surrounding medium, is known as the Zeta Potential. The Zeta potential can not be measured directly but it can be calculated using theoretical models and an experimentally-determined electrophoretic mobility. In practice, the Zeta potential of dispersions is measured by applying an electric field across the dispersion. Particles within the dispersion with a zeta potential will migrate towards the electrode of opposite charge with a velocity proportional to the magnitude of the zeta potential. This velocity is measured using the technique of the Laser Doppler Anemometer. The frequency shift or phase shift of an incident laser beam caused by the moving particles is measured as the particle mobility, and the mobility is converted to the Zeta potential by considering the dispersant viscosity, as described by the theory of Smoluchowski [105]. This yields the following equations from which the Zeta potential ζ can be calculated.

$$\mu_e = \frac{2\varepsilon.\zeta.f(Ka)}{3\eta} \qquad 3.1$$

$$V_S = \mu_e E \qquad 3.2$$

ζ : Zeta Potential (mV)

η : Viscosity of medium

ε : Dielectric Constant of medium

V_S : Speed of particle (cm/sec)

E : Electric field (V/cm)

μ_e : The electrophoretic mobility

3.2.1.2 Particles size distribution

Dynamic light scattering (DLS), which is also known as "Photon Correlation Spectroscopy" (PCS) or "Quasi-Elastic Light Scattering" (QELS), uses the scattered light to measure the rate of diffusion of the particles from which a size distribution for the sample can be determined. The size is given by the "Stokes radius" or "hydrodynamic radius" of the particle. This hydrodynamic size depends on both mass and shape (conformation) of the particle. In dynamic light scattering one measures the time dependence of the light scattered from a very small region of solution, over a time range from tenths of a microsecond to milliseconds. The fluctuations of intensity of the scattered light are related to the rate of diffusion of particles in and out of the region being studied (Brownian motion), and the data can be analyzed to directly yield the diffusion coefficients of the particles. Rather than presenting the data in terms of diffusion coefficients, the data are processed to give the "size" of the particles (radius or diameter). The relation between diffusion and particle size is based on theoretical relationships for the Brownian motion of spherical particles, originally derived by Einstein. The "hydrodynamic diameter" or "Stokes radius", R_h, derived from this method is the size of a spherical particle that would have a diffusion coefficient equal to that of the particle. Set-up which is schematically represented in Figure 3-4 consists of a monochromatic laser focused at the center of the goniometer of the light scattering photometer, where the sample is located [106, 107]. The sample cell (a cylindrical quartz cuvette) is mounted in the middle of the goniometer, surrounded by an index matching bath that reduces the scattering of the cuvette edges and serves to thermostatically couple the cuvette to the rest of the measurement block, which is temperature stabilized.

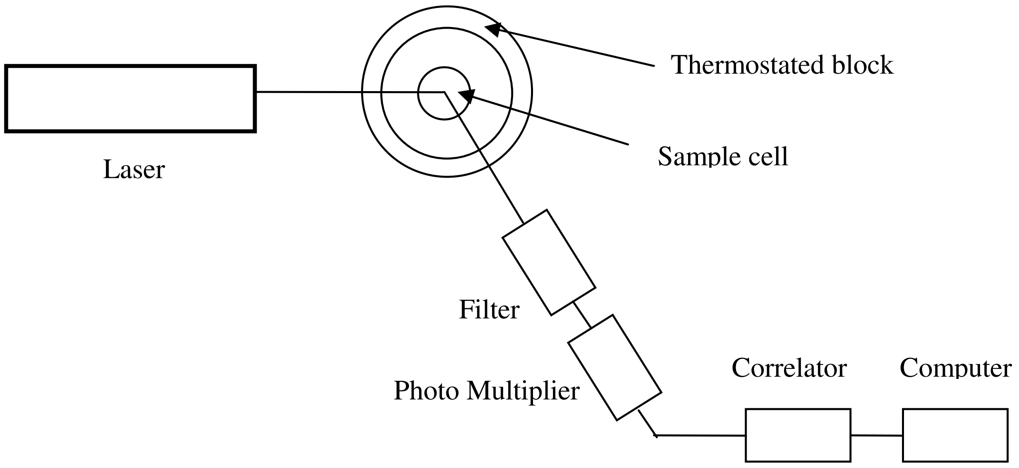

Figure 3-4 Schematic of the dynamic laser scattering setup

The scattered light is collected by a photomultiplier (PM) or a photodiode, mounted on the goniometer arm, in such a way that it can be moved at different angles, generally from 15° to 175°. Shining a monochromatic light beam, such as a laser, onto a solution with spherical particles in Brownian motion causes a Doppler Shift when the light hits the moving particle, changing the wavelength of the incoming light. This change is related to the size of the particle. It is possible to compute the sphere size distribution and give a description of the particle's motion in the medium, measuring the diffusion coefficient of the particle and using the autocorrelation function.

$$I_S \propto I_0 \frac{n_0^2}{\lambda^4}\left(\frac{dn}{dC}\right)^2 N(R).\,R^6.\,P(R,\theta).\,S(R,\theta,Conc.) \qquad 3.3$$

where

I_0 : Intensity of incident light

n_0 : Refractive index of the solvent

λ : Light wavelength (in vacuum)

dn/dC: Refractive index increment (n is referred to the solution)

N(R) : Number of particles with radius R

R : Radius of a particle

P(R, θ) : Particle form factor which describes the influence of intraparticle interface effects on the angular dependence of the scattered intensity and thus provides information on the shape and structure.

S(R, θ, Conc.) : Time-averaged structure factor which describes interparticle interface effects. It depends on the concentration and for dilute solutions S→1.

There are three major factors to be identified in the scattered light intensity of a dilute sample containing some scattering particles. The number, the size, and the shape of the particles are responsible for the scattered light intensity, which is also dependent on the angle of observation. Since the scattered light depends on the sixth-power of the radius of the scattering particles, it is clear that big particles contribute greatly to the scattered light intensity. On the other hand, the form factor P, a complex function of shape and scattering vector, is involved in the angular variation of the scattered light. Finally, in the case of a concentrated solution, the structure factor S becomes important, and provides some information, beyond a certain limit, on multiple scattering phenomena that make the theoretical aspects more complex. In the dynamic light scattering the temporal fluctuations of the scattered light around its average value are recorded and analyzed in order to estimate the size of the scatterers and their size distribution. These fluctuations originate from the Brownian motion of the scatterers, which move continuously and randomly in solution, in a way that is size-dependent.

3.3 Preparation of symmetrical samples

Spin coating

Functional thin cathodes were prepared by spin coating of stabilized dispersions of LSM, LSCF, LBSCF and their composites with GDC (10-30%wt) as an ionic conductive component. Both sides of the polycrystalline YSZ substrates (200 µm thickness, 8% yttria, Itochu, Japan) were spin coated with the dispersions at 1700 rpm. In order to avoid the chemical reaction between LSCF and LBSCF with the YSZ substrate in case of mixed-conductive cathode material systems, a thin buffer layer of GDC nanoparticles was deposited on both sides of the YSZ substrates by spin coating (rpm: 2500) a stabilized GDC dispersion. The GDC buffer layer was sintered at 950 °C for 2 h. After the deposition of the nanocomposite functional layers (10–30 wt% GDC) the samples were sintered at various temperatures in order to investigate the effect of the sintering temperature on the electrochemical performance. In case of LSM cathodes a preheating treatment at 800, 850 and 900°C and in case of LSCF and LBSCF 650, 700 and 750 °C for 10 hours was carried out.

Screen printing

In order to facilitate a proper distribution of the potential during the electrochemical impedance measurements a commercial $(La_{0.8}Sr_{0.2})_{0.95}MnO_3$ paste (d50=0.39 µm, 4.66 m^2/g, Nextech Materials, Lewis Center, OH) was screen-printed (mesh 325) after the preparation and the heat treatment on both sides of the symmetrical samples to serve as a current collector layer. The thickness of the current collector layer was determined to be 10 µm from cross-sectional HRSEM micrographs. The current collector layer was dried at 120°C for 2 hours.

3.4 Electrochemical characterization

High temperature Impedance spectroscopy

A high temperature electrochemical measurement setup was built for impedance spectroscopy measurements on symmetrical cells. A resistance tube furnace with appropriate diameter (90 mm) were used to homogeneously heat the sample. Considerations were taken in order to minimize electric and magnetic fields within the measurement chamber. The heating rods were coiled in a double manner around the alumina tube and direct current was applied. A 3 mm nickel iron alloy sheet was rolled up between heating elements and alumina tube as an additional shield for any magnetic field. The sample was positioned between two alumina pieces. The contact side of the alumina pieces was slotted to allow proper gas access to the sample. Platinum gauze (mesh 100) was used as a metallic electrode and two platinum wires were spot-welded on the gauze to serve as separate current and voltage probes to eliminate the possible electrical noises. In order to minimize the inductive effect of the electrical circuit the platinum wires connecting the sample to the impedance analyzer were chosen as short as possible. The platinum cables were shielded outside as well as within the chamber. An additional thermometer was positioned through the upper ceramic support 1 mm above the sample and enabled the precise temperature control to be within ±0.1 °C. Gas connections into the chamber facilitated the control of the gas composition during the measurements. Measurements at various partial pressures of oxygen were carried out by precise mixing of oxygen and nitrogen through mass flow controllers. An oxygen sensor was installed in the gas system prior to introduction into chamber to ensure the correct oxygen partial pressure. Electrochemical impedance spectroscopy was measured using a Solartron 1260 frequency response analyzer, recorded under open-circuit conditions (OCV), using a 20 mV amplitude AC signal over a frequency range from 0.05 Hz to 2 MHz. The measurements were performed in the temperature range from 350 and 850 °C at increments of 50 °C at oxygen partial pressures between 0.01 and 1 atm. All impedance measurements were made 1 h after the desired temperature was reached. The impedance data were analyzed using ZVIEW 2.80 software developed by Scribner Associates, Inc. After the electrochemical characterization the samples were fractured in order to determine the microstructure using HRSEM.

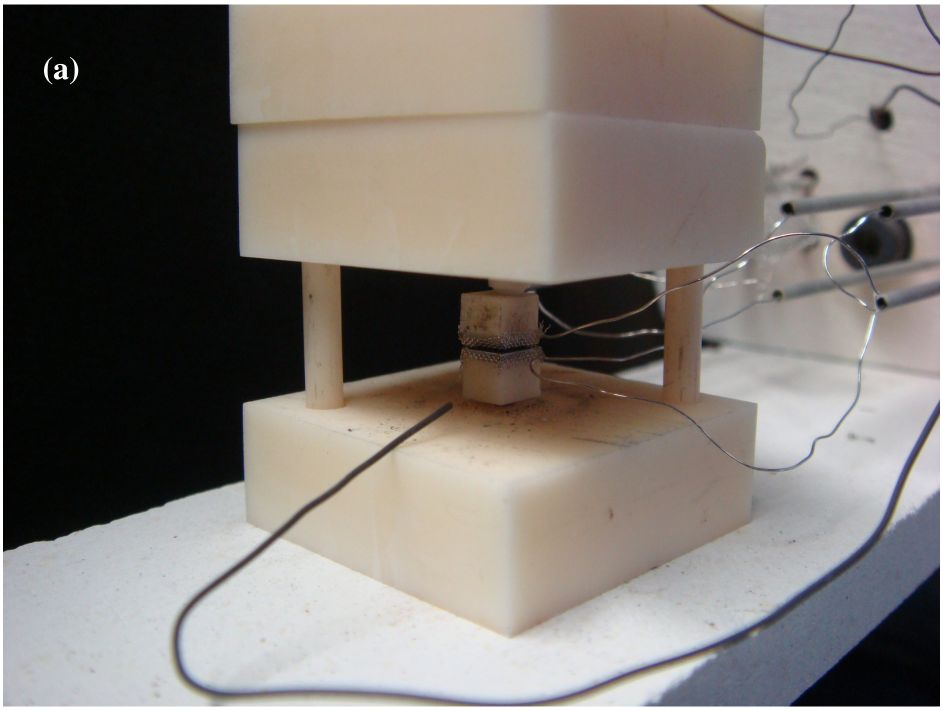

Figure 3-5: (a) High temperature impedance spectroscopy sample holder

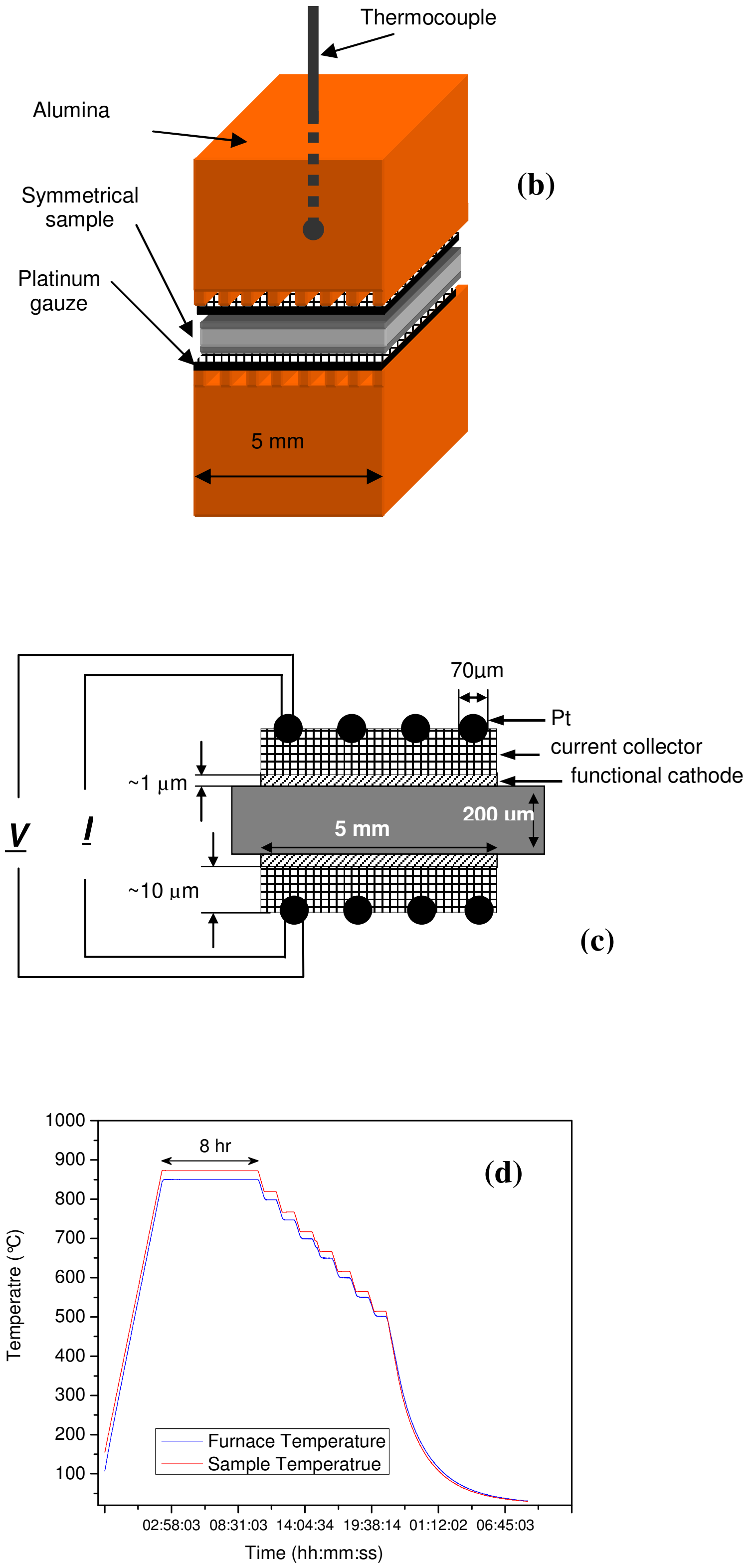

Figure 3-6: (a) and (b) High temperature impedance spectroscopy sample holder schematic, (c) Setup for two point impedance measurement with four electrical leads (not to scale), (d) Programmed tmperature profile for an impedance measurement.

Chapter Four

4 Synthesis of nanostructured cathode materials

The electrochemical behavior and performance of cathodes depends strongly on the characteristics of the cathode materials like chemical composition, phase purity, crystallite size and specific surface area. Consequently, the detailed characterization of synthesized samples is the basic principle for the interpretation of further experiments.

Within this chapter the results of chemical and structural characterization of nanostructured cathode materials synthesized via spray pyrolysis will be discussed. The analysis of chemical composition has been carried out by optical emission spectroscopy with induced coupled plasma and structural characterization has been investigated by X-ray diffraction as well as high temperature in-situ measurements. Morphology and texture of particles are investigated by scanning electron microscopy (SEM) and nitrogen adsorption.

4.1 Chemical composition

The results of the chemical analysis for the synthesized cathode materials in various batches are listed in Table 4-1. The chemical composition of the synthesized powder is especially important since small changes in composition lead to different doping levels of cathode material which subsequently causes a variation of the electrochemical properties as well as the ionic and electronic conductivity. It is of obvious importance that the chemical composition of the cathode films is exactly known and can be achieved in a controllable fashion during the synthesis as the electrochemical performance of the various films will be compared for the different compositions. The ratio of metal ions (La and Sr) is driven by normalization of the Manganese concentration to one. The results indicate a very slight deviation from the actual desired composition. These results were expected and confirmed the advantage of spray pyrolysis method which facilitates exact control on a certain stoichiometry in the final powder.

Table 4-1: Results of the chemical analysis obtained by inductively coupled plasma optical emission spectrometry for as synthesized samples. An

Sample	La/Sr/Mn concentration (mmol/L)	Real composition (La/Sr/Mn)
LSM06	(0.039: 0.0108: 0.053)	(0.743: 0.204: 1)
LSM07	(0.034: 0.009: 0.047)	(0.737: 0.193: 1)
LSM08	(0.037: 0.0098: 0.0484)	(0.763: 0.206: 1)

4.2 Morphology

Electron microscopy

The scanning electron micrographs of the as synthesized powder shown in Figure 4-1 represent the typical morphology of the ultrasonic spray pyrolisation. Generally, all samples consist of hollow spheres with thin shells. This is typically achieved by employing low concentration precursors. The size distribution of the hollow spheres is between 1 up to 5 µm. The main reason for the formation of wide distribution lies in the process technology of ultrasonic nebulization. The ultrasonic Interface (sapphire substrate) was charged permanently with the maximum feasible amount of precursor, which leads to formation of a very high droplet density in the gas phase.

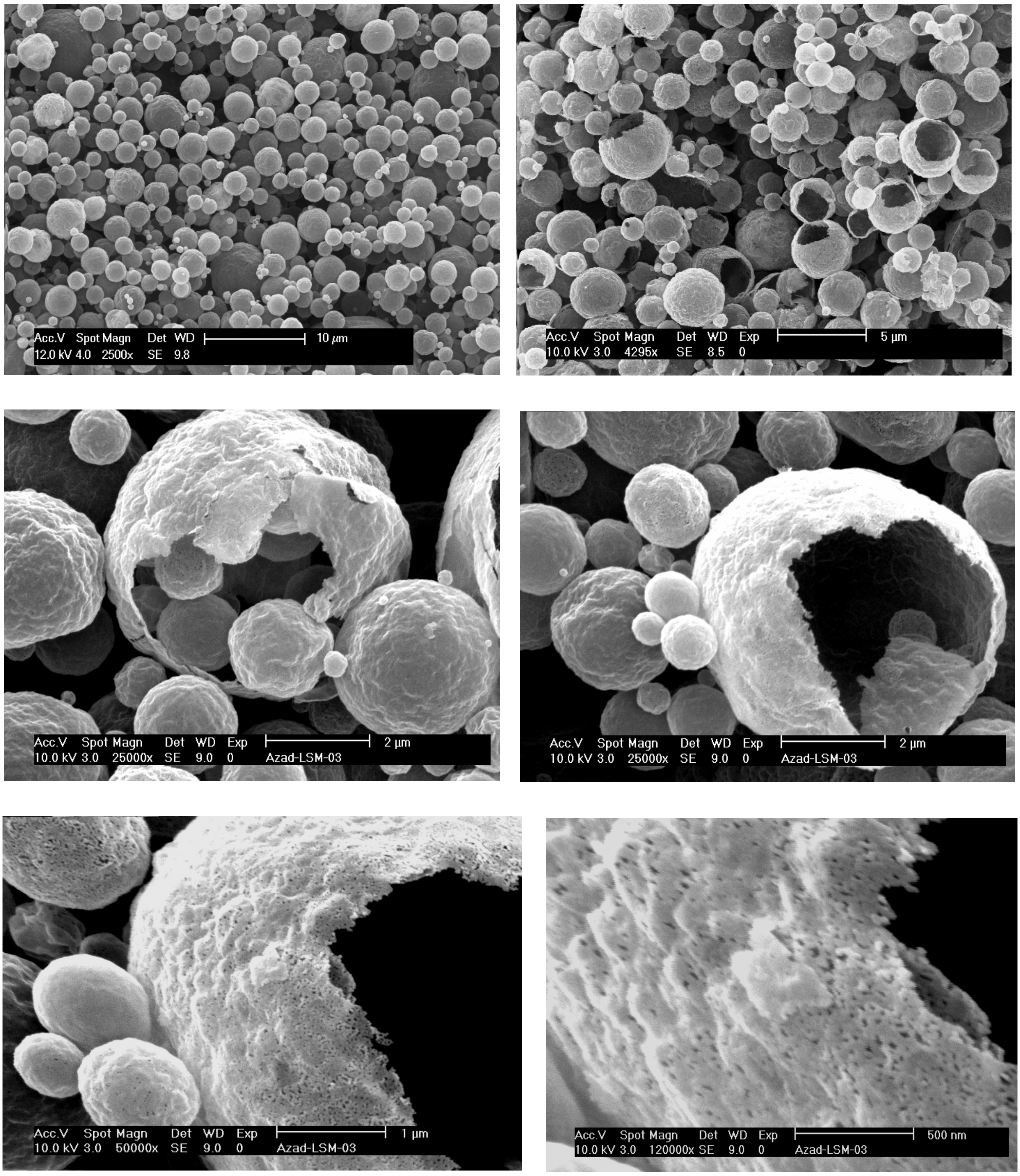

Figure 4-1: Scanning electron microscopy micrographs of as synthesized Lanthanum Strontium Manganate powders, indicating the hollow sphere morphology with nanosized shell. The porosity within the thin shell is evident at higher magnifications.

Thus, the mean free path of individual droplets decreases and the probability of coagulation between droplets on the way to the reaction zone increases. Apart from that, the nebulization performance of the ultrasonic processor can change after long synthesis times, which additionally contributes to time dependent droplet density in the gas phase and subsequently, polydisperse size distributions. As it is obvious from the SEM micrographs, the shells are partially broken which is an evidence for the high rate of evaporation of the precursor droplets in the reaction zone as well as low gas permittivity of precipitate which causes a high internal gas pressure within the droplet. Obviously, the internal gas pressure exceeds the mechanical strength of the shells and destructs the hollow spheres. At higher magnifications the thickness of the shells (10-20 nm) suggests that the crystallites within the shells are at least in one dimension nanometer-sized. SEM micrographs at higher magnifications clearly show porosity holes within the thin shells. The formation of porosity in the hollow spheres depends on the physiochemical properties of the precipitate, which confirms again the low gas permittivity. Figure 4-2a shows transmission electron micrographs of LSCF powders synthesized at 1200°C and heat treated at 750°C for one hour confirming the typically spray pyrolyzed morphology observed by HRSEM, consisting of hollow spheres with diameters in the range of 1-5 μm and very thin porous shells. Figure 4-2a shows an overview of two hollow spheres and broken shells. Two regions, marked with yellow boxes are presented at higher resolutions. Figure 4-2b is taken from the contact region of two hollow spheres, showing a cross section of the contact region between the two shells. The thickness of the shells is measured to be approximately between 10 to 15 nm. This confirms the result of the high resolution SEM images (Figure 4-1). Furthermore the micrograph (Figure 4-2d) shows no evidence of overlapping crystals within the broken shell and confirms the crystallite size determined from the Rietveld refinement (Figure 4-10) of LSCF powders synthesized at 1200 °C and subsequently heat treated at 750 °C to be below 20 nm. The broad rings in the electron diffraction shown in Figure 4-2e are indicative for the nanocrystalline nature and lack of texture in the as synthesized powder. The observation of cracks in thin shells just after ultrasonication of the dispersion for a few seconds suggests that the application of ultrasonic energy for longer time can lead to break up of the thin shells and, consequently, smaller agglomerate sizes. High resolution TEM images (Figure 4-2f) show excellent crystallinity and confirm the grain size values obtained from X-ray analysis. The chemical composition and compositional homogeneity of the as synthesized powder were examined by EELS and TEM-EDX methods (Figure 4-3). The results reveal nearly perfect achievement of desired composition. EELS and EDX mapping indicate a very good compositional homogeneity of metal ions within the thin shell microstructure.

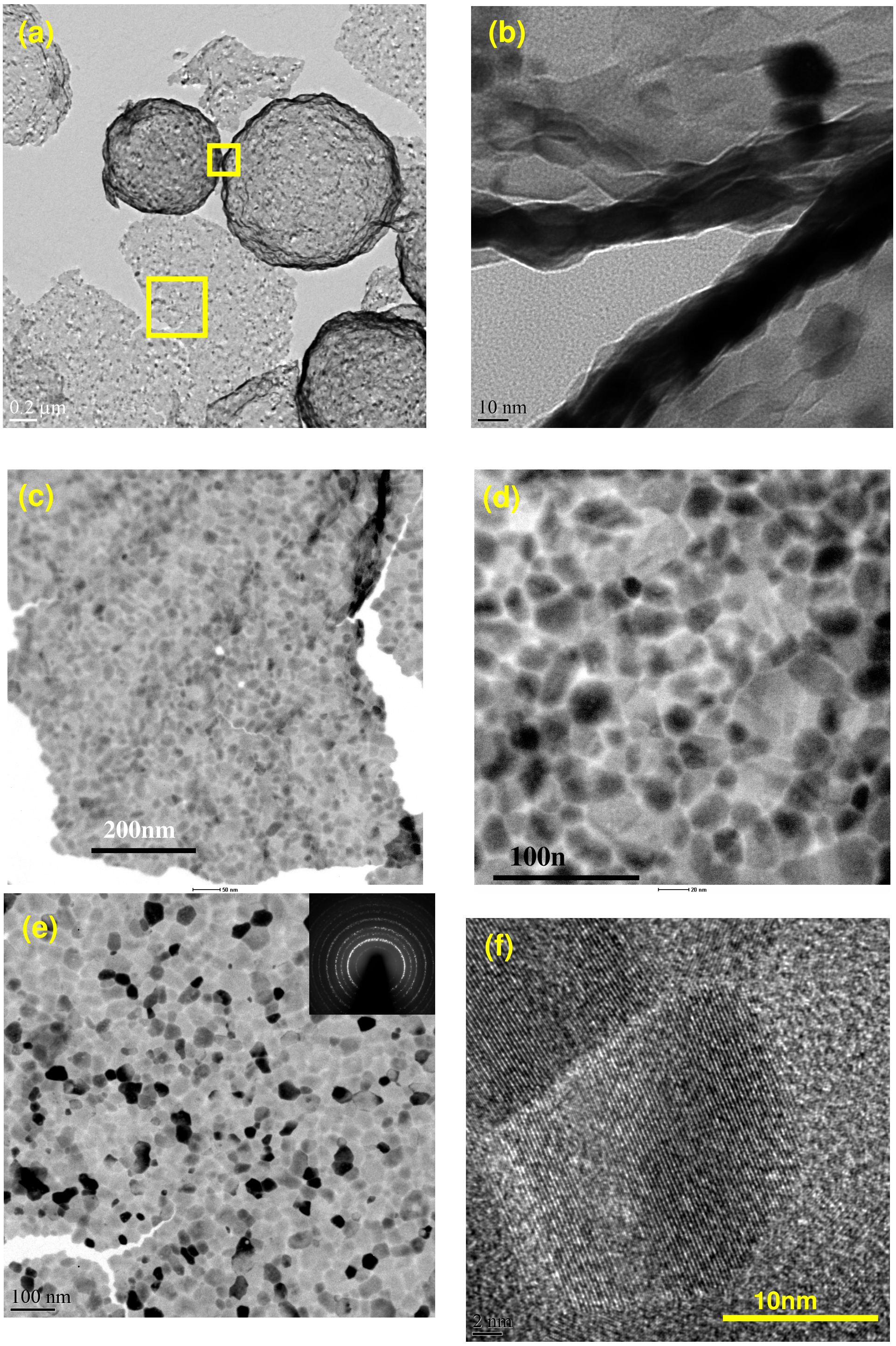

Figure 4-2: (a) Bright field transmission electron microscopy micrographs for as synthesized LSCF powder synthesized at 1200 °C, (b) Higher magnification image of (a) at the contact region of two hollow spheres, indicating the thickness of the shells, (c), (d) and (e) TEM micrographs of shell structure at various magnifications and electron diffraction pattern, (e) High resolution TEM image of nanocrystallie LSCF.

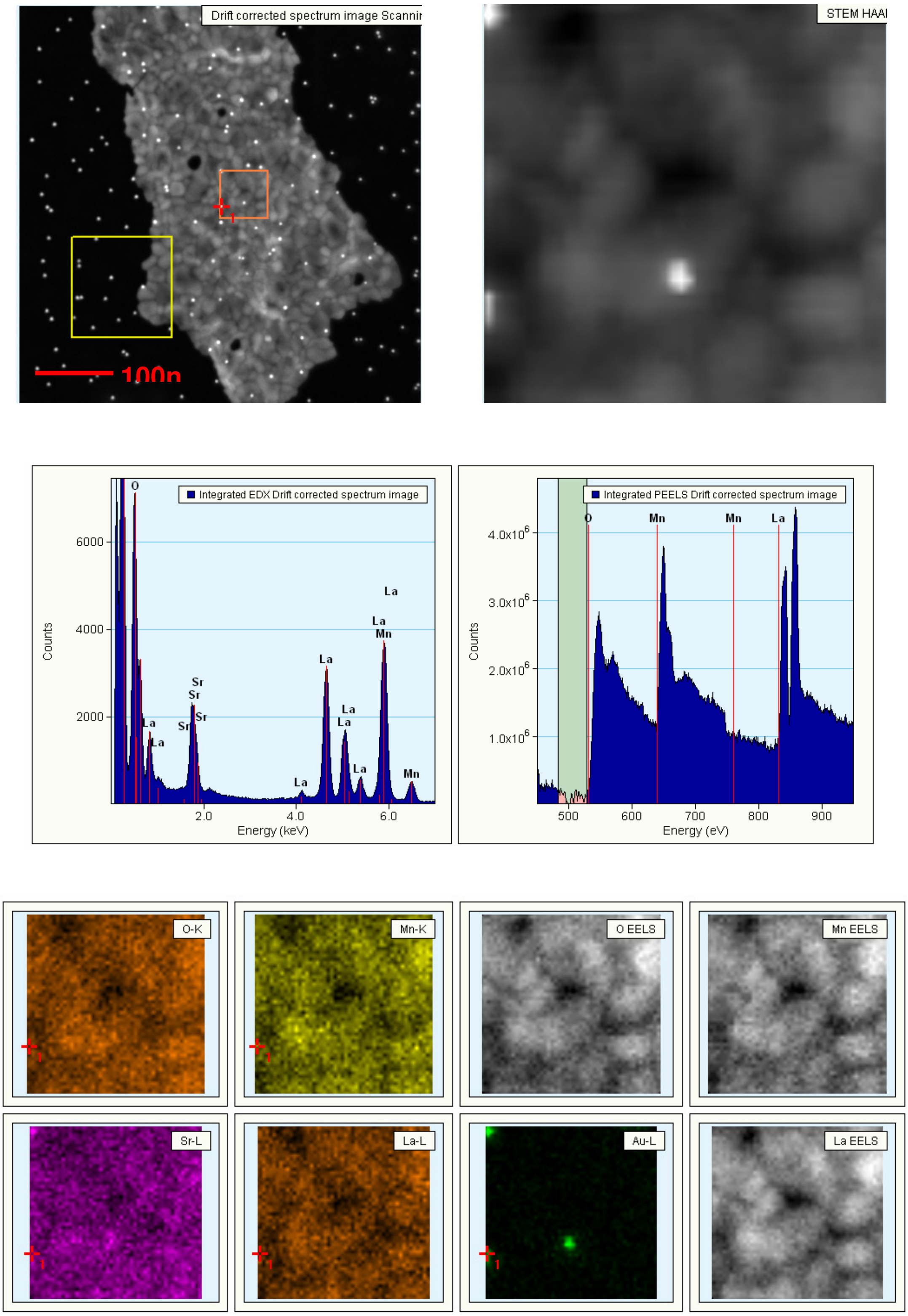

Figure 4-3: Results of energy dispersive X-ray spectroscopy and electron energy loss spectroscopy measured on as synthesized (at 1200°C) LSM sample.

Nitrogen adsorption

A key microstructural feature of the cathode material is a high specific surface area, since the electrochemical active areas within the cathode layers especially in mixed-conductive cathodes are the surface of the cathode particles. The specific surface area (SSA) of as synthesized LSM samples was measured by nitrogen adsorption. Table 4-2 presents the specific surface areas of powders synthesized at different reactor temperatures. As expected, an increase of the reactor temperature leads to lower specific surface area in nanocrystalline powder. For LSM, among the crystalline synthesized samples, the highest SSA value was obtained at 1000°C. Since the desired cathode material should possess highest SSA whereas certain crystallinity and phase purity, the final synthesis temperature for each material system was chosen by consideration of degree of crystallinty estimated from X-ray investigations, and SSA calculated from nitrogen adsorption.

Table 4-2: Specific surface area measured by nitrogen adsorption method for LSM powder synthesized at various temperatures.

Synthesis Temperature (°C)	1000	1050	1100	1200	1300
Specific surface area (m^2/g)	69	56	47	32	23

4.3 Structure

X-ray diffraction patterns of LSM powder synthesized at temperatures between 900 and 1200°C are shown in Figure 4-4. Below 900 °C, the powders were completely amorphous and no reflection was observed. At 950°C weak reflections appear, indicating crystallization of the powder. However, the weak intensity and the high intensity of the background suggest a low degree of crystallinity and the presence of a considerable amount of amorphous phase. At 1000°C, high intensity broad reflections are present indicating single phase nanocrystalline perovskite structure. Crystallization of perovskite structure is above 1000°C stable. By increasing the synthesis temperature, the FWHM of the reflections become smaller, indicating the formation of larger crystallites. In order to determine the grain size of the as synthesized powder at different temperatures, Rietveld refinement was carried out by using Pseudo-Voigt-curve approximation and constant background (Figure 4-5). Extracted grain sizes from Rietveld refinement for the LSM material system are summarized in Table 2-1. The results indicate a considerable increase in crystallite size above 1200 °C. 1000 °C was chosen as the optimum synthesis temperature for LSM material system since the obtained sample possesses the lowest crystallite size while a considerable phase purity (no secondary phase) is obtained.

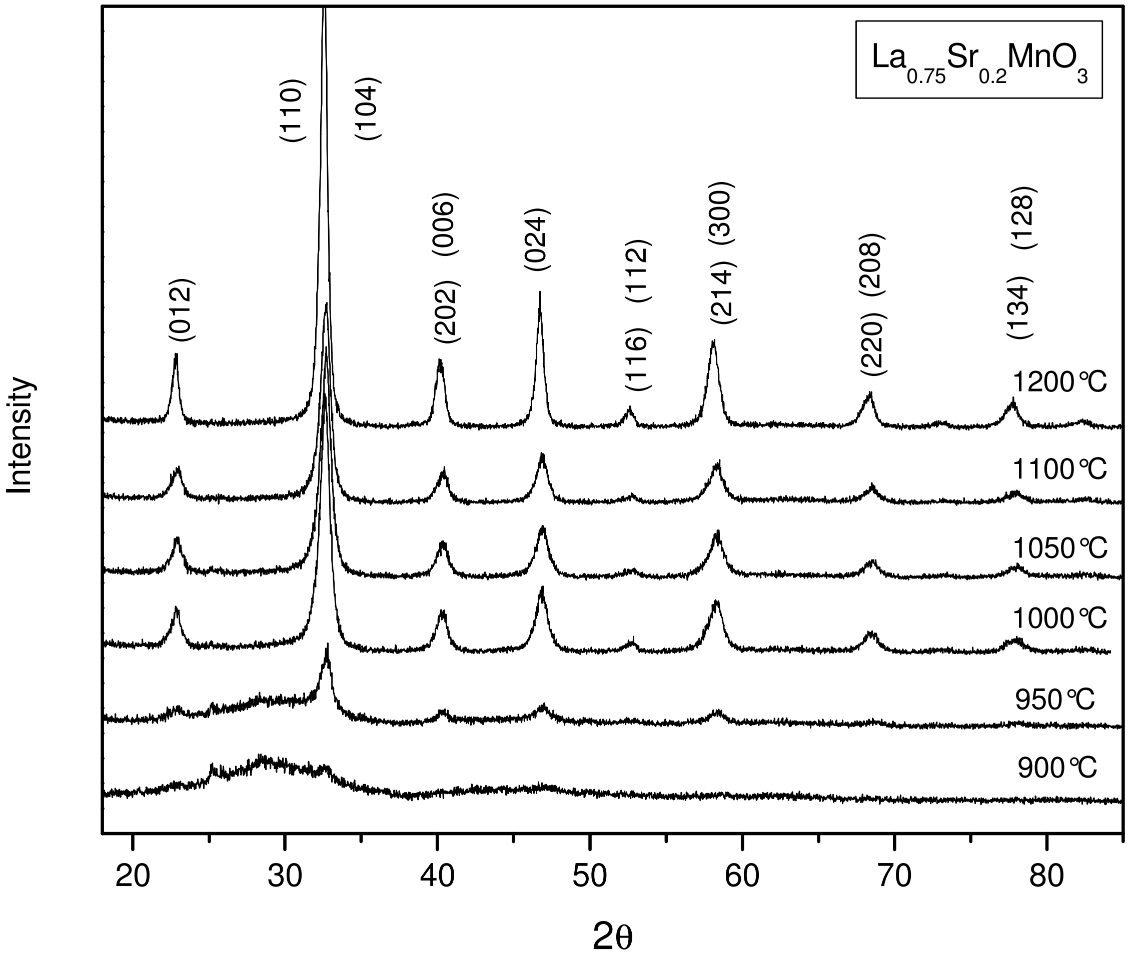

Figure 4-4: X-ray diffraction pattern of LSM samples synthesized at various reactor temperatures.

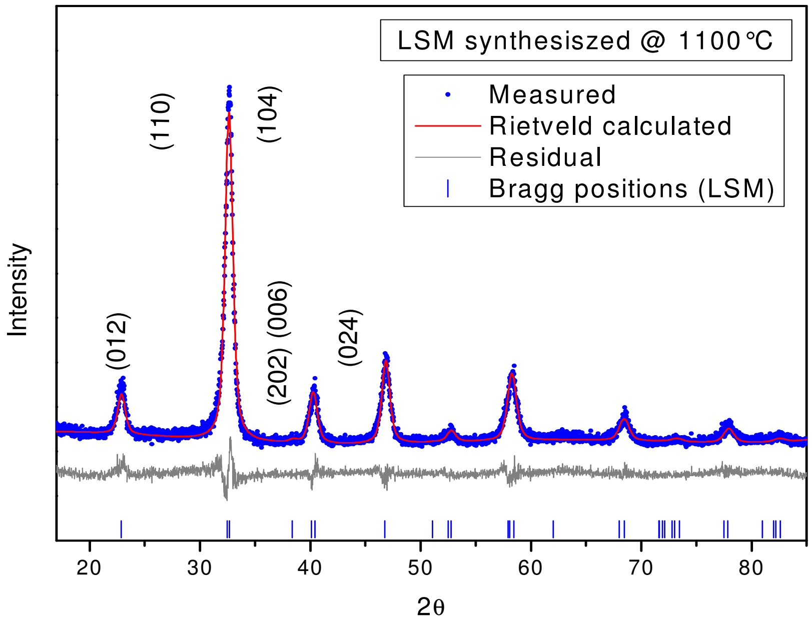

Figure 4-5: Characteristic diffraction pattern of a LSM sample synthesized at 1100 °C with the perovskite phase. The average grain size was determined by Rietveld refinement using pseudo-Voigt approximation and constant background.

Table 4-3: Effect of synthesis temperature (reactor) on LSM crystallite size

Synthesis Temperature (°C)	1000	1050	1100	1200	1300
Crystallite size (nm)	8	9	12	14	23

During the spray pyrolysis, the decomposition of the precursor and the formation of the peroskite phase occur in-situ in the reaction zone. Considering the carrier gas flow rate of 5 SLM, 2 cm inner diameter and 40 cm length of the tube furnace, a very short residence time for the precursor molecules and the particles is expected. Depending on the temperature of the reaction zone (900-1200 °C) a resident time of approx. 1/8 sec can be estimated. The high heating rate and short residence time could also mean that that the particles are not reaching the nominal reactor temperature, which in terms means that the phase evolution in equilibrium conditions (low heating rate) can occur at different temperatures in comparision to spray pyrolysis. In order to follow the phase evolution, several experimental techniques have been employed on the amorphous powder synthesized at 800°C. Thermogravimetry analysis (TG), differential thermoanalysis (DTA) were carried out on the fully amorphous LSM powder. A heating rate of 5 K/min was chosen for TG and DTA measurements. The measurements were performed in air in order to allow the complete

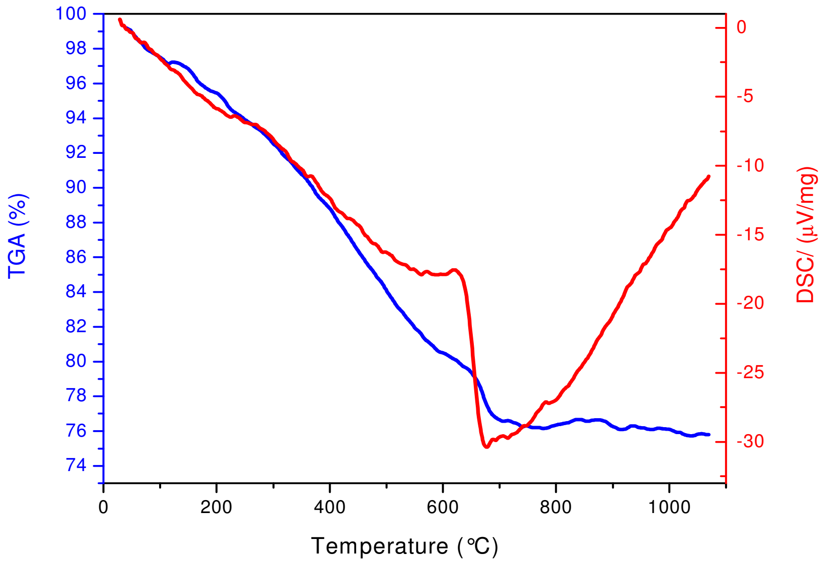

Figure 4-6: DTA-TGA measured for fully amorphous LSM sample synthesized at 800°C.

oxidation of the sample. Crystallization and phase formation of the fully amorphous powder was also studied by in-situ high temperature X-ray diffraction (HTXRD). In order to enable direct comparison with thermoanalysis data, an identical heating rate of 5 K/min was chosen as in the ex-situ experiments. The measurements were carried out under air atmosphere.

Differential thermal analysis shows small endothermic peaks below 200°C, which could be related to remaining moisture from the water based precursor during the synthesis. In this temperature range a total mass loss of 6% was observed. Further continuous and slow mass loss was observed up to 550°C which coincide with small exothermic peaks. This could be related to the decomposition of remaining organics. With increasing temperature a rapid mass loss of 4% was observed between 600 and 700°C. In the same temperature range a strong exotherm signal with a maxima at 675 °C was measured. This temperature assigns the complete crystallization of the powder. Above 700 °C there was neither distinct mass loss nor signal in DTA curve. A total mass loss of 24% was recorded for whole measured temperature range. An overview of the data obtained by HTXRD of the amorphous sample is shown in figure 4.b. The crystallization of powder begins at 560°C and completes at 696°C. This is in a good agreement with the DTA results. The phase formed at this time-temperature profile can be identified as a Trigonal with space group of ICSD#R-3C (167). With increasing temperature, the FWHM of the reflections decreases, which is most likely an effect of grain growth processes. The considerable difference between the decomposition and the synthesis temperature of LSM powder originate from the short dwell time of droplets within the reaction zone. At a reaction zone temperature of 800 °C sufficient thermal energy is provided in order to evaporate the majority of the water.

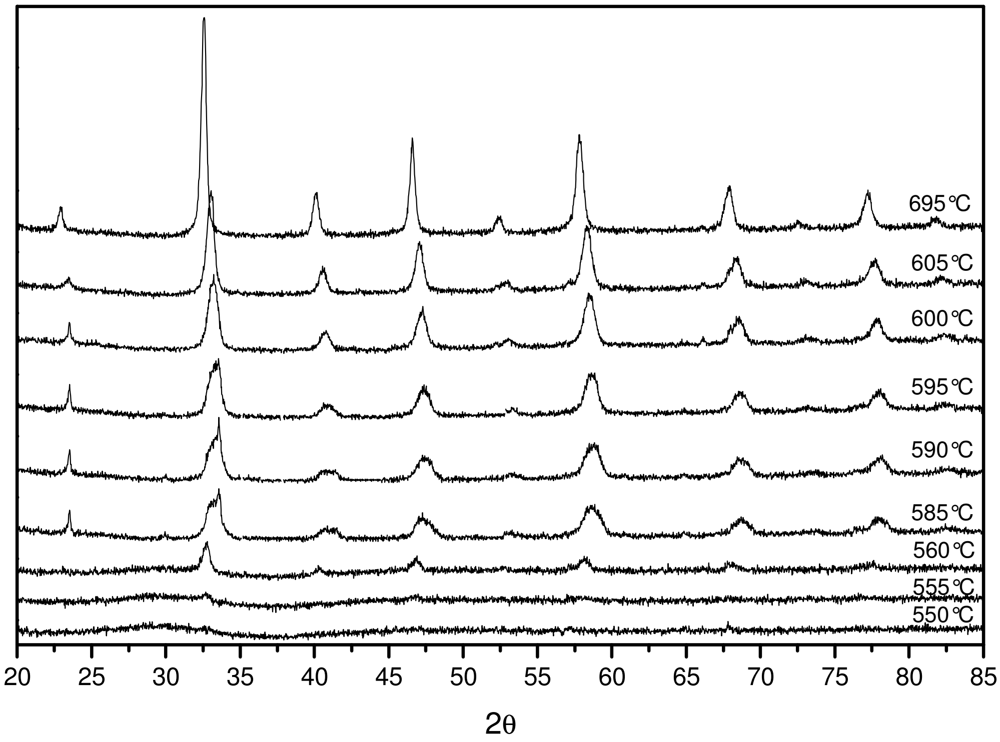

Figure 4-7: In-situ high temperature X-ray diffraction of amorphous LSM sample synthesized at 800°C

However, the particles leave the reaction zone before they reached their decomposition temperature. Therefore, a higher temperature e.g. 1000°C is required for fully decomposition and crystallization of powder. X-ray diffraction patterns of LSCF powder synthesized at temperatures between 900 °C and 1300 °C are shown in Figure 4-8. The desired perovskite structure (ICSD#R-3C(167)) is already present predominantly even at the lowest synthesis temperature of 900 °C. A minor secondary phase identified as the orthorhombic secondary phase (ICSD#62, pmcn) of strontium carbonate is observed at the lower temperatures. The formation of strontium carbonate during synthesis of LSCF was observed also by other researchers [108-110]. The Rietveld refinement in Figure 4-9 shows that only two phases are present both in nanocrystalline form. The crystallite size of the perovskite phase as well as the secondary phase in the as prepared powder depends on the synthesis temperature. Table 4-4 summarizes the crystallite size of LSCF and $SrCO_3$ phases determined from Rietveld refinement for the powders synthesized at 900, 950, 1000, 1100, 1200 and 1300 °C, respectively. Table 4-5 presents the R values for Rietveld refinements, indicating the quality of the fits. It is obvious that the synthesis at higher temperatures leads to larger grain sizes for the perovskite phase. Interestingly, in contrast to the LSCF phase, the grain size of the minor secondary phase ($SrCO_3$) decreases in powders synthesized at higher temperatures. Rietveld refinements indicate that the LSCF powder synthesized at 900, 1000 and 1200 °C contains 14.7, 11 and 5 weight percent strontium carbonate, respectively.

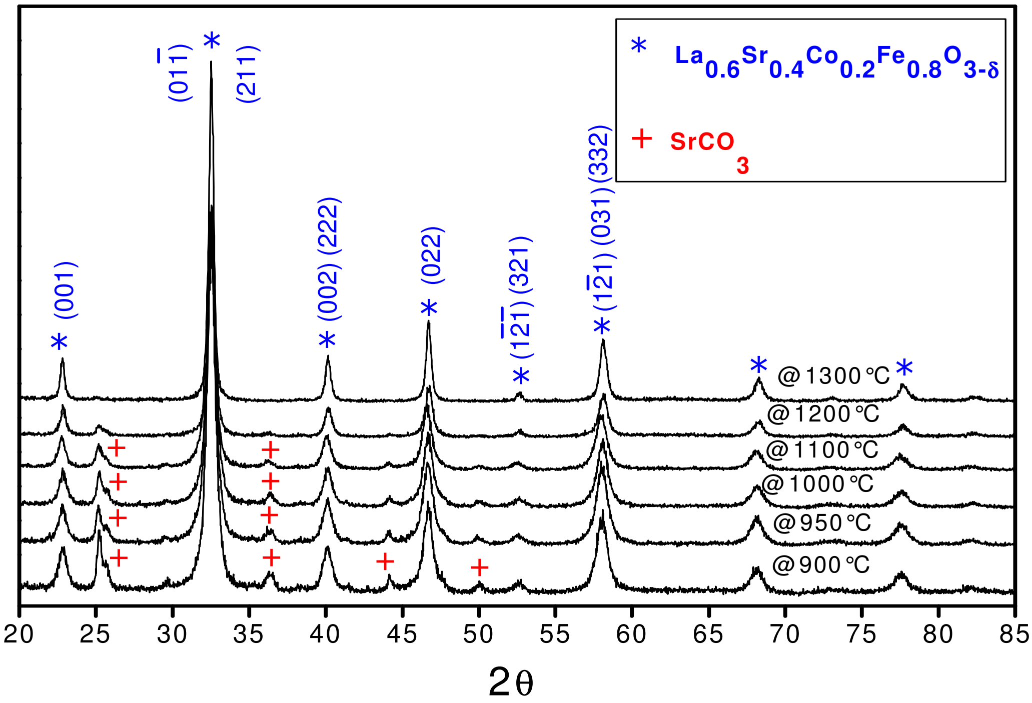

Figure 4-8: X-ray diffraction pattern of LSCF as synthesized samples at various reactor temperature

Obviously the synthesis at higher temperatures leads to better a decomposition of $SrCO_3$ and, consequently, an increasing content of the primary phase. The decrease of both grain size and weight percent of nanocrystalline strontium carbonate with increasing synthesis temperature reveals that the minor secondary phase is well dispersed in the LSCF matrix.

LSCF powder synthesized at 1300°C contains no secondary phase detectable by X-ray diffraction. Alternatively, $SrCO_3$ decomposes during extended heat treatment for 1 hour at 750 °C of powder synthesized at 1200 °C as shown in Figure 4-10. The results indicate that total decomposition of strontium carbonate during heat treatment takes place below 750 °C while the nanocrystallinity ($\leq$ 20 nm) of the perovskite phase is retained. The thermal decomposition of pure SrCO3 is reported in the literature to occur between 900 and 950 °C [111]. However, there are studies investigating the decomposition of $SrCO_3$ not only as pure powder but also as a mixture with other oxides, like TiO2 [112]. Thermoanalysis shows that the decomposition of SrCO3 in mixed powders occurs at considerably lower temperature than in pure state. Roy et al. suggested reactions between two phases in mixed powders at lower temperatures than the decomposition temperature of pure $SrCO_3$ [113]. Most likely a similar phenomena is being observed in the present case of the LSCF-$SrCO_3$ mixture. Additionally, as it is evident from X-ray studies, in the present powder, $SrCO_3$ exists as nanocrystalline phase dispersed in the LSCF matrix. Due to the high specific surface area of the nanocrystallites, the diffusion lengths are considerably shorter and diffusional processes can occur much faster than in the microcrystalline counterparts. In case of the LBSCF material system (Figure 4-11) the formation of strontium carbonate is more pronounced at synthesis temperatures below 1100 °C. This could be due to the higher strontium content in the precursor composition. However, powder synthesized at 1200 °C contain only 5 wt%. and at 1300 °C a single phase perovskite structure is achieved. X-ray investigations of LBSCF powder reveal that the complete decomposition of the secondary carbonate phase requires temperatures higher than 800 °C, moderately more than in the LSCF case.

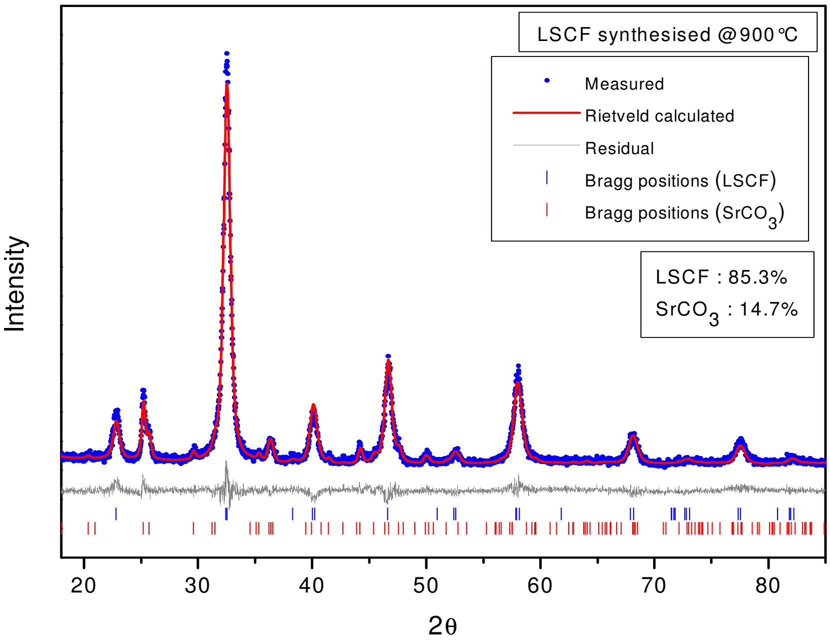

Figure 4-9: Rietveld refinement of LSCF sample synthesized at 900°C

Table 4-4: Crystallite size of present phases in synthesized LSCF powder at different temperatures

Synthesis Temperature (°C) Crystallite size (nm)	900	950	1000	1100	1200	1300
Perovskite (LSCF)	**10**	**10**	**10.4**	**11.5**	**15.5**	23
$SrCO_3$	19	17	16	14	13	-

Table 4-5: R-values for Rietveld refinements; the profile (R_p), the weighted-profile R value (R_{wp}), the expected (R_{exp}), the goodness of fit (G.O.F) and [114].

R factors	R_p	R_{wp}	R_{Exp}	G.O.F	D-WD
LSCF @900°C	10.16	13.75	11.89	1.16	1.53
LSCF@1200@750°C	11.98	16.82	13.37	1.26	1.37

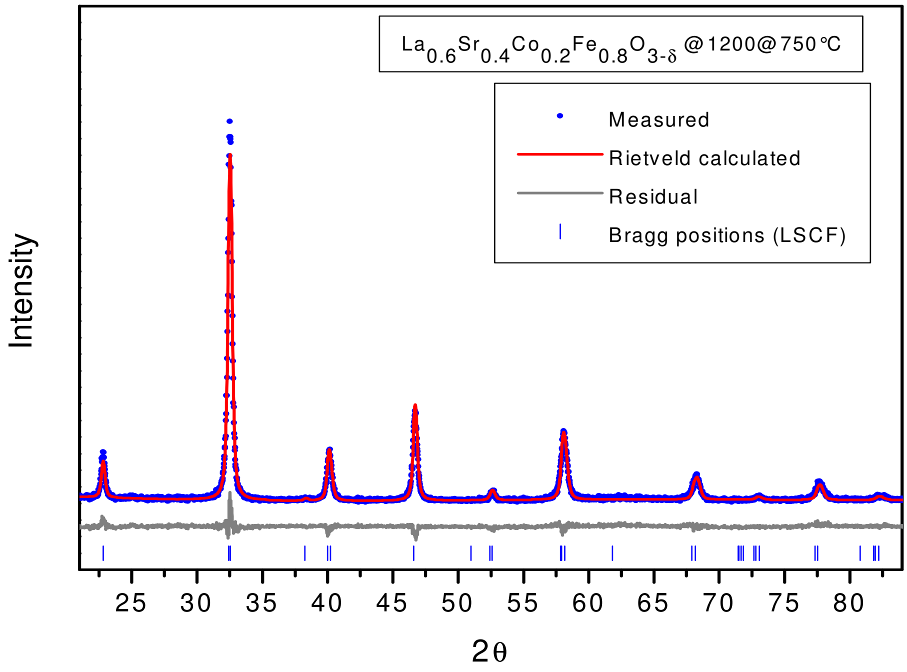

Figure 4-10: Rietveld refinement of LSCF sample synthesized at 1200 °C and heat treated at 750 °C for 1 hr.

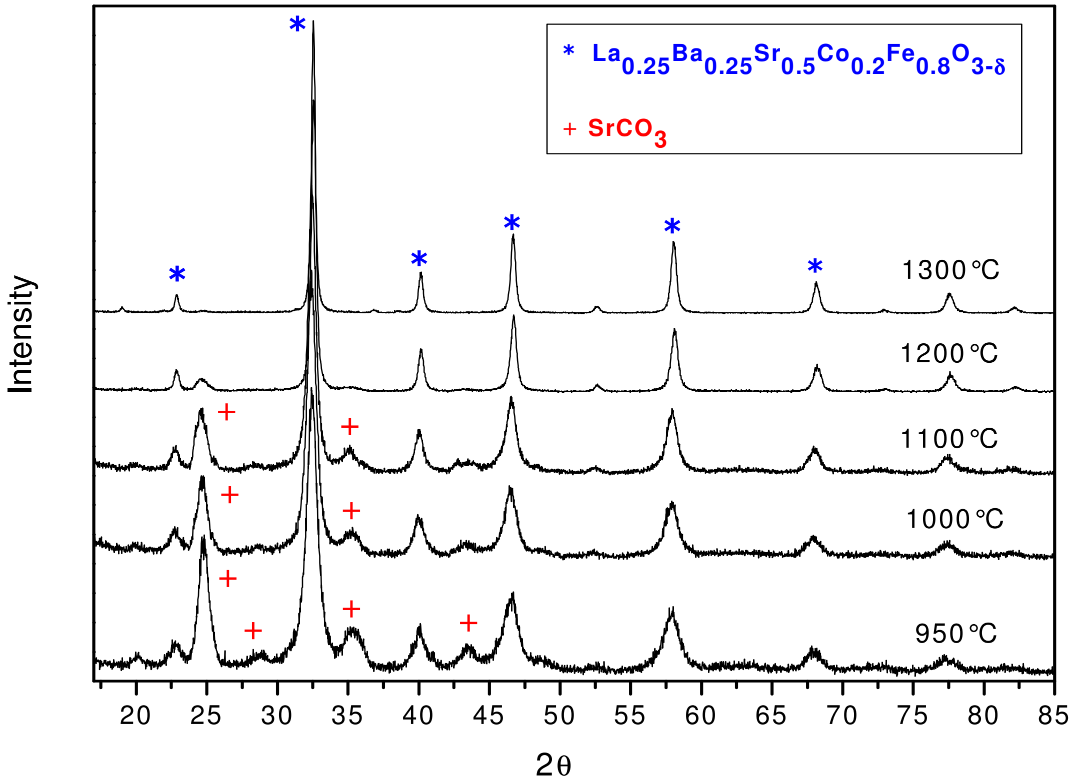

Figure 4-11: X-ray diffraction pattern of LBSCF synthesized at various reactor temperatures.

Chapter Five

5 Morphological studies and thin film cathodes

5.1 Formation of hollow spheres

As discussed earlier, spray pyrolysis from water based precursors of LSM, LSCF and LBSCF yields hollow spheres morphology. The spheres are partially broken and porosity within the thin shell is observed. A part of the hollow spheres are not in perfect shape and broken to smaller flake like pieces. The breakup of the hollow spheres is indicative of the fast evaporation process of the solvent, which in connection with the low permeability of the precipitated material leads to a high pressure inside the droplet. Obviously, this pressure exceeds the mechanical stability of the thin shell which breaks up into small pieces.

The physical and chemical characteristics of soluble chemical precursors strongly influence the characteristics of particles formed by spray pyrolysis. Unlike most solution-precipitation processes where the metal ions are precipitated as sparingly soluble salts (e.g., hydroxides, oxalates, or carbonates), the dissolved precursor salts precipitate during the evaporation stage of the spray pyrolysis. As shown later, the salt solubility and the degree of supersaturation influence whether solid or hollow particles are formed during the evaporation stage of spray pyrolysis. Charlesworth

and Marshallz [115] summarized how the permeability and the thermal character (melting and boiling point) of metal salts affect particle morphology when the boiling temperature of the solvent is exceeded. For example, thermoplastic salts readily inflate, whereas impermeable, rigid particles simply fracture into shell fragments once the solvent boils. The thermal properties of the precipitated precursors also impact subsequent particle evolution during the thermolysis stage. For example, many metal nitrates have low melting temperatures (e.g., < 200°C). If the metal salt melts during thermolysis, then the reduction of the product gas permittivity through the molten salt results in an internal gas-pressure increase and "explosion" or foaming of the particle. This process leads to hollow particles or particle fragments of a broad particle-size distribution [97, 98, 116].
The scanning electron micrographs of LSM powder synthesized at 1200°C shown in Figure 5-1 is a representative morphology of particles synthesized via spray pyrolysis. The powder consists of hollow spheres with thin shells, which were originally droplets of precursor solution with low concentration. The size distribution of the hollow spheres (diameter) is polydispersed with a size range from submicrometer to 5 micrometer. The size of the hollow spheres depends on various parameters given by a related. A simple relation for the size estimation (d, particle diameter) of particles produced by ultrasonic is presented by Lang [117].

$$d = 0.34\left(\frac{8\pi\sigma}{\rho f^{2}}\right)^{1/2} \qquad 5.1$$

σ : Surface tension (dyne/cm)

ρ : Concentration (g/ml)

f : Ultrasonic frequency (Hz)

A constant ultrasonic frequency of 1.7 MHz was provided by the ultrasonic power supply and concentration of all precursors are set at 0.1 mol/l. Overview micrographs of LSM powder synthesized at 1200°C are shown in Figure 5-1a. The size of particles (diameter of the hollow spheres) was determined by software Lince. The size distribution is shown in Figure 5-3, fitted by a Normal distribution function.

$$f(d) = A\exp\left(-\frac{1}{2}\frac{(x-\mu)^{2}}{2\sigma^{2}}\right) \qquad 5.2$$

where μ is the average particle size (diameter) and σ is the standard deviation. The fitting results are shown as solid lines. For the powder synthesized at 1200°C and 0.95 bar (pressure of nebulization chamber) a mean size of 1.71 μm is obtained (Figure 5-3a). However, a wide size distribution is present. The main reason for the nonuniformity in morphology and formation of widely distributed particle sizes lays in the high slope of the temperature profile within the reaction zone. The precursor was supplied onto the ultrasonic interface with the maximum possible flow rate, which leads to high droplet concentration in the gas phase. Thus, the mean free path of the individual droplets is reduced and the probability for coagulation of droplets on the way to reaction zone increases. Liquid droplets can undergo coagulation- a process by which two or more droplets collide and coalesce into a larger droplet. There are no reports in the literature concerning the importance of coagulation phenomena on particle size and morphology development. However, the dynamics of coagulating droplets (or particles) are well understood. The decrease of the particle number density, associated with an increase in the average droplet size, can be described by [97]:

$$\frac{N_t}{N_0} = \frac{1}{1 + t/\tau_c} \qquad 5.3$$

where N_0 is the initial number of droplets, N, the number of droplets at time t, $\tau_c = 2/\beta N_0$ the characteristic coagulation time constant, and β the coagulation (collision) rate constant, where Brownian motion is assumed to be the reason for droplet collision and β is assumed to be constant. Both of these assumptions are reasonable and allow for an estimate of droplet coagulation times as a function of size and number density. The coagulation time is relatively strongly dependent on the initial number density of droplets; the higher the initial number density, the faster is droplet coagulation.

Effect of number density of droplets

In order to study the effect of number density of droplets on the size distribution, LSM powder was synthesized at lower precursor supply rate with all other parameters kept constant. At a constant carrier gas flow rate the reduction of the precursor supply rate results directly in a lower (initial) droplet density number.

Figure 5-1e and f represent the resulting morphology. The size of particles (diameter of hollow sphere) was estimated by software (Lince) and the size distribution is shown in Figure 5-3b. The mean size is reduced to 1.21 μm. More significant is the narrowing of the size distribution obtained after reducing precursor supply rate. The width obtained from fitting the size distribution by Gaussian function reduces from 2.07 to 1.08 μm. This confirms the considerable effect of initial droplet density on the coagulation and formation of broad size distribution.

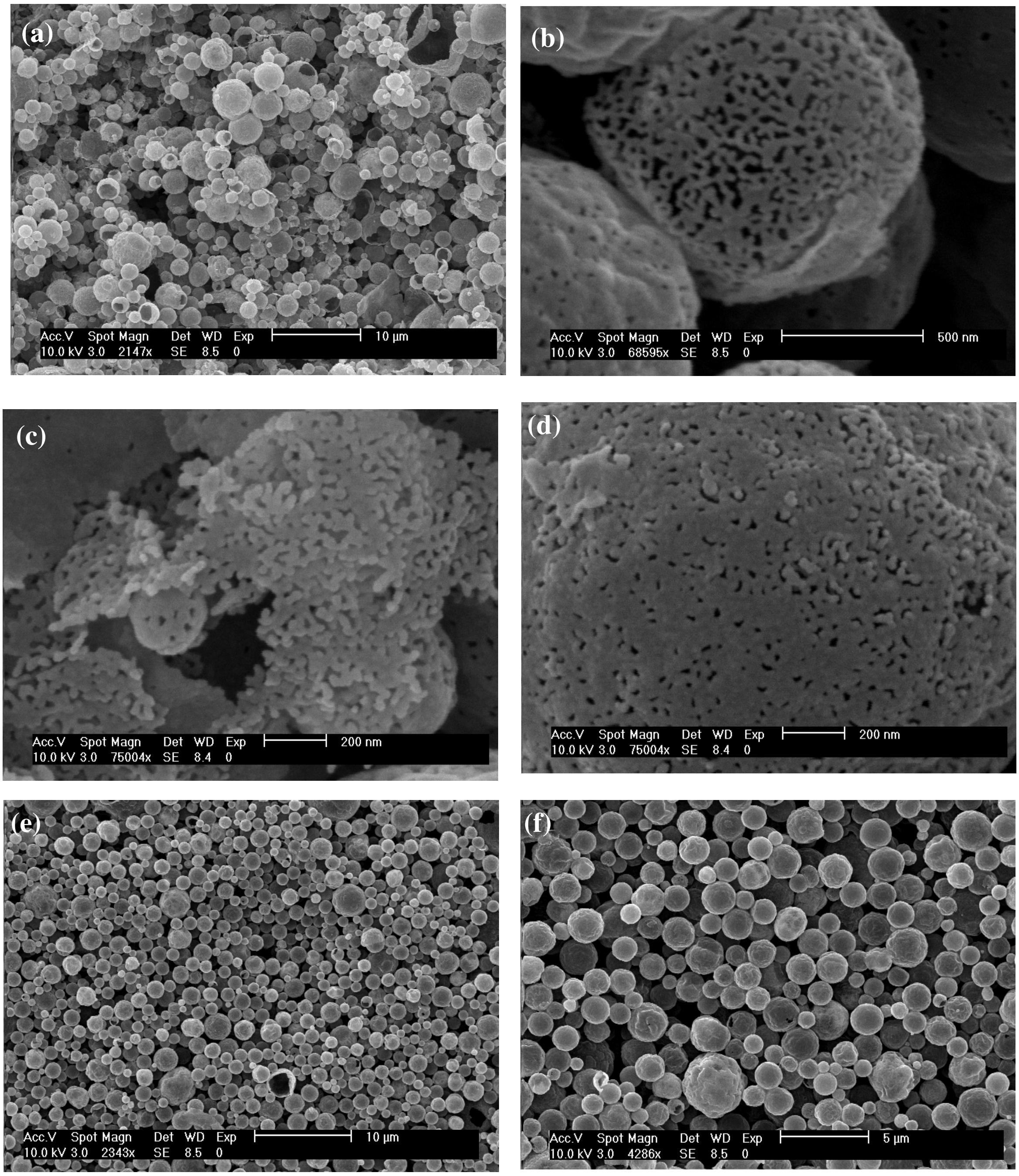

Figure 5-1 (a) As synthesized LSM powder (at 1200°C) with hollow sphere morphology and polydispersed size distribution, (b),(c) and (d) nanoporous structure of the shells of the spherical particles, (e) and (f) effect of lower precursor supply rate (lower droplet number density in aerosol on size distribution of hollow spheres

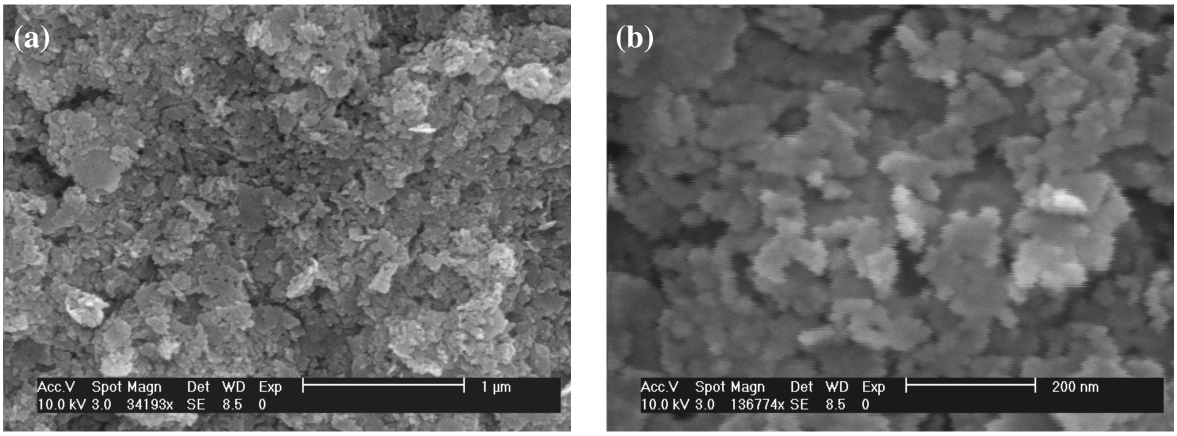

Figure 5-2 (a) (b) Total breakup of hollow sphere morphology into flake like nanoparticles as an effect of reactor pressure.

Effect of pressure and precursor concentration on morphology

A comparison of the evaporation rate and temperature change of liquid droplets and solution droplets is helpful in identifying the effect of the solute on particle formation by SP. The evaporation of liquid droplets has been extensively studied and modeled for combustion processes and atmospheric phenomena. The derived models form the foundation for calculating the rate of change of droplet-size change as a function of temperature and relative humidity in the initial evaporation stage of SP. The rate of evaporation of droplets moving with the same velocity as the ambient is given by [118]:

$$\frac{dm}{dt} = \frac{4\pi R D_V M}{R_g}\left(\frac{p_\infty}{T_\infty} - \frac{p_d}{T_d}\right) \qquad 5.4$$

where p_∞ and T_∞ are the ambient vapor pressure and temperature of the reactor, respectively. The subscript “d” refers to the same parameters at the surface of the droplet, *M* is the molecular weight of the gas and R_g is the gas constant, *R* is the radius, and m mass of the droplet. Fuchs [119] noted that Eq. 5.4 neglects the initial change in the surface vapor concentration and the change in the droplet radius. According to Equation 5.4 the decrease of the vapor pressure within the reaction zone leads to higher evaporation rate in the droplet at a constant temperature. In case of a formation of precipitant layer with low permeability a higher evaporation rate results in a higher vapor pressure inside the droplet. The increased gas pressure in the droplets yields a higher pressure on the precipitant shell and this enhances the probability of breakup of the shell resulting in smaller particle sizes. In order to study the effect of gas pressure within the reaction chamber, the pressure was decreased from 0.95 atm to 0.3 atm. The carrier gas flow was reduced accordingly to maintain the residence time of the droplet constant. Micrograph 5.2c represents the morphology obtained under reduced gas pressure. It is evident that the hollow spheres microstructure break up completely to flake (Figure 5-2). The size of particles was estimated by software (Lince) and the size distribution is shown in Figure 5-3c. The mean size of 270 nm, obtained from fitting, indicates substantially reduction in particle size.

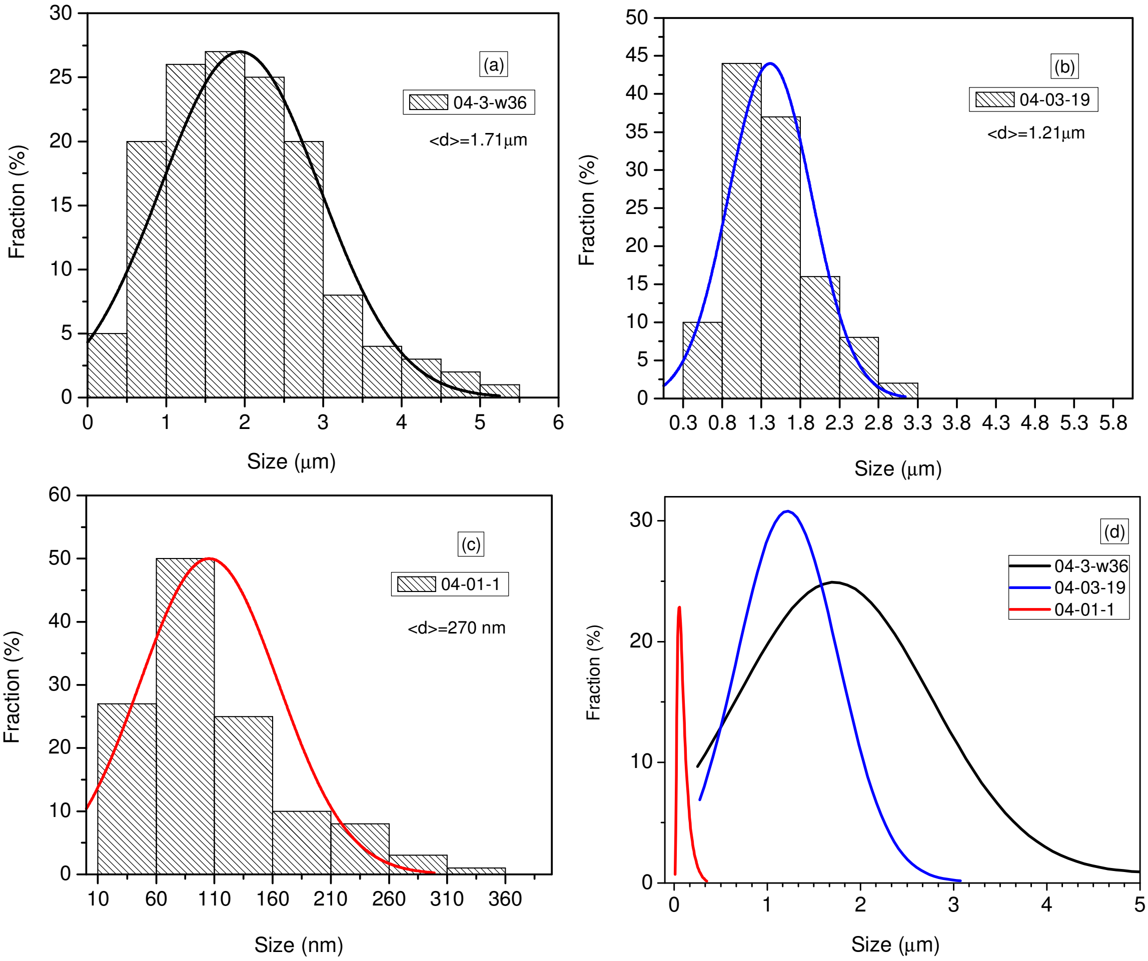

Figure 5-3 Size distribution of as synthesized LSM powder under different parameters, (a) under reactor pressure of 0.95atm, (b) low precursor supply rate, (c) under low reactor pressure, (d) size distribution comparison among samples synthesized under different conditions

Morphology modification

The morphology of as synthesized powder exhibits a high specific surface area up to 70 m2/g. However the hollow sphere morphology is not beneficial for further processing into functional cathode layer. Hollow spheres in contact with the electrolyte do not provide higher three phase boundary zones in comparison to micropowders. As discussed earlier, the electrochemical active zone can be increased most effectively by a reduction of the particles size. Therefore, an optimization of the initial morphology is required. High resolution electron microscopy has shown considerable formation of porosity within the thin shell of the spheres. This porosity together with the small thickness of the shell results in a brittle behavior and consequently shells can be early broken. This is observed in the TEM samples which were prepared by ultrasonication of the dispersions. The hollow spheres break into smaller flakes after short periods (few seconds) of application of ultrasonic energy (Figure 5-4a and b). The nanocrystallites in the thin shells are not completely sintered together and showing only small sintering necks. Consequently, the as-synthesized powders were dispersed in water and treated with ultrasound for different time.

Figure 5-4c and d show the microstructure of LSM powders after 30 seconds exposure to ultrasonic energy. It is evident that the hollow spheres are mostly broken into flakes like structures. Particle size measurements reveal also considerable size reduction after longer application of ultrasonic treatment (up to 2 minutes) which leads to complete destruction even of the flakes to small agglomeration of initial nanoparticles. It is evident from the micrograph that the thin shells are broken up into very fine particles with sizes in the range of 20 nm to 50 nm (Figure 5-4e and f).

5.2 Characterization of nanodispersions

Due to the charging of the particles after break up in the ultrasound treatment, the particles tend to agglomerate and settle in form of large agglomerates. Consequently, the stabilization of the nanoparticles in the water based dispersion is the first step using dispersions in further processes. In order to stabilize the nanoparticles, the surface potential behavior of the particles in dependence of pH value in dispersion media was studied by Zeta Potential measurement. Figure 5-5a shows the Zeta Potential measurement for LSM dispersion. The highest surface potential of a LSM in water was found to be -38.5 mV at pH =10.2. According to the literature the repulsive Coulomb force between the particles with a surface potential above 30mV is sufficient to avoid the agglomeration. The electrostatic approach works well for short times, however for further processing, typically a long-term stabilization is needed.

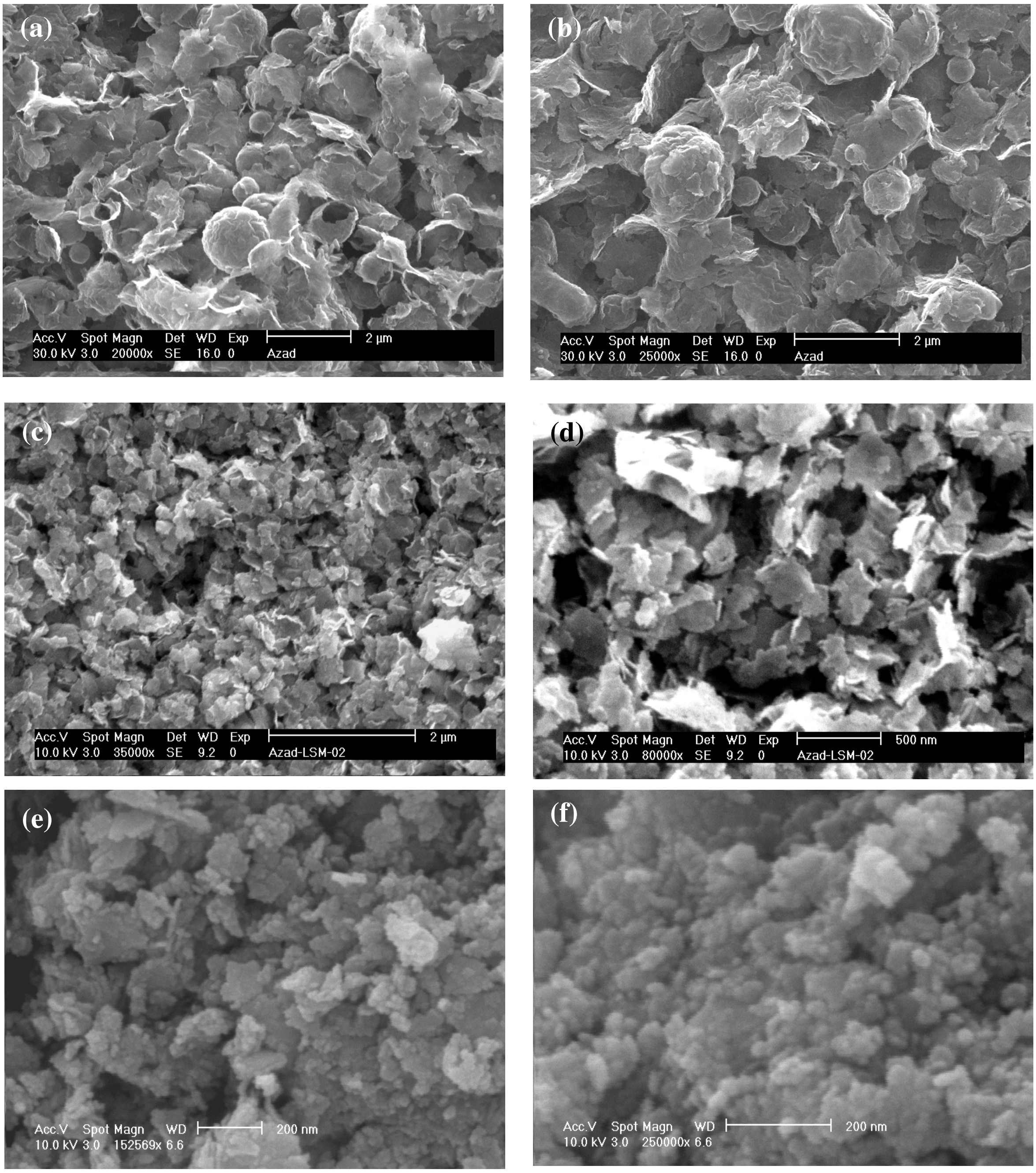

Figure 5-4 Effect of duration of ultrasonication process on powder morphology, from hollow spheres into nanoparticles. (a) and (b) after 5 seconds, (c) and (d) after 30 seconds, (e) and (f) after two minutes.

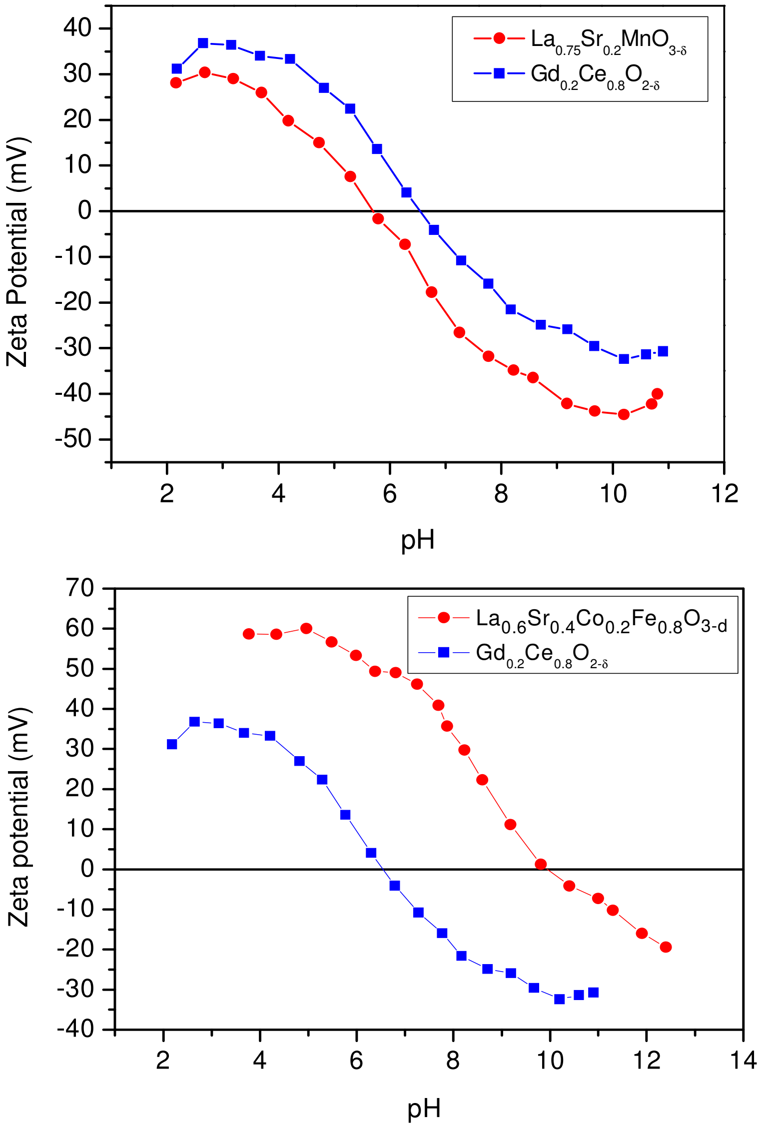

Figure 5-5 Surface potential of LSM, LSCF and GDC nanoparticles in water-based dispersions versus pH value.

This can be achieved by the use of organic molecules.. Therefore, various organic dispersing agents were added to the LSM dispersion and Zeta potential was measured. Among several organic agents, KX9009 (Zschimmer&Schwarz GmbH, Lahnstein, Germany) effectively fulfilled stabilization of LSM nanoparticles in deionized water. The Zeta potential measurement of LSM after addition of KX9009 shows an increase in the surface potential. The maximum surface potential of -44.6 mV was observed without significant shift (in pH axes) at pH=10.2. The high surface potential in basic conditions, facilitates the stabilization and preparation of stabilized LSM dispersions. The particle size distribution in stabilized LSM dispersions was measured by the dynamic laser scattering method. The result is presented in Figure 5-6a. The fitting with a Gaussian function reveals a mean particle size of 43 nm.

The Zeta potential measured for LSCF particles dispersed in deionized water after using organic additive (KX9009) is shown in Figure 5-5b. The highest surface charge for LSCF in deionized water, approx. 60 mV, was found in the range of $4.1 \leq pH \leq 4.9$. An almost identical surface potential behavior for LBSCF particles was observed. Therefore, the stabilization of LSCF and LBSCF in contrast to LSM particles was accomplish in acidic environment. The mean particle size measured by dynamic laser scattering yields a value of 50.7 nm for LSCF (Figure 5-6b).

5.3 Dispersions of Nanocomposites

In order to be able to prepare cathodes containing two components (composites) the addition of oxygen conductive particle to stabilized dispersions containing cathode particles (LSM etc.) is required. Therefore, a dispersion of commercially available Gadolinium stabilized ceria (GDC) nanoparticles was prepared and the surface potential behavior of GDC nanoparticles was studied. The result of the Zeta potential measurement of GDC nanoparticles dispersed in deionized water with the addition of organic dispersing agent exhibits the highest surface potential in basic as well as acidic environments, i.e. 38.4 mV at $pH=10.2$ and 36 mV at $2.7 \leq pH \leq 3.15$ (Figure 5-5). This enables co-stabilization of GDC particles in LSM dispersion as well as LSCF and LBSCF dispersions. In order to prepare the composite dispersions, the individually prepared LSM/LSCF/LBSCF and GDC dispersions were mixed together in appropriate ratios. According to the Zeta potential measurement and using the same dispersant, the low degree of agglomeration of both LSM and GDC particles should be retained. The particle size distributions of these dispersions measured at the same pH value exhibit maxima at 43 nm and 28 nm for LSM and GDC particles, respectively, confirming the conclusions from SEM micrographs of a rather low degree of agglomeration.

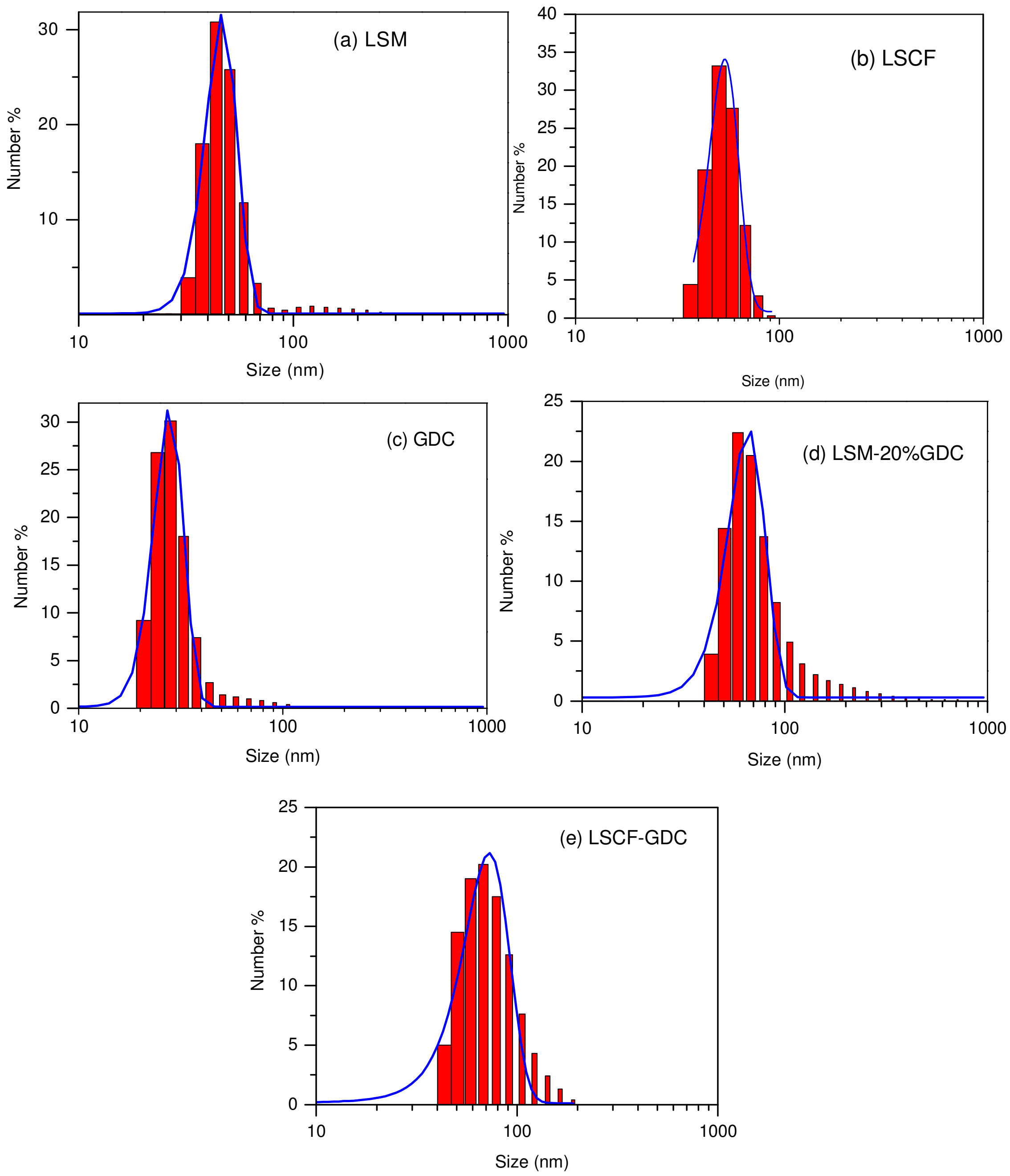

Figure 5-6: Particle size distributions of stabilized dispersions of a. LSM; b. LSCF, c. GDC; d. LSM-20%GDC and e. LSCF-20%GDC composite.

After dispersing the as prepared powders in de-ionized water and adjustment of the pH-value to the optimized value, the dispersions were treated ultrasonically. Particle size distributions of pure LSCF and GDC dispersions exhibit maxima at 50.7 nm and 29 nm, respectively. A nanocomposite dispersion of LSCF-20%wt.GDC shows an average particle size of 68 nm which is slightly higher than the pure LSCF dispersion (Figure 5-6e).

The determined mean particle sizes of the mixed dispersions are only slightly above the values of the individual dispersions. Narrow size distribution ensures the low degree of agglomeration and subsequently a uniform distribution of the GDC and cathode nanoparticles which in turn provides a three phase boundary (TPB) region, where the electronic conductor, the oxygen ion conductor and the gas phase are in contact with each other.

5.4 Nanoparticulate functional cathodes

The stabilized dispersions of the particulate cathode materials were spin coated directly on Yttria-stabilized Zirconia (YSZ). The HRSEM micrograph in Figure 5-7d shows the spin coated LSM layer with a thickness of about 500 nm after 10 hr of sintering at 850°C. From the micrograph (Figure 5-7d,e and f) it is evident that good contacts between the LSM nanoparticles and the YSZ substrate are achieved at this relatively low sintering temperature. The dispersion of GDC nanoparticles was coated directly on the YSZ substrate to serve as an interlayer for LSM and LSM-GDC composites and also as a buffer layer for LSCF and LBSCF cathodes. The complete layered structure on the YSZ-electrolyte substrate consisting of a pure GDC layer and a nanocomposite layer is shown in (Figure 5-8). The thickness of the LSM-GDC functional layer and the GDC interlayer averages 500 nm and 300 nm, respectively. The obtained microstructure of thin the cathodes in all three material systems was very similar. After spin coating of functional cathode films, LSM paste was screen printed to serve as current collector. The microstructure of LSM cathode obtained by screen printing of commercially provided LSM microparticles is shown in figure. The Cathode layer was sintered at 1150°C in order to obtain good contact with YSZ substrate (Figure 5-7a,b and c).

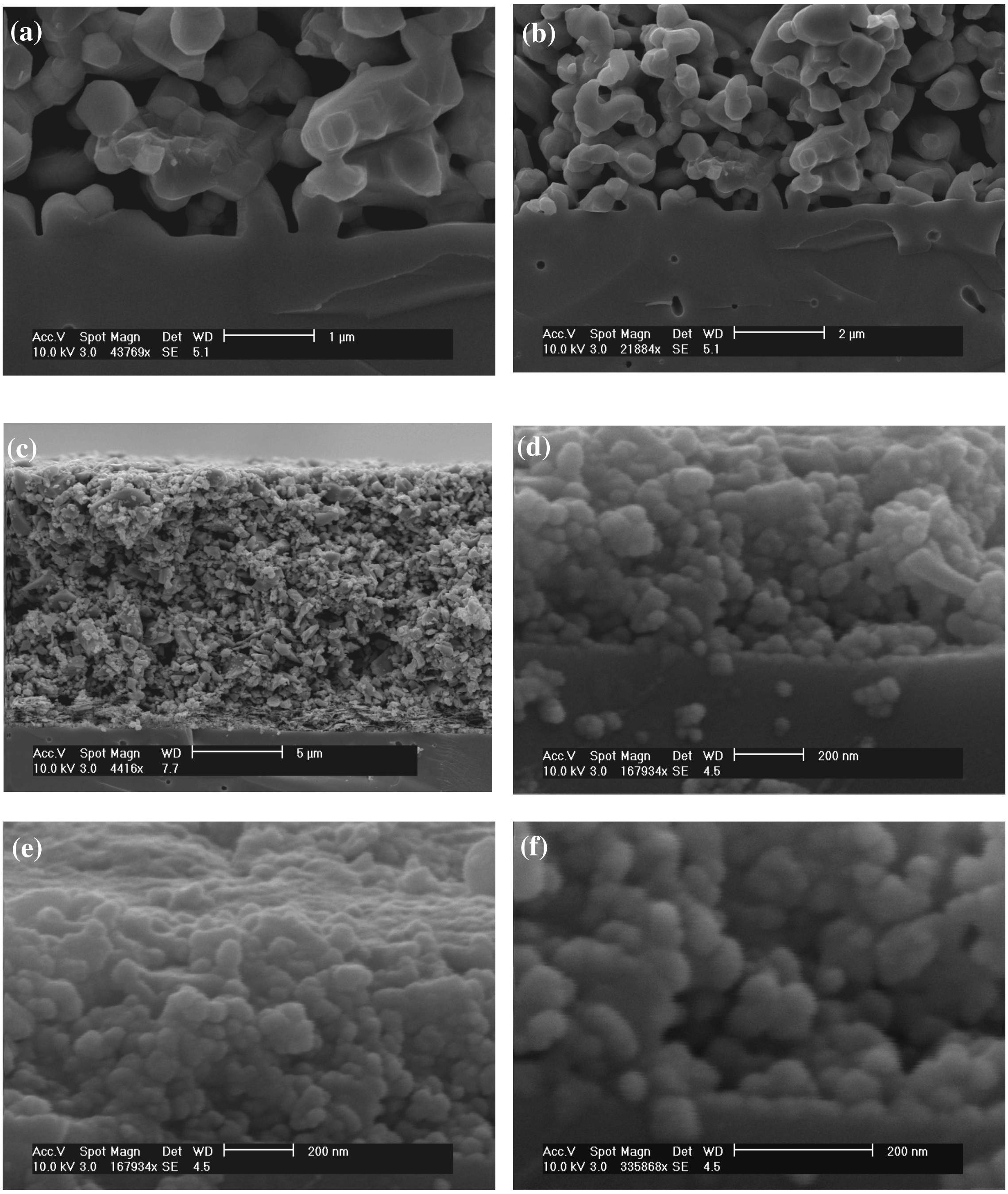

Figure 5-7 (a), (b) and (c) Commercial LSM micro powder screen printed on YSZ substrate and sintered at 1150°C, (d), (e) and (f) LSM nanoparticles synthesized by Spray Pyrolysis and deposited by spin coating on YSZ substrate and subsequently sintered at 850°C.

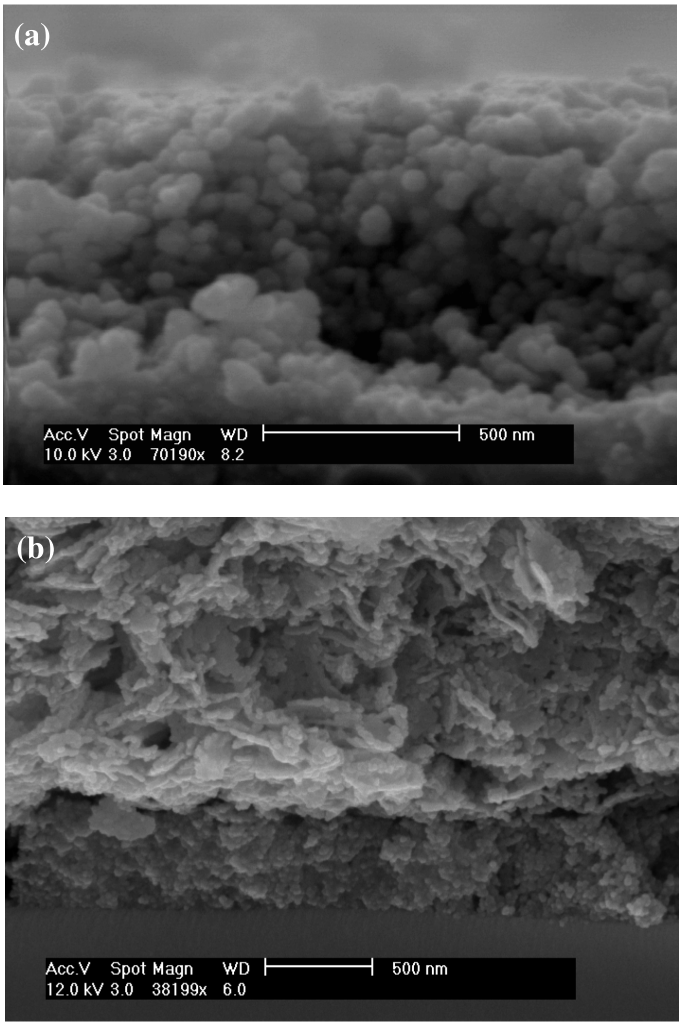

Figure 5-8 Nanocomposite functional cathode films deposited on a GDC buffer layer, (a) LSM-25%GDC nanocomposite deposited on GDC buffer layer, (b) LSCF-10%GDC deposited on GDC buffer layer.

5.5 Thermal Stability

Thermal stability of synthesized powder

The thermal stability of the nanostructures at working temperatures of the SOFCs is a key condition for long term stability and performance of the cell. Grain growth/sintering at elevated temperatures leads to a reduction of the specific surface area and the open porosity within the functional cathode layer. This in turns means lower electrochemical active zone and higher gas diffusion polarization. In other words, since electrochemical performance is correlated strongly with microstructure, by observing the sinter behavior of the cathode nanoparticles a qualitative estimation of electrochemical performance of cathode films can be made.

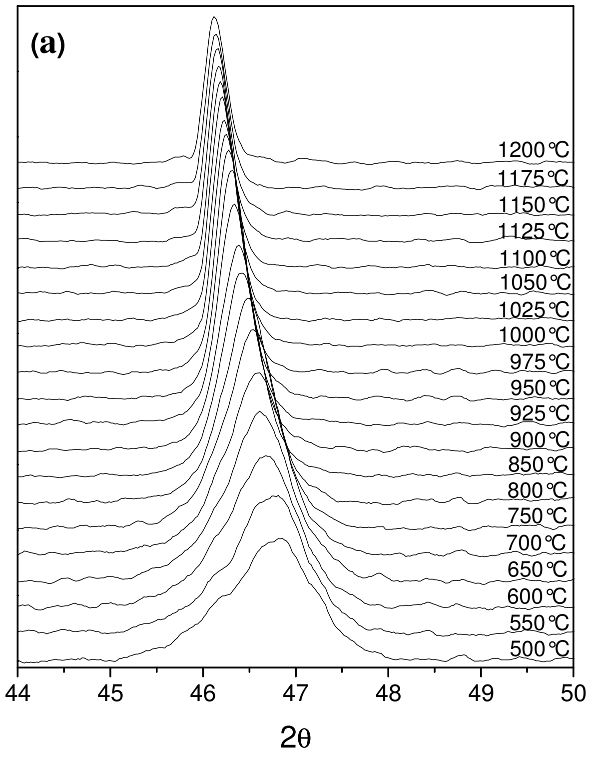

Figure 5-9 In-situ high temperature X-ray diffraction pattern of the (024) reflection measured in a limited angular range by means of a position sensitive detector.

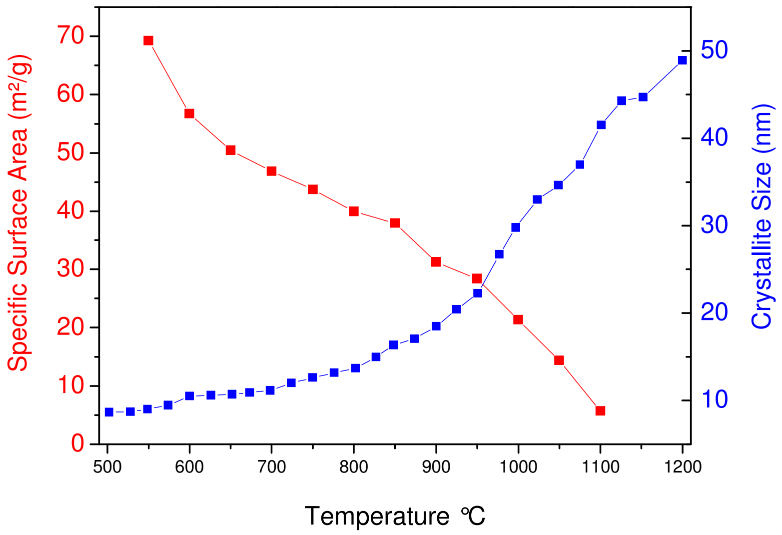

Figure 5-10: The parameters grain/ crystallite size and specific surface area, as indication for the stability, measured for LSM powders under continuous heating rate of 5 °C/min.

Furthermore, a highest working temperature regarding to grain growth for individual material systems can be suggested. Therefore, thermal stability of the as synthesized powders was studied by in-situ high temperature X-ray diffraction and ex-situ nitrogen adsorption measurements. For high temperature XRD (HTXRD) measurements the same machine was equipped with a high temperature chamber and a position sensitive detector in conjunction with a Ni-filter for the simultaneous recording of a 2θ range of 11°. Each XRD pattern was measured within 60 s while ramping the sample temperature with a constant heating rate of 5 K/min in ambient atmosphere. Figure 5-9 represents in-situ high temperature X-ray diffractograms of LSM synthesized at 1200 °C focused on the single reflex (024) at approx. 46-47°. The crystallite size has been calculated using the Scherrer equation, i.e. $D = K\lambda/(\beta\cos\theta)$, where D is the average crystallite size in nm, K is the Scherrer constant assumed to be 1, λ is the wavelength of the X-ray radiation in nm, θ is the Bragg angle, and β is the full width at half maximum (FWHM) in radians of 2θ. These parameters were obtained by fitting the (024) reflection of the samples with a pseudo-Voigt function using the commercial software TOPAS 3.0 (Bruker AXS, Karlsruhe, Germany). Using this analysis, the instrumental contributions to the FWHM can be neglected since they are of only minor significance in the case of very broad peaks. However, crystallite sizes calculated in this way should be regarded as a lower limit. Figure 5-9 represents in-situ XRD for (024) reflection on the LSM powder. The calculated crystallite size and specific surface area are summarized in Figure 5-10.

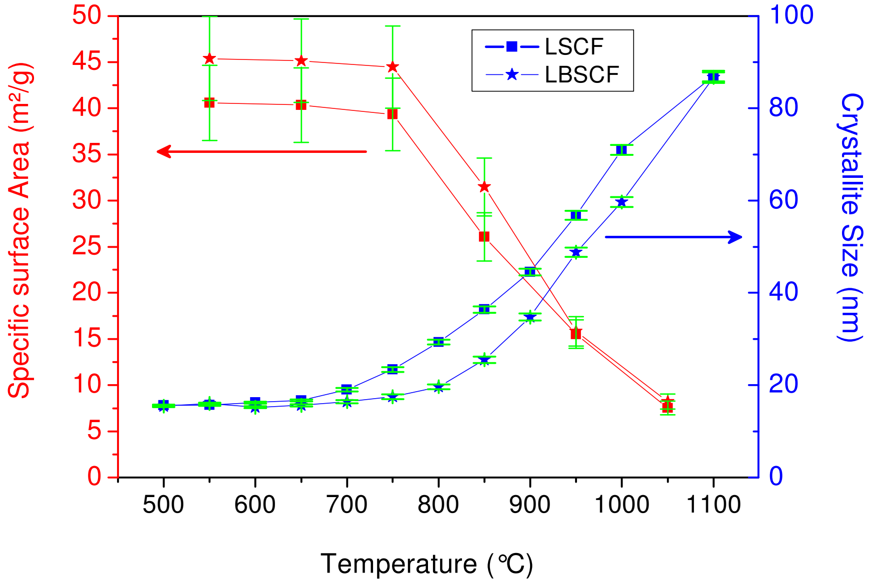

Figure 5-11: The parameters grain/ crystallite size and specific surface area, as indication for the stability, measured for LSCF and LBSCF powders under continuous heating rate of 5 °C/min.

The LSM nanoparticles exhibit to different grain growth rates, below and above 850 °C. The relatively slow rate of grain growth below 850 °C leads to 20 nm crystallites and a reduction in specific surface area. After 850 °C a faster sintering process is activated which is correlated with a considerable reduction of specific surface area and fast crystal growth. Therefore, in order to maintain nanocrystallinity and high specific surface area of LSM powder, the heat treatments should not exceed 850 °C. The results for LSCF and LBSCF powders are depicted in Figure 5-11. A similar behavior is observed for both materials. However, the accelerated grain growth begins at lower temperatures (750 °C). In case of LSM the results reveal that even at the highest working temperature of SOFCs (850 °C) the powder still retains its nanocrystalline nature, grain size below 20 nm, and a high specific surface area (approximately 40 m2/g).

Thermal stability in thin cathodes

The thermal stability and the grain growth of nanocomposite cathode were also studied by X-ray diffraction in the thin film cathodes. The results were analyzed by Rietveld methode and the grain size of cathode was calculated.

Figure 5-12 represents the grain growth of LSM nanocrystallites in thin film cathodes and compares those with the observed values of LSM powder in the as synthesized form. Below 800°C there was no significant difference observed which confirms the previous results related to LSM powder showing excellent thermal stability below 800°C. However, above 800 °C it is obvious that sintering processes in LSM cathodes films accelerate substantially faster than in the powder. At 850 °C, i.e. the typical working temperature of SOFC, LSM crystallites have reached approximately 30 nm, almost 100% larger than those in powder from (16 nm). This can be understood by considering the substantially higher density in the thin films. In hollow sphere morphology of the powder the sintering processes are basically limited in two dimensions, since, as discussed earlier, the thin shells of the hollow spheres are consisting of one of few layers of nanocrystallites. Therefore, sintering and grain growth is rather limited by the neighbor crystallites in a plane (two dimensional thin shell morphology). In despite of the hollow sphere morphology, sintering can occur in thin films in all three dimensions, i.e. over a much larger volume. LSM nanoparticles are packed quite dense in cathode films and each particle is in contact with surrounding particles in all three dimensions. In this three dimensional porous structure material transport processes for each particle is supported by several contact points. Thermal stability was also investigated in LSM –GDC composite cathodes with different weight percentage of GDC.

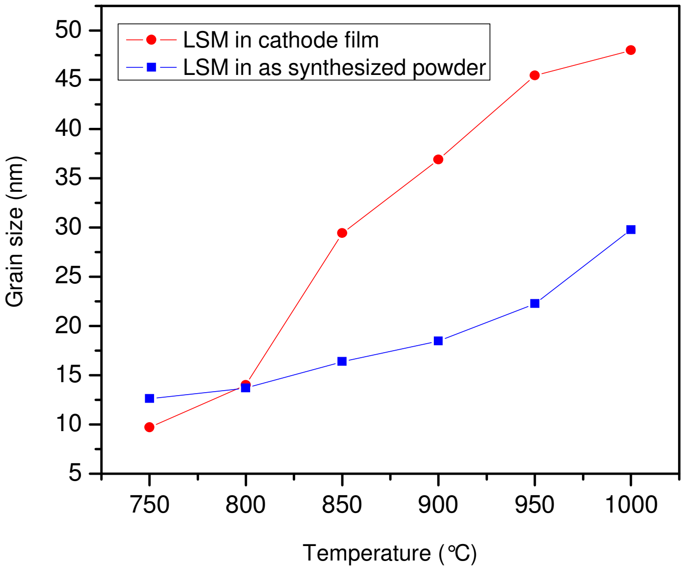

Figure 5-12: Comparison of grain growth of LSM nanocrystallites within hollow sphere structure and within LSM thin cathode layer.

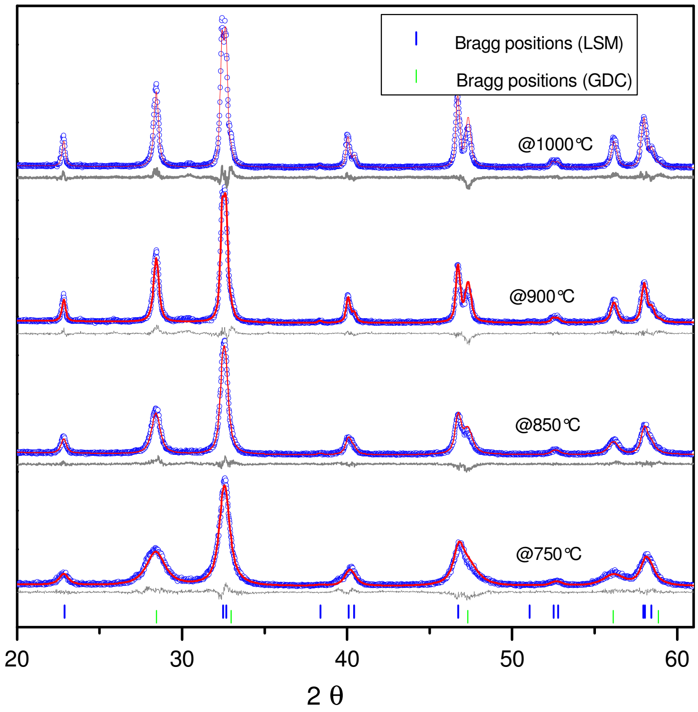

Figure 5-13: Rietveld refinement for high temperature X-ray diffraction obtained for LSM-30wt%GDC composite cathode.

Figure 5-13 shows the X-ray diffraction pattern of LSM-30%wt GDC nanocomposite after heat treatment at different temperatures. The grain sizes estimated from Rietveld refinement are shown in Figure 5-14. As observed earlier sintering processes in LSM nanoparticles are not significantly activated below 800°C. However, above 800°C a considerable reduction in grain growth rate is observed in case of composite film. At 850°C LSM particles within LSM-GDC composite cathode are approximately 18 nm while at the same temperature LSM particles in pure LSM cathode are 29 nm (Figure 5-14). Most likely, the introduction of GDC nanoparticles as a secondary phase serves as an inhibitor for grain growth. By decreasing the amount of the GDC phase the inhibition effect becomes less pronounced and below 20 wt% GDC there is no significant difference in grain growth is observed. GDC nanoparticles in starting material have smaller particle sizes and reveal a lower sintering rate in comparison to LSM through the temperature range up to 1000 °C. Due to the fact that in composite materials the crystallite growth inhibition effect is influenced by the dilution. Since the GDC particles are highly diluted in LSM, sintering which requires material transport between GDC-GDC particles is strongly limited. Additional evident arises from the fact that an inhibition effect in composite cathodes is observed, indicating a good dispersion and an uniform distribution of particles of both LSM and GDC phases within the cathode films. From the electrochemical point of view an uniform distribution of electronic and ionic conductive particles is of crucial importance. Better distribution of LSM and GDC particles provides higher three phase boundary areas, uniform distributed pathways for electron and oxygen ions which all in turns results in a higher electrochemical activity and subsequently, lower polarization resistance.

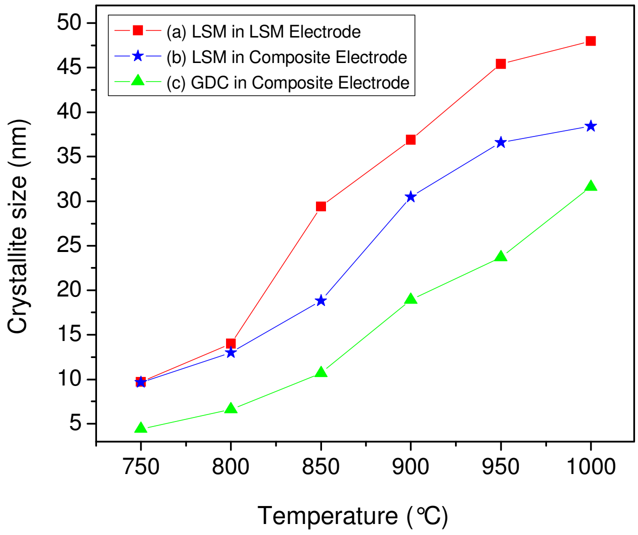

Figure 5-14: Comparison of grain growth of LSM nanocrystallites within LSM cathode and LSM-30wt% GDC cathode.

Chapter Six

6 Electrochemical characterization of thin film cathodes

The aim of this chapter is to focus on the achievement of the lowest cathode polarization resistance by compositional and morphological architecture. The electrochemical characterization of the nanocrystalline cathode material was performed in the thin film cathode form. In order to perform reliable measurements symmetrical half cells prepared by spin coating of dispersions containing cathode nanoparticles and subsequently characterized by high temperature impedance spectroscopy measurements. In this work, the electrode activity is determined in terms of the interfacial polarization resistance, which is measured by AC impedance spectroscopy. The interfacial polarization resistance is the difference between the high and low frequency intercepts on the real axis of the complex impedance plane. Since the purpose of the present study is to characterize the effect of microstructure (active surface area) on the interfacial polarization resistance of the same electrode material, the polarization behavior of the electrodes under different DC voltages were not studied [120]. The interfacial impedance response under open-circuit conditions represents the equilibrium properties of the interface and thus is related to the exchange current densities or catalytic properties of the interface. In this chapter, the effect of microstructure (active surface area) on the interfacial polarization resistance will be discussed within individual cathode material systems (LSM, LSCF and LBSCF).

6.1 $La_{0.75}Sr_{0.2}MnO_{3-\delta}$ cathodes

LSM Nanoparticulate cathode on YSZ

The high temperature impedance spectra measured for LSM nanoparticles deposited directly onto yttria stabilized zirconia substrates (symmetrical cells) are shown is Figure 6-1. For symmetrical cells, the measured impedance response reflects in principle the sum of two nominally identical electrodes. Therefore, in the figures presented in the following, the electrode response is divided by two. This means also that the polarization resistance determined from the plots is the average of the two electrodes being investigated. The impedance results in the complex plane, Nyquist/Cole-Cole plots (Z', Z'') are presented also in Figure 6-1, The results are shown also in Bode plots to provide a detailed information on the .validation of the absolute impedance , $|Z|$, and the phase shift, φ, as a function of the frequency of the sinusoidal signal.

Basically, the impedance spectra are composed of several components; a high frequency induction tail ascribed to the measurements lead, an ohmic resistance (the high frequency intercept adjusted for induction) mainly originating from the electrolyte, and usually two to four processes which contribute to the electrode impedance. A whole variety of chemical or physical processes contribute the overall impedance spectrum. The induction effect from the cables observed at higher frequency can become rather considerable in samples with lower ohmic resistance or at higher temperatures.

As illustrated in Figure 6-1 the impedance spectra of LSM nanoparticles in contact with the YSZ electrolyte appears as quite simple one dominant arc. The observation of a single semi-circle impedance spectrum for cells containing LSM microparticles in contact with YSZ substrate has been well documented in the literature [121-123]. In the equivalent circuit (Figure 6-1b) R1 represents the ohmic resistance of the LSM cathode, electrolyte and negligible resistance of the platinum wires, R2 and CPE2 are the interfacial resistance and capacitance, respectively [124-126]. The relations of the resistances values R1 and R2 to LSM layer and interfacial oxide layer have been given by Li and Xiao [127]. It should be noted that LSM is an electronic conductor and the interfacial oxide layer is a dielectric material. Consequently, the semicircle is assigned to the interfacial oxide layer. The partial contribution of a grain boundary impedance at lower temperatures (550 and 500°C) was not considered in the equivalent circuit and the fittings were carried out within the relevant frequencies for cathode polarization.

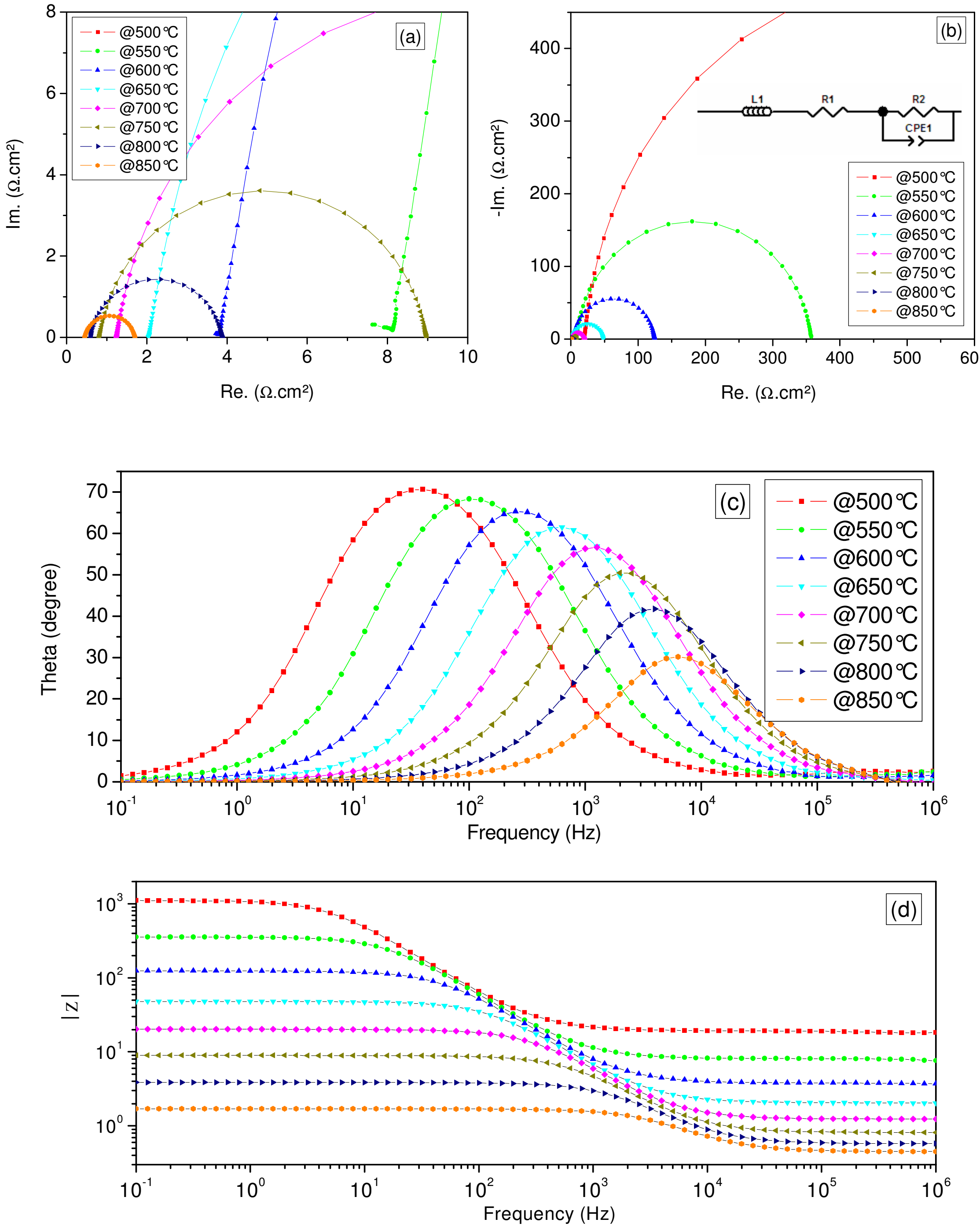

Figure 6-1: High temperature impedance spectra (nyquist, Cole-Cole and Bode plots) obtained for cathodes consisting of LSM nanoparticles which were coated directly on YSZ substrate in air.

Phenomenologically, all resistance quantities show an Arrhenius-type behaviour in the relevant temperature range (500-850 °C), i.e. they are proportional to exp(E_A/kT), with E_a being the activation energy of the respective quantity.

$$\ln R_P = \ln \frac{1}{k_0} + \frac{E_a}{RT} \qquad 6.1$$

where R is the resistivity, A is a material constant containing the carrier concentration term, T is the absolute temperature, E_a is the activation energy for small polaron hopping, and k is the Boltzmann constant.

The activation energy (E_a) can be calculated from the slopes of the linear correlations. The Arrhenius plots for the different cathode compositions show a linear relationship between 1/T and Log (Rp). To check the reproducibility of the preparation, contacting and measurement process, three cells were prepared identically and the results were compared. The ASR of all three cells differed by ±5 %, thus this value was taken as the relative error between the samples.

The measured resistance values extracted from the impedance spectra should be normalized according to the sample geometry. The area specific resistance (ASR) of the cathode is defined its polarization resistance normalized by its area.

$$ASR = \frac{resis\tan ce\ of\ electrode}{2\ (symmetry)} \times area\ \ of\ \ electrode \qquad 6.2$$

Figure 6-2 illustrates the temperature dependence of the total polarization resistance (Arrhenius plot) for a LSM nanoparticulate cathode and, for comparison, a microcrystalline LSM cathode. Each set of data was fitted with the least square method and is included as solid lines. The corresponding activation energies (Ea) are 147 and 136 kJ/mol, for the micro- and nano-LSM, respectively. While the activation energy do not differs substantially, the overall values of the ASR are lower for the nano-LSM than the micro-LSM. The cathode interfacial resistance exhibits a strong dependence on temperature. As a consequence, the electrode-related resistances become more important as the temperature is decreased. Obviously, the application of LSM nanoparticles results in a considerable reduction of the cathode polarization over the entire temperature range of the measurement. In order to achieve proper adhesion between LSM and YSZ, electrolyte the samples were sintered prior to the measurement at high temperatures. Thin films of LSM nanoparticles deposited on the YSZ substrates were heat treated at 850°C for two hours and the cell of micro LSM was heat treated at 1150°C.

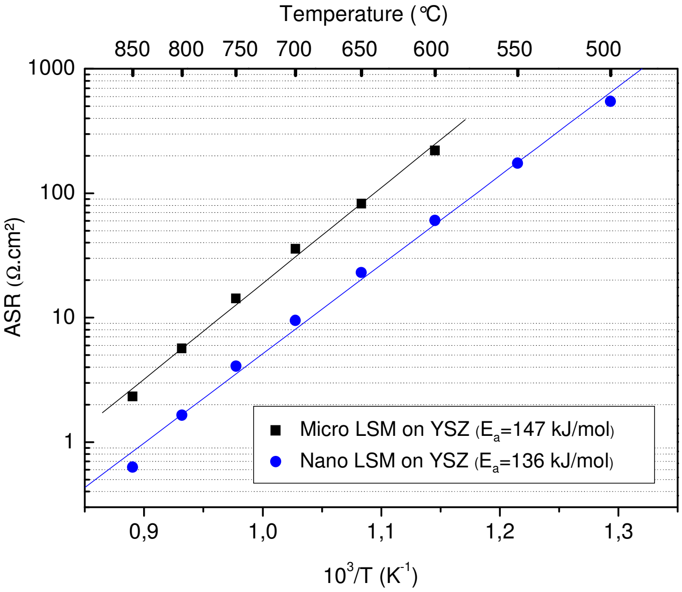

Figure 6-2: Arrhenius plot representing area specific resistances for nano and micro LSM cathodes coated on YSZ substrate. The nanoparticulate LSM cathode shows an ASR of 0.62 Ωcm^2 at 850 °C which is 3.75 times lower than the value for the finest commercial LSM powder sintered at 1150 C in this study.

The nanoparticulate LSM cathode shows an ASR of 0.62 Ωcm2 at 850°C which is 3.75 times lower than the value for the finest commercial LSM powder sintered at 1150 C in this study. The decrease of the ASR for LSM nanoparticles confirms the increase of TPB at the cathode/electrolyte interface. From the HRSEM, it is evident that even at the lowest sintering temperature (850 °C) good connection between LSM nanoparticles and the electrolyte have been (Figure 5-7). This is due to the fact that sintering processes are already activated at lower temperatures. In contrast, if the sintering temperature of the electrode is chosen too high, the interfacial resistance increases due to oversintering. As a consequence, loss of porosity and specific surface area as well as the formation of insulating secondary phases might occur. In the opposite case of the sintering temperature being too low, the bonding between the electrode and electrolyte could be rather poor, resulting in high interfacial resistances. For the commercially available powders the lowest sintering temperature is in the range of 1100 to 1150°C, which leads to lower specific surface area (electrochemical active zone) and increases the risk of interdiffusion metal ions and formation of electrochemical isolating interfaces. Nanopowders have the advantage that sintering processes are activated at considerably lower temperatures and thus retain a high specific surface that corresponds to a high density of TPBs.

LSM Cathode deposited on GDC interlayer

In order to further investigate the effect of morphology at the cathode/ electrolyte interface on the electrochemical activity, a nanocrystalline thin interlayer of gadolinium doped ceria was deposited on the YSZ substrate and heat treated up to 950°C for achieving proper adhesion to the electrolyte substrate. Subsequently, the LSM nanoparticulate thin layer was applied as described above on the GDC buffer layer and sintered at 850°C. Figure 6-3 illustrates the Nyquist plots of high temperature impedance spectra obtained from LSM cathode applied on GDC interlayer. The semi-circles corresponding to the cathode polarization are reduced in comparison to LSM cathode deposited directly on the YSZ substrate. The model used for the fitting of the impedance spectra consists of two phase constant phase element parallel with polarization resistances. The grain boundary contribution observed at lower temperatures was not considered in equivalent circuit and fittings were carried out within the relevant frequencies for cathode polarization. The values of the area specific resistance of cathode polarization are extracted from fitted data and depicted in Figure 6-4.

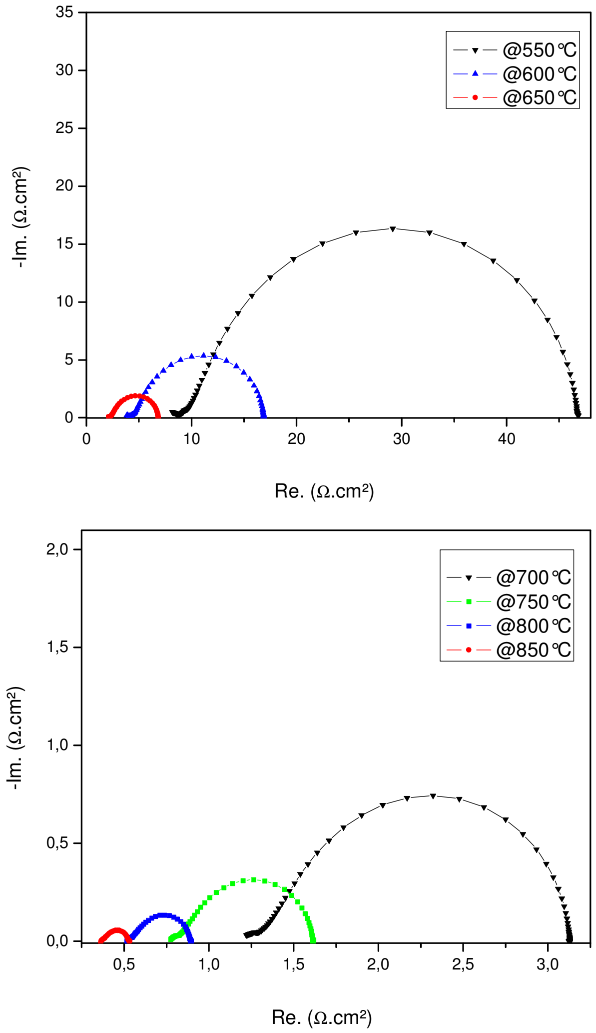

Figure 6-3: Impedance spectra (Nyquist plot) measured for cathode consisting LSM nanoparticles coated on GDC interlayer.

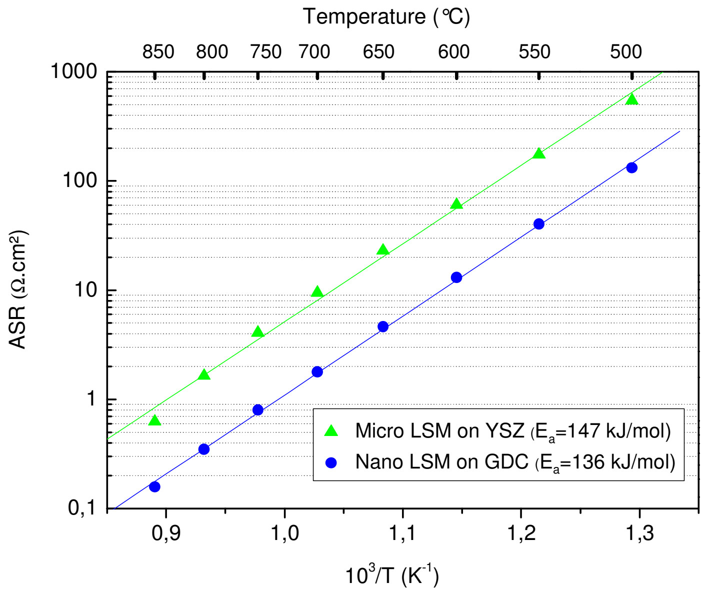

Figure 6-4: Arrhenius plot representing area specific resistances for cathodes consisting of LSM nanopartiels coated directly on YSZ substrate and coated on GDC interlayer.

Each set of data was fitted using the least square method. The results are included as solid lines and the corresponding activation energy (E_a) are estimated (Figure 6-4). Over the entire temperature range (550-850 °C) an improvement of the electrochemical activity by a factor of 4 (ASR=0.15 Ωcm^2) has been achieved by applying a thin film interlayer of GDC nanoparticles between the LSM functional layer and the YSZ substrate. The enhancing effect of nanoparticles on sinterability, higher contact area and better adhesion between cathode and GDC interlayer is clearly observed. Besides the effect of morphological improvements, GDC has also a higher electrochemical activity compared to YSZ. Furthermore, the activation energy for cathode polarization resistance is also reduced from 147 to 136 kJ/mol.

LSM-GDC composite cathodes

In the next step, nanoparticulate composite cathodes prepeared from composite dispersions were characterized electrochemically. Impedance spectra obtained for a symmetrical cell with the layer sequence of LSM-GDC/GDC/YSZ/GDC/LSM-GDC measured from 600-850 °C in air are shown in Figure 6-5. The impedance spectra of LSM-25wt%GDC composite system measured in air were fitted by the same electric equivalent circuit model applied for nano LSM cathode deposited on a GDC interlayer. The area specific resistance of the cathode polarization was extracted from fitting results for each composition (10-30 wt% GDC). Figure 6-6 summarizes the area specific resistances for different cathode compositions at various temperatures. Basically, the addition of 10wt% of GDC

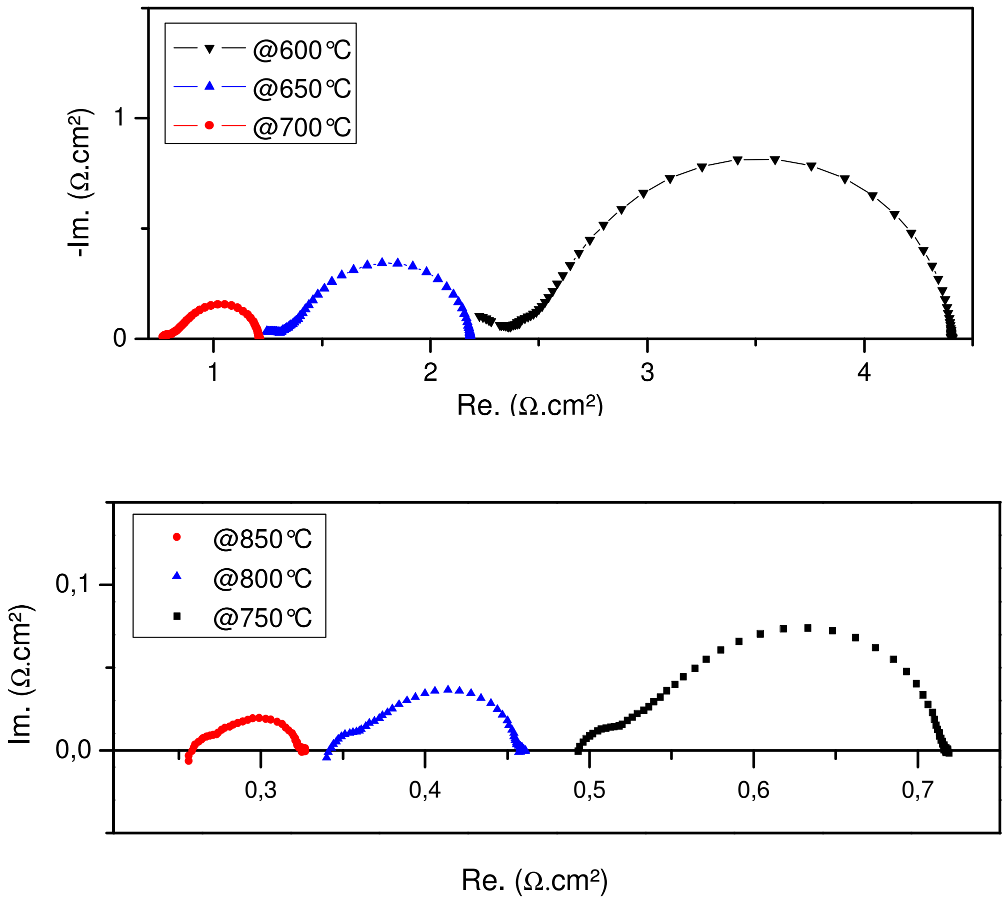

Figure 6-5: Impedance spectra (Nyquist plot) measured for LSM-25wt%GDC cathode under air atmosphere.

as an ionic conductive phase, into the LSM cathode reduces the cathode polarization resistance significantly. This trend is clearly observed over the entire temperature range under investigation (650-850°C). An addition of the content of ionic phase up to 20wt% reveals no significant change of the cathode polarization (Figure 6-6). The lowest ASR values were obtained for the LSM-25wt%GDC composition. However, higher amounts of GDC phase lead to higher cathode polarization. Significant enhancement of the electrochemical activity has been achieved by introducing GDC nanoparticles into the LSM nanostructure. The minimum ASR of 0.06 Ωcm2 at 850 °C has been achieved at a composition of LSM-25wt.%GDC compared to approx. 136 kJ/mol for nano LSM on GDC. Furthermore, the activation energy is reduced to 109 kJ/mol. The lower activation energy and polarization resistance of the nanocomposite LSM-25wt.%GDC cathode can be attributed to the excellent distribution of LSM and GDC nanoparticles, resulting in an effective extension of the TPB length.

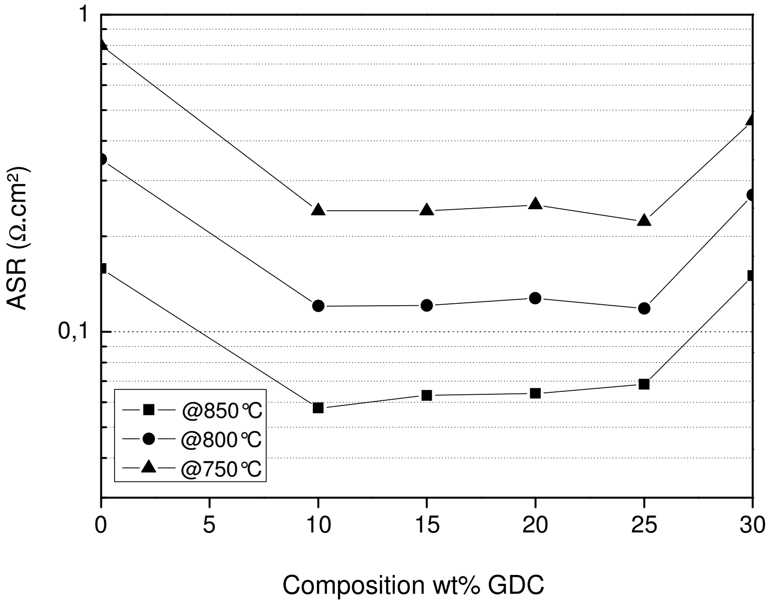

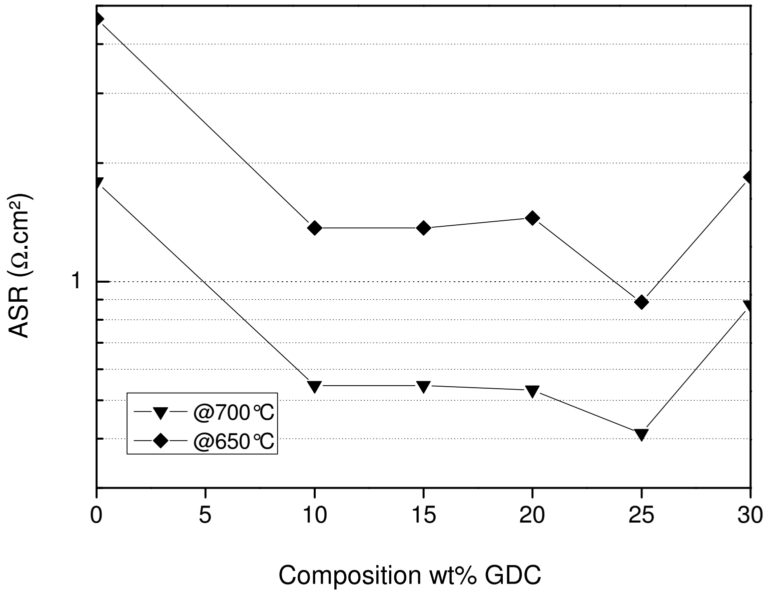

Figure 6-6: Area specific resistances for LSM-GDC cathodes versus composition ratio.

However, the interfacial polarization resistance does not decrease upon increasing the GDC content beyond 25 wt.%. The increase of the interfacial polarization resistance at higher GDC contents may be a consequence of the decrease of the electrical conductivity of the cathode as a result of loss of contact between LSM particles [84, 128]. Many authors have reported the optimal composition of composite cathodes at 40-50 wt.% of the ionic conductor component (i.e. GDC), for the case that both components of the composite cathode possess similar specific surface areas. Typically, the values of surface areas were in the range of 10 m²/g and below. In the present investigation, the specific surface area of both components is substantially larger. For LSM a specific surface area of 60-70 m²/g is achieved, for GDC a larger value of 100 m²/g was obtained. Thus, the ratio between specific surface area of GDC and LSM altered substantially. Most likely, this is the reason for the optimum polarization resistance value at lower GDC composition in the composite.

Figure 6-7 summarizes the Arrhenius-plots for different cathode materials. The comparison clearly shows the significant effects of the cathode morphology on electrochemical performance. The application of LSM nanoparticles reduces the cathode polarization at the cathode/electrolyte interface by increasing the electrochemical active points (three phase boundary).

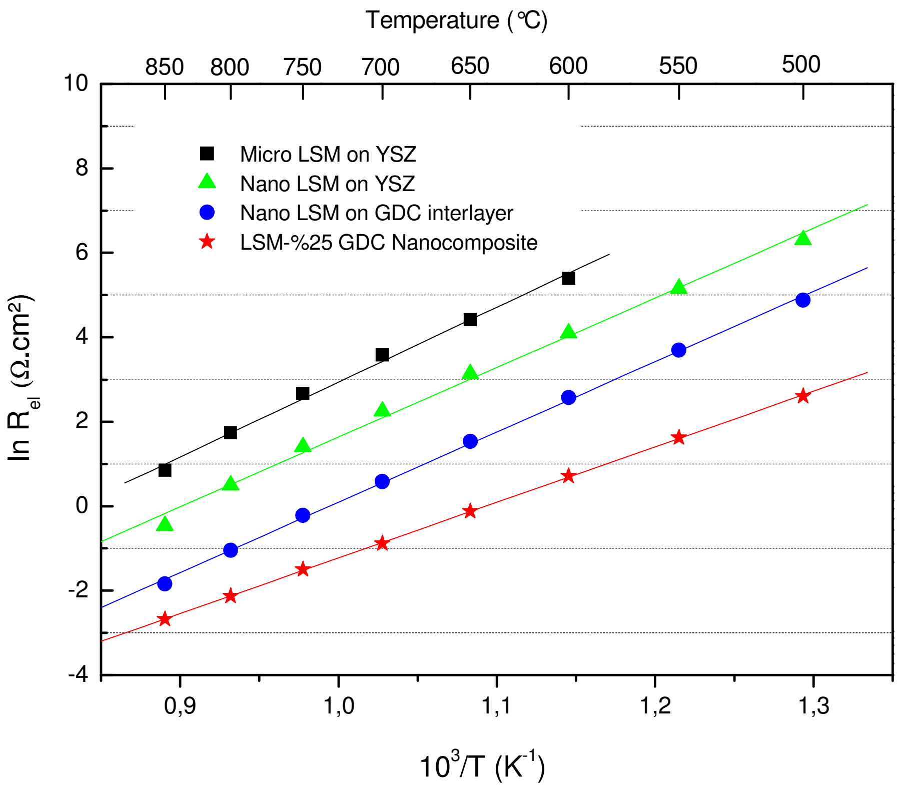

Figure 6-7: Arrhenius plots of cathode polarization resistances for LSM based thin cathodes.

Furthermore, the formation of appropriate contact points (necking) between LSM nanoparticles takes place at considerably lower temperatures since nanoparticles are highly active in sintering process at lower temperatures. This reduces the probability of strontium diffusion from the cathode into the electrolyte and, subsequently, formation of electronically insulating phases of strontium zirconates. The cathode/electrolyte interface can be further improved by the introduction of an interlayer with ionic conductivity which provides a high surface area and, subsequently, higher contact area with cathode particles. This was achieved by the deposition of a nanoparticulate gadolinium doped ceria thin interlayer prior to LSM functional cathode. The results indicate a considerable improvement of cathode polarization by a factor of four from nano-LSM deposited directly on the YSZ substrate. By introducing nanoparticles with ionic conductivity in the bulk of the functional cathode layer the electrochemically active zone (TPB) is extended from the cathode/electrolyte interface to the entire nanoporous cathode layers. Therefore, a further improvement by the factor of two was achieved.

6.2 Cathode polarization under oxygen pressure

In order to gain a better insight on the kinetics of the electrochemical processes governing on the cathode side, high temperature impedance measurements were carried out as a function of the partial pressure of oxygen $(P_{O_2} = 0.01 - 1\,atm)$. Figure 6-8 and Figure 6-9 show the impedance spectra of LSM-25%GDC at 850°C and 700°C obtained under various partial pressures of oxygen. Figure 6-8b represents also the results as a function of frequency. At oxygen partial pressures higher than 0.2 atm there are clearly two depressed arcs. Below 0.2 atm, a new arc appears at low frequencies, the resistance of which increases with decreasing oxygen partial pressure. These results were evaluated by using the equivalent circuit represented in Figure 6-8a which has been proposed by many authors for composite cathodes [18, 28, 29]. The high-frequency intercept of the impedance spectra is attributed to the Ohmic resistance of the electrolyte and lead wires (R_1 in the equivalent-circuit). In the equivalent-circuit, R-CPE1 and R-CPE2 circuits in series describe two rate limiting electrode processes at high and middle frequencies in series. R-CPE3 was considered only for the additional low frequency arc which appears at higher temperatures (above 800 °C) and lower partial pressure of oxygen ($P_{O_2} \leq 0.21$ atm). Based on the analysis of each arc, a model of the oxygen reduction reaction for the LSM–YSZ composite electrode is proposed in the following paragraphs.

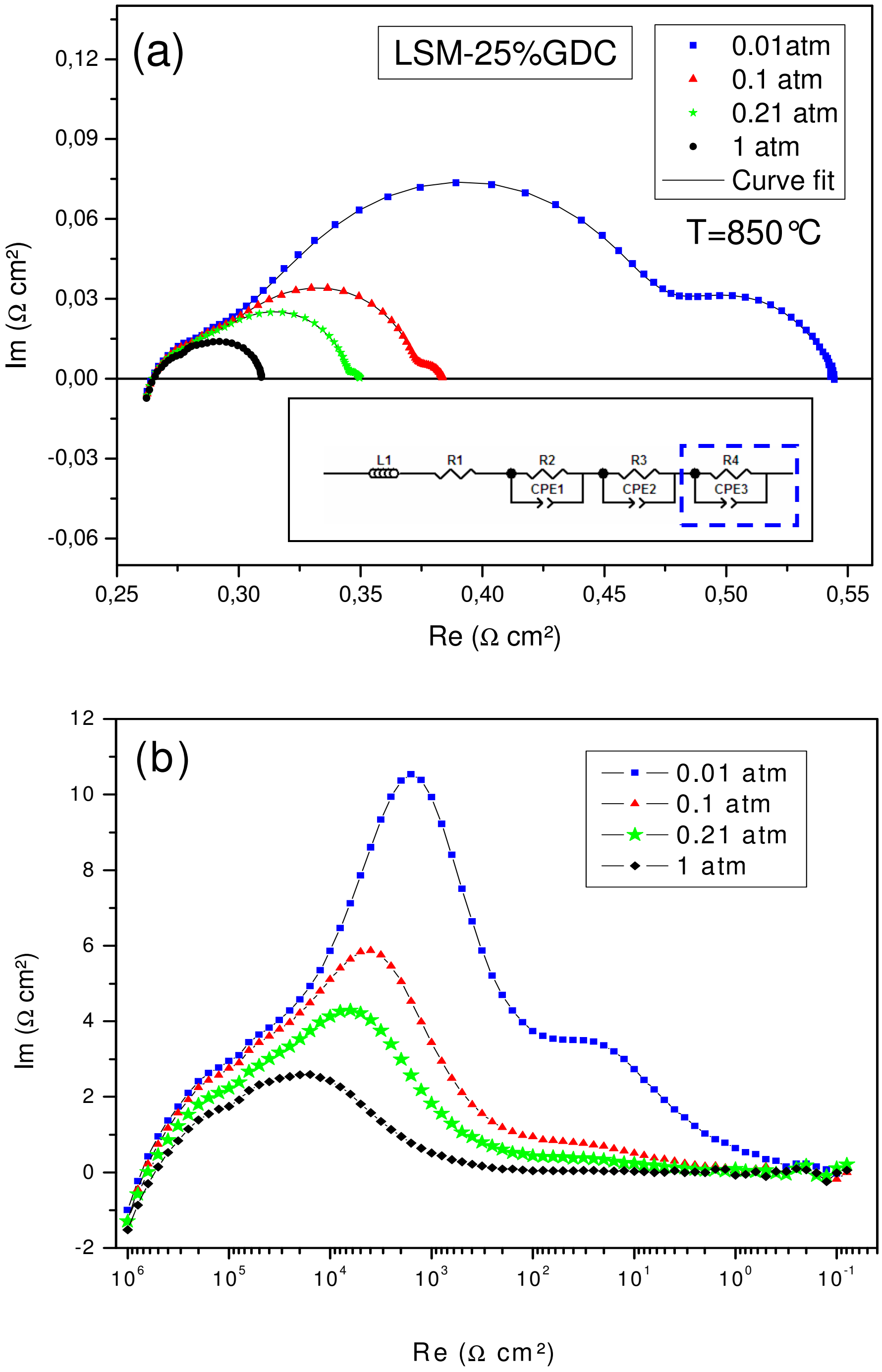

Figure 6-8: AC Impedance spectra at 850 °C for LSM-25%wt.GDC composite under different partial pressures of oxygen

High frequency arcs

The impedance spectra obtained for LSM-25wt%GDC are plotted versus oxygen pressure at 850 and 700 °C in Figure 6-8 and Figure 6-9. The high-frequency arcs did not vary with partial pressure of oxygen. At 850°C, the distinction between $(R_2 CPE_2)$ and $(R_3 CPE_3)$ arcs is difficult since the $(R_2 CPE_2)$ arc is small and is overlapped by the $(R_3 CPE_3)$ arc. At lower temperatures e.g. 700 °C the two arcs can be easily differentiated (Figure 6-9). The characteristics of the $(R_2 CPE_2)$ arc were inferred from the $1/R \propto p_{O_2}$ dependence. The weak p_{O_2} dependence of the $(R_2 CPE_2)$ arc suggests that neither atomic oxygen nor molecular oxygen is involved in the step [10]. Therefore, the $(R_2 CPE_2)$ arc can be interpreted as oxygen ion transfer from the TPB to the YSZ electrolyte or as grain boundary resistance in YSZ and GDC. On the other hand the capacitance of the YSZ grain boundary is known to be less than 10^{-8} F/cm^2 and the calculated capacitance of the $(R_2 CPE_2)$ arc is about 10^{-4} F/cm^2. Therefore, the semi-circular $(R_2 CPE_2)$ arc is most likely attributed to oxygen ion transfer. The reaction corresponding can be expressed as:

$$O^{2-} + V_O^{\cdot\cdot} \rightarrow O_O^x \qquad 6.3$$

where $V_O^{\cdot\cdot}$ represents an oxygen vacancy with two valences and O_O^x an oxygen ion at an oxygen ion site. [129].

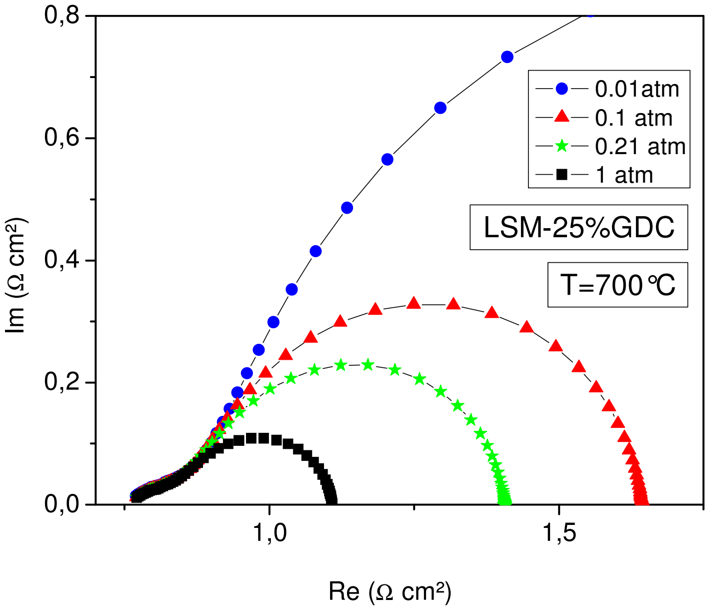

Figure 6-9: Nyquist plot for LSM-25wt%GDC cathode measured at 700°C under various partial pressure of oxygen from 1MHz to 0.01 Hz.

Intermediate frequency arcs

Various reactions, such as dissociative adsorption of oxygen molecules and surface diffusion, have been proposed to explain intermediate-frequency arcs. It has been suggested in the literature [129] that intermediate frequency arcs are related to the dissociative adsorption of oxygen molecule resulting a $p_{O_2}^{1/2}$ dependence. In this study, the oxygen reduction reaction on LSM–YSZ was investigated by modeling the p_{O_2} dependence. As clearly shown in Figure 6-10, the characteristics of intermediate-frequency arcs change with p_{O_2}. The $(R_3\ CPE_3)$ arc is approximately proportional to $p_{O_2}^{1/4}$. Based on the formula proposed by van Heuveln and Bouwmeester [4], the reaction model for oxygen reduction on LSM–YSZ composite is given as follows. Although various reaction models were applied, the model described below was most appropriate for the experimental results obtained in this study.

Model:

step 1. $O_{2(g)} \rightarrow 2O_{ad}$

step 2. $O_{ad} + e^- \rightarrow O_{ad}^-$

step 3. $O_{ad}^- \rightarrow O_{TPB}^-$

step 4. $O_{TPB}^- + e^- \rightarrow O_{TPB}^{2-}$

step 5. $O_{TPB}^{2-} + V_O^{\cdot\cdot} \rightarrow O_O^x$

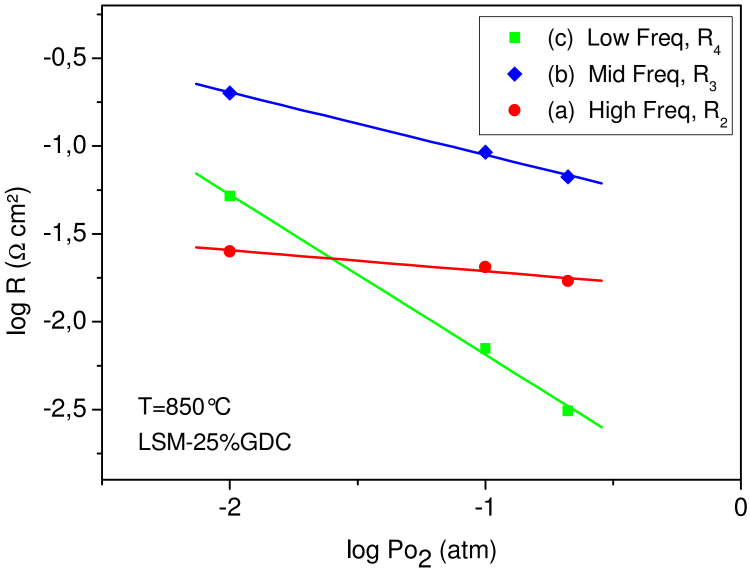

Figure 6-10: Dependence of the polarization resistance R on oxygen partial pressure for LSM-25%GDC electrode.

The rate equations corresponding to the proposed reaction model are expressed as:

$$r_1 = k_1 P_{O_2} - k_1^{'} a^2 O_{ad} \tag*{6.4}$$

$$r_2 = k_2 aO_{ad} \exp(-fE/2) - k_2^{'} aO_{ad}^{-} \exp(fE/2) \tag*{6.5}$$

$$r_3 = k_3 aO_{ad}^{-} - k_3^{'} aO_{TPB}^{-} \tag*{6.6}$$

$$r_4 = k_4 aO_{TPB}^{-} \exp(-fE/2) - k_4^{'} aO_{TPB}^{2-} \exp(fE/2) \tag*{6.7}$$

$$r_5 = k_5 aO_{TPB}^{-} - k_5^{'} \tag*{6.8}$$

Where k_i and k_i' are the rate constants for the forward and backward reactions, respectively. The activities of $V_O^{\cdot\cdot}$ and O_O^x in the electrolyte are assumed to be constant, *E* is the electrode potential, and *f*=*F*/*RT*, where R is the gas constant, T is absolute temperature, and F is the Faraday constant. TPB and *a* represent the length of the three-phase boundary and the activity, respectively. Equation (6.4) describes the diffusion of O^- species along the LSM surface to the TPB area, and Equation.(6.6) describes the transfer of O^{2-} species from the TPB to the electrolyte. If step 2 is assumed to be the rate-determining step, steps 1, 3, 4 and 5 are in virtual equilibrium. It then follows from Eq. (6.4). that:

$$aO_{ad} = (k_1 / k_1^{'})^{1/2} P_{O_2}^{1/2} \tag*{6.9}$$

From Equations. (6.5) and (6.6):

$$aO_{TPB}^{-} = (k_4^{'} / k_4)(k_5^{'} / k_5) \exp(fE) \tag*{6.10}$$

Substituting Equation (6.8) into Equation (6.4) gives:

$$aO_{ad}^{-} = (k_3^{'} / k_3)(k_k^{'} k_4)(k_5^{'} k_5) \exp(fE) \tag*{6.11}$$

Substituting Equations (6.7) and (6.9) into Eq. (6.4) gives the steady state reaction rate, which when converted to a current $(i = -nFr)$, gives:

$$i = i_{anodic} - i_{cathodic} \tag*{6.12}$$

$$i_{anodic} = nFk_2^{'} (k_3^{'} / k_3)(k_4^{'} / k_4)(k_5^{'} / k_5) \exp(3fE/2) \tag*{6.13}$$

$$i_{cathodic} = nFk_2 (k_3 / k_1^{'})^{1/2} P_{O_2}^{1/2} \exp(-fE/2) \tag*{6.14}$$

In equilibrium, the net current is zero, i.e. $i_{\text{anodic}} = i_{\text{cathodic}} = \text{i}_0$ (exchange current density), which yields the Nernst relation:

$$E_{eq} = const + (RT / 4F) \ln P_{O_2} \tag*{6.15}$$

Substituting the Nernst relation into either Equation (6.11) or Equation 6.(12) yields the dependence of i_0 on p_{O_2}:

$$i_{0.2} \propto P_{O_2}^{3/8} \qquad 6.16$$

We now consider step 3 as the rate-determining step. Assuming that steps 1, 2, 4 and 5 are in virtual equilibrium, substituting Eq. (6.7) into Eq. (6.3). gives:

$$aO_{ad}^{-} = (k_2 / k_2^{'})(k_1 / k_1^{'})^{1/2} P_{O_2}^{1/2} \exp(-fE) \qquad 6.17$$

Substituting Eq. (6.8) into Eq. (6.4) gives:

$$\begin{aligned} i_3 &= nFk_3^{'}(k_4^{'} / k_4)(k_5^{'} / k_5)\exp(fE) \\ &\quad - nFk_3(k_2 / k_2^{'})(k_1 / k_1^{'})^{1/2} P_{O_2}^{1/2} \exp(-fE) \end{aligned} \qquad 6.18$$

In the same way as shown previously, the relation between i_0 (step 3) and p_{O_2} can be derived as:

$$i_{0,3} \propto P_{O_2}^{1/4} \qquad 6.19$$

We then consider step 5 as the rate-determining step. Assuming that steps 1, 2, 3 and 4 are in virtual equilibrium aO_{TPB}^{2-} is written as:

$$\begin{aligned} aO_{TPB}^{2-} &= (k_4 / k_4^{'})(k_3 / k_3^{'})(k_2 / k_2^{'})(k_1 / k_1^{'})^{1/2} \\ &\qquad \times P_{O_2}^{1/2} \exp(-2fE) \end{aligned} \qquad 6.20$$

$$\begin{aligned} i_5 &= nFk_5^{'} - nFk_5(k_4 / k_4^{'})(k_3 / k_3^{'})(k_2 / k_2^{'}) \\ &\qquad \times \left(k_1 / k_1^{'}\right)^{1/2} P_{O_2}^{1/2} \exp(-2fE) \end{aligned} \qquad 6.21$$

The dependence of i_0 (step 3) on p_{O_2} is derived as:

$$i_{o,5} \propto P_{O_2}^{0} \qquad 6.22$$

Hence, step 5 is independent of p_{O_2}. In the proposed reaction model, oxygen ion transfer (step 5) is then independent of p_{O_2} and O^- surface diffusion (step3) can be modeled as a $p_{O_2}^{1/4}$ dependence. Although $p_{O_2}^{1/4}$ dependence is generally interpreted as a charge transfer reaction, these results indicate that $p_{O_2}^{1/4}$ dependence could be O^- surface diffusion. Therefore, it is concluded that high-frequency arcs $(R_2\ CPE_2)$ represent oxygen ion transfer from the TPB to the electrolyte, and intermediate-frequency arcs $(R_3\ CPE_3)$ .represent the diffusion of O^- species along the LSM surface to the TPB.

Low frequency arcs

As it is clear from Figure 6-8, the low-frequency arcs change significantly with partial pressure of oxygen. It is evident that the $(R_4\ CPE_4)$ arcs exhibit an approximate $p_{O_2}^{0.95}$ dependence. The low frequency arcs obtained for LSM-25%GDC at the temperatures of 800 and 850 °C and various oxygen pressures reveal comparatively a negligible temperature dependence (Figure 6-11). Therefore, the low frequency arcs are not thermally activated. This reaction could be interpreted as the diffusion of oxygen molecules in the pores of the electrode or the associative adsorption of oxygen molecules. It has been found that the adsorption of oxygen molecules on LSM occurs dissociatively.[130]. Therefore, the $(R_4\ CPE_4)$ low-frequency arcs are attributed to gas phase diffusion, the activation energy of which is very low, and the gas phase diffusion flux resulting from the gradient in the chemical potential of the gas is proportional to the gas pressure. Gas phase diffusion occurs as follows:

$O_2 \rightarrow O_2(LSM - pore1)$

$O_2(LSM - pore1) \rightarrow O_2(LSM - pore\ 2)$

The oxygen diffuses from bulk gas into LSM pores within the open LSM pore system.

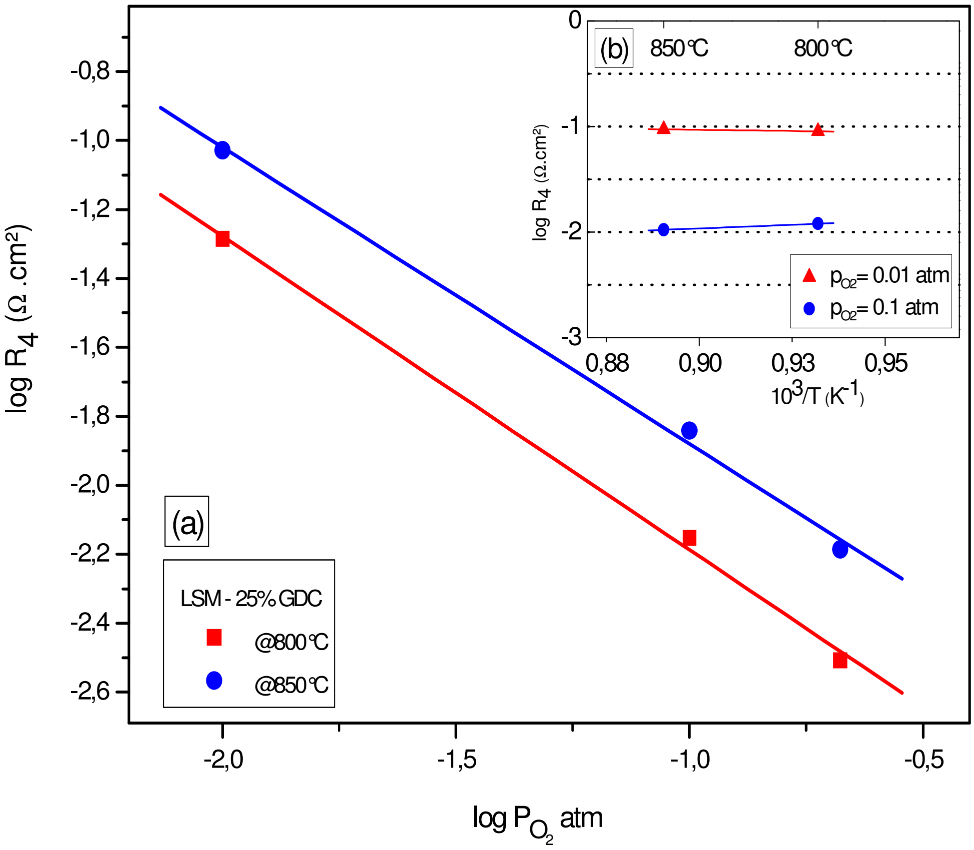

Figure 6-11: (a) Oxygen partial pressure and (b) temperature dependence of low frequency arc in LSM-wt%25GDC cathodes.

Mixed conductive cathodes

Nanoparticulate symmetrical cells of mixed conductive cathode materials (LSCF and LBSCF) were prepared by an analog procedure applied for LSM cathodes. Nanocomposite cathodes containing cathode particles with mixed and pure ionic conductive particles (10-30 wt%GDC) were characterized by high temperature impedance spectroscopy. Since the aim of this study focuses on the achievement of the lowest cathode polarization resistance by compositional and morphological architecture, in this part the discussions on impedance spectra obtained from the above material systems and their various composites will be limited to the cathode composition which represents the highest electrochemical activity among various compositions.

Impedance spectra obtained for a symmetrical cell with a layer sequence of LBSCF-10%GDC/GDC/YSZ/GDC/LBSCF-10%GDC measured at 350, 400 and 450 °C in air are shown in Figure 6-12. The contribution of bulk, grain boundary and cathode polarization is clearly observed within the impedance spectra at the low temperatures. As it is expected the first arc of the impedance spectra, characteristic of the bulk conductivity, does not alter when the oxygen partial pressure is changed. This confirms the extrinsic character of the ionic conductivity of the YSZ electrolyte. The capacitance values of 5.4 pFcm^{-1} and 75 µFcm^{-1} are calculated for the bulk and the grain boundary contributions at 350°C. These values are in good agreement with those reported in the literature [131, 132]. The activation values of 0.98 and 1.04 kJ/mol calculated for grain and grain boundary in temperature range of 350-450°C confirms the reported values for YSZ substrate in the literature. The cathode impedance contribution (polarization resistance) in Figure 6-12 corresponds to two cathode layers, as symmetrical cells were measured. At higher temperatures, the observation of the response of the bulk and the grain boundary of the electrolyte material (YSZ substrate and GDC thin film) became more incomplete due to a reduction of the time constants of the semicircles. The impedance spectra of the same sample measured at 450 and 650°C under various partial pressures of oxygen are shown in Figure 6-14. The equivalent circuit, proposed by many authors for mixed conductive cathodes [123, 124, 126], was used to fit the experimental data. In the equivalent circuit, L, C, CPE and R denote inductance (originating from cables), capacitance (C), constant phase element (CPE) and resistance, respectively.

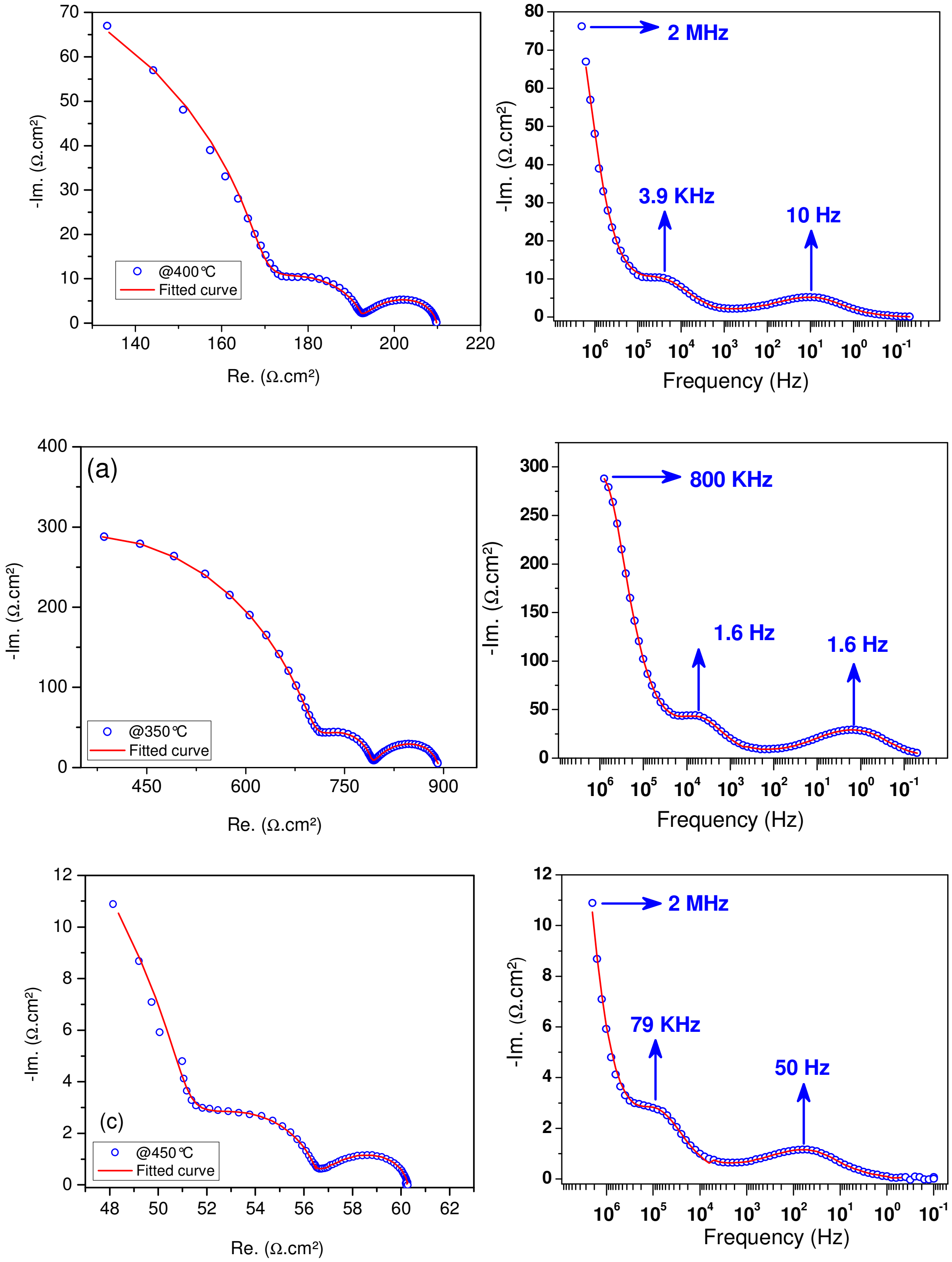

Figure 6-12 Impedance spectra of a symmetrical cell with functional cathode layers of LBSCF-10%GDC in air (a) at 350°C, (b) 400°C, (c) 450°C.

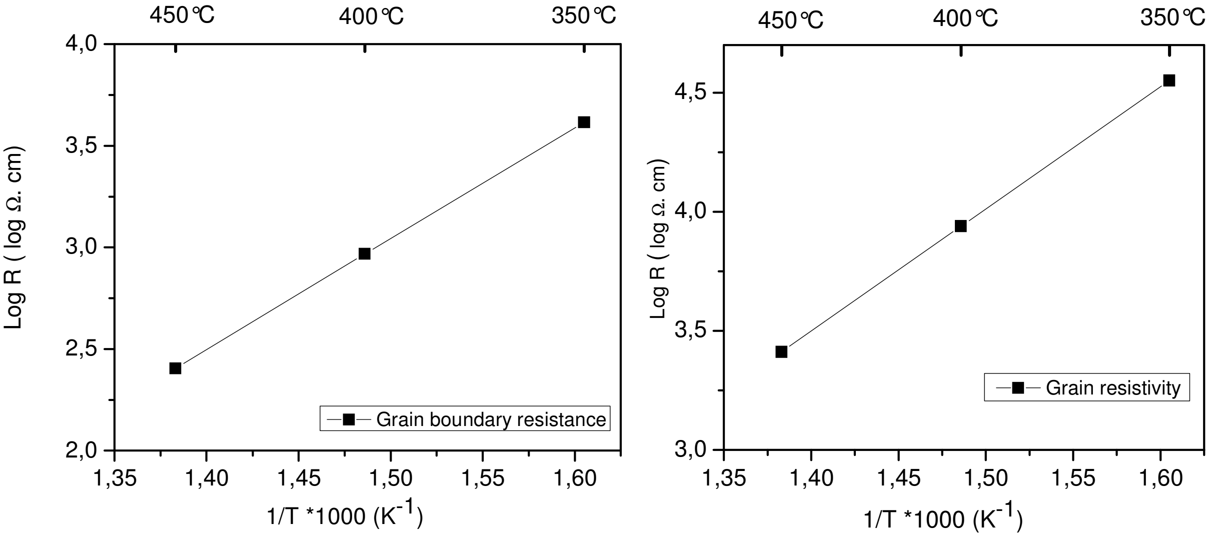

Figure 6-13: Grain and grain boundary resistances extracted from impedance spectra.

The high-frequency intercept of the impedance spectra is attributed to the ohmic resistance of the electrolyte and lead wires (R1 in the equivalent-circuit). In the equivalent-circuit, R2-C1 is considered for the grain boundary impedance (additional high frequency arc). R3-CPE1 and R4-CPE2 circuits in series describe two rate limiting electrode processes at high and middle frequencies in series. R5-CPE3 was considered only for the additional low frequency arc which appears at higher temperatures (above 600°C) and lower partial pressure of oxygen. The values for electrical elements estimated from the fits of the data of LBSCF-10%GDC at 650°C are listed in Table 6-1. The constant phase element (CPE) has the admittance $Y^* = Y_0(j\omega)^n$, where n is the frequency exponent and ω is the angular frequency. The arc summit frequencies are calculated using the formula $f^0 = 1/(2\pi(RY_0)^{1/n})$ and associated capacitances using the formula $C = 1/(2\pi R f^0)$ [133, 134]. R2-CPE1, considered for grain boundary impedance shows absolutely no dependence on oxygen partial pressure and the calculated activation energy of 1.07 eV (Figure 6-13) corresponds well with reported values [132]. The dependence of R5 on temperature and oxygen partial pressure obtained from fitted data is shown in Figure 6-15. The additional low frequency arc which appears at higher temperatures reveals an oxygen partial pressure dependence of (n ~ -0.95) while no temperature dependence was observed above 600°C. The capacitance associated with R5 possesses a very high value of 0.34, 0.61 and 0.99 Fcm^{-2} under oxygen partial pressure of 0.01, 0.05 and 0.1 atm at 650°C.

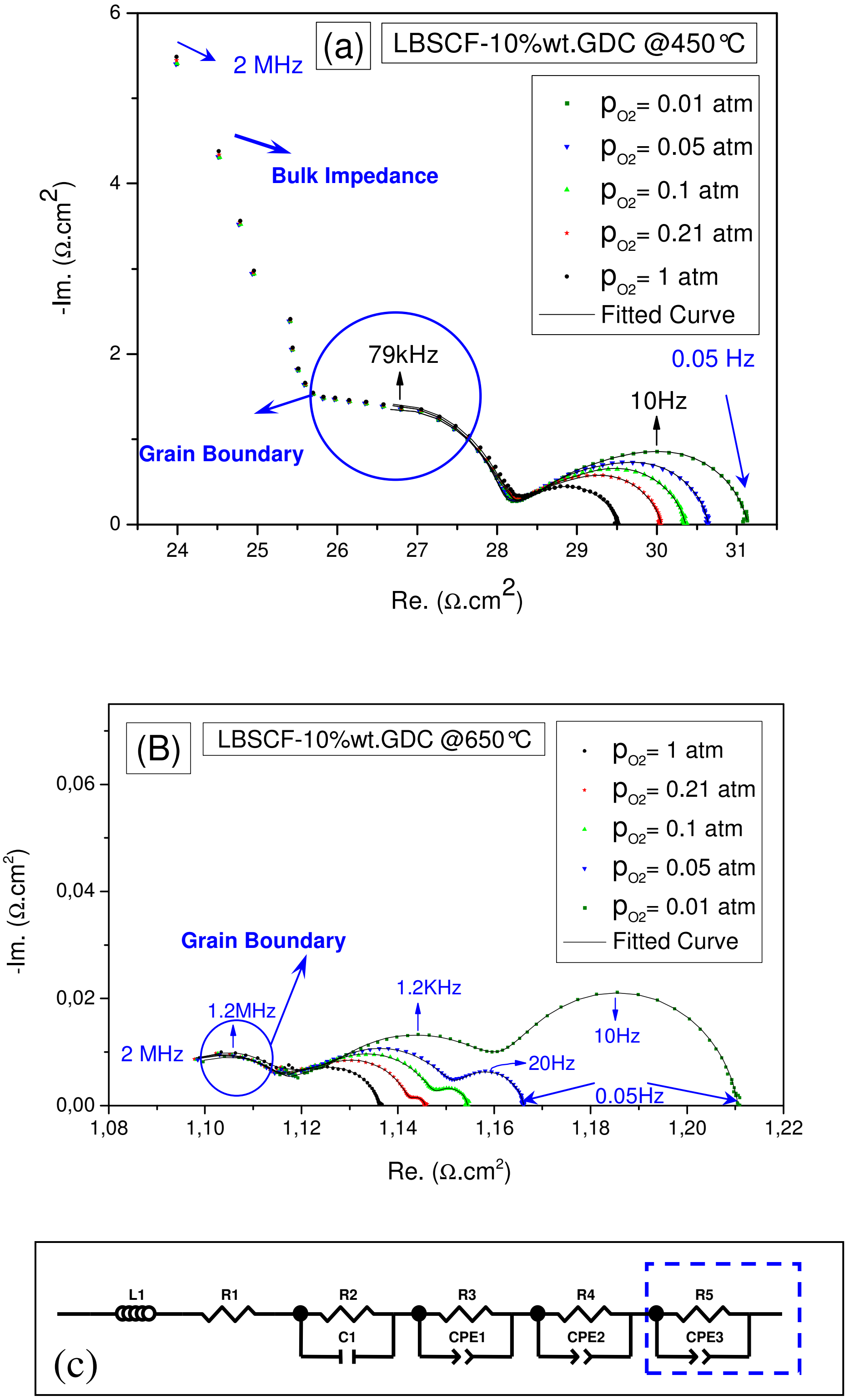

Figure 6-14 The dependence of ac impedance spectra of LBSCF-10%GDC on oxygen partial pressure (P_{O_2}) at different temperatures (a) at 450°C (b) at 650°C. Real axes corresponds the polarization resistance of half cell solely. (c) Equivalent circuit used for fitting Data

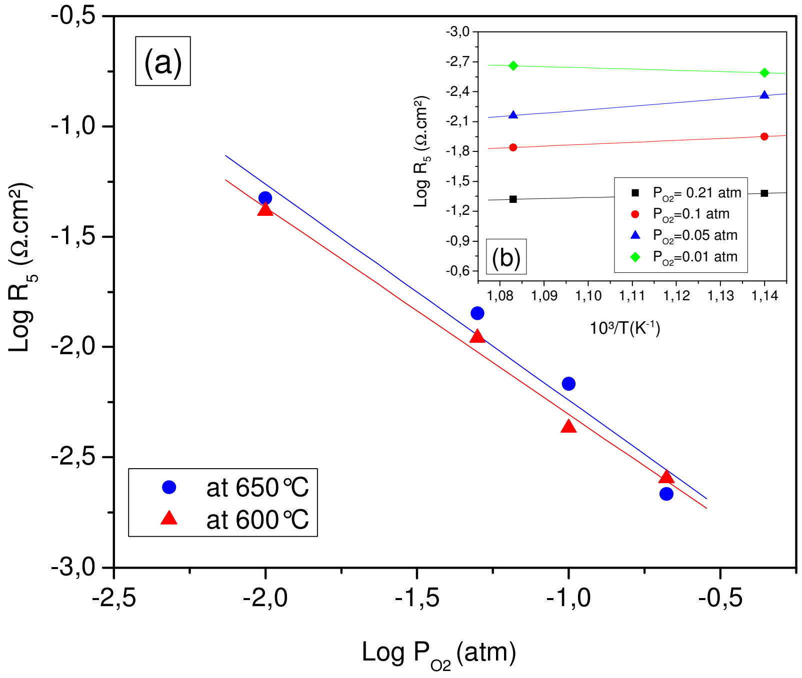

Figure 6-15 (a) Dependence of the polarization resistance R_5 on oxygen partial pressure for LBSCF-10%GDC cathode. (b) Dependence of the polarization resistance R_4 on temperature for LBSCF-10%GDCcathode

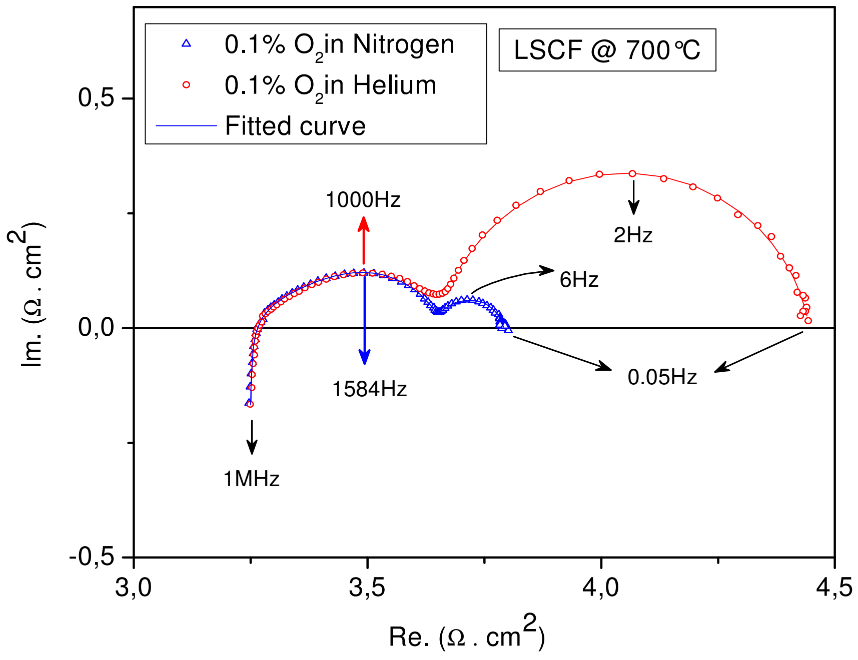

Figure 6-16 Impedance spectra observed for LSCF cathode under similar oxygen partial pressure diluted in Helium and Nitrogen.

These observations indicate that the additional low frequency arc can be interpreted as oxygen molecule (gaseous oxygen) diffusion within the cathode nanopores [81, 128, 135, 136] as well as the existence of a small stagnant gas layer outside the electrode [137]

The polarization associated with this arc is found to have a small activation energy, and the low frequency of the arc, which can generally be understood in terms of the relative chemical capacitances involved, as follows. The chemical capacitance associated with the faradaic impedance is proportional to the linearized storage capacity of adsorbed oxygen on the electrode surface within a distance of the interface.

A technique which has been used also in literature includes a variation of the total pressure while keeping oxygen partial pressure constant (since binary diffusion coefficients scale inversely with P_{total} at low pressure) or replacing the diluent gas (usually N_2 or Ar) with He [123, 138-140], since the binary diffusion coefficient for O_2 in He is about 4-5 times smaller than for O_2 in N_2. Figure 6-16 shows the impedance spectra observed for LSCF cathode under two mixed gases; N_2 –O_2 and He–O_2 at the same pressure (0.001 atm). The characteristics of gas phase diffusion were investigated by varying the gas balance (N_2–O_2, He–O_2). The oxygen partial pressure was 0.001 atm. The low frequency arc can be seen to change noticeably in N_2–O_2 and He–O_2; where the diameter of the arc is reduced significantly in He–O_2 since gas phase diffusion coefficient of He–O_2 is higher than that of N_2 –O_2 .The higher resistance in N_2 is accompanied by a proportional decrease in characteristic frequency rather than the appearance of a second feature in the impedance. The similarity of time scale for the chemical versus transport impedances in these cases reflects a large utilization length since the active region is already a significant fraction of the electrode bulk. Thus, any fluctuations in solid and gas composition resulting from gradients in gas concentration add little to the already large chemical capacitance.

The temperature dependence of the total area specific polarization resistance (ASR) for LSCF and LSCF-GDC composite cathodes is summarized in Figure 6-17. A good linearity of the cathode ASR versus reciprocal temperature was observed over the temperature range from 400 to 700°C. For the LSCF material system, the lowest ASR was obtained for the composition of LSCF and 10-15 wt% GDC. Area specific resistances of 65, 161 and 371 mΩ.cm² were observed at 700, 650 and 600°C, respectively. The addition of GDC nanoparticles to LSCF decreases the polarization resistance as well as the activation energy. The derived activation energy, 109-130 kJmol-1 for different LSCF cathodes is almost identical to that suggested for the oxygen surface exchange step (113±11 kJmol-1) [141]. The lower activation energy and polarization resistance of the nanocomposite LSCF-10 wt.% GDC cathode is attributed to the well-dispersed LSCF and GDC nanoparticles which effectively extend the TPB length and enhance the ionic conductivity. However, higher contents of GDC (above 20 wt%) lead to an increase in polarization resistance.

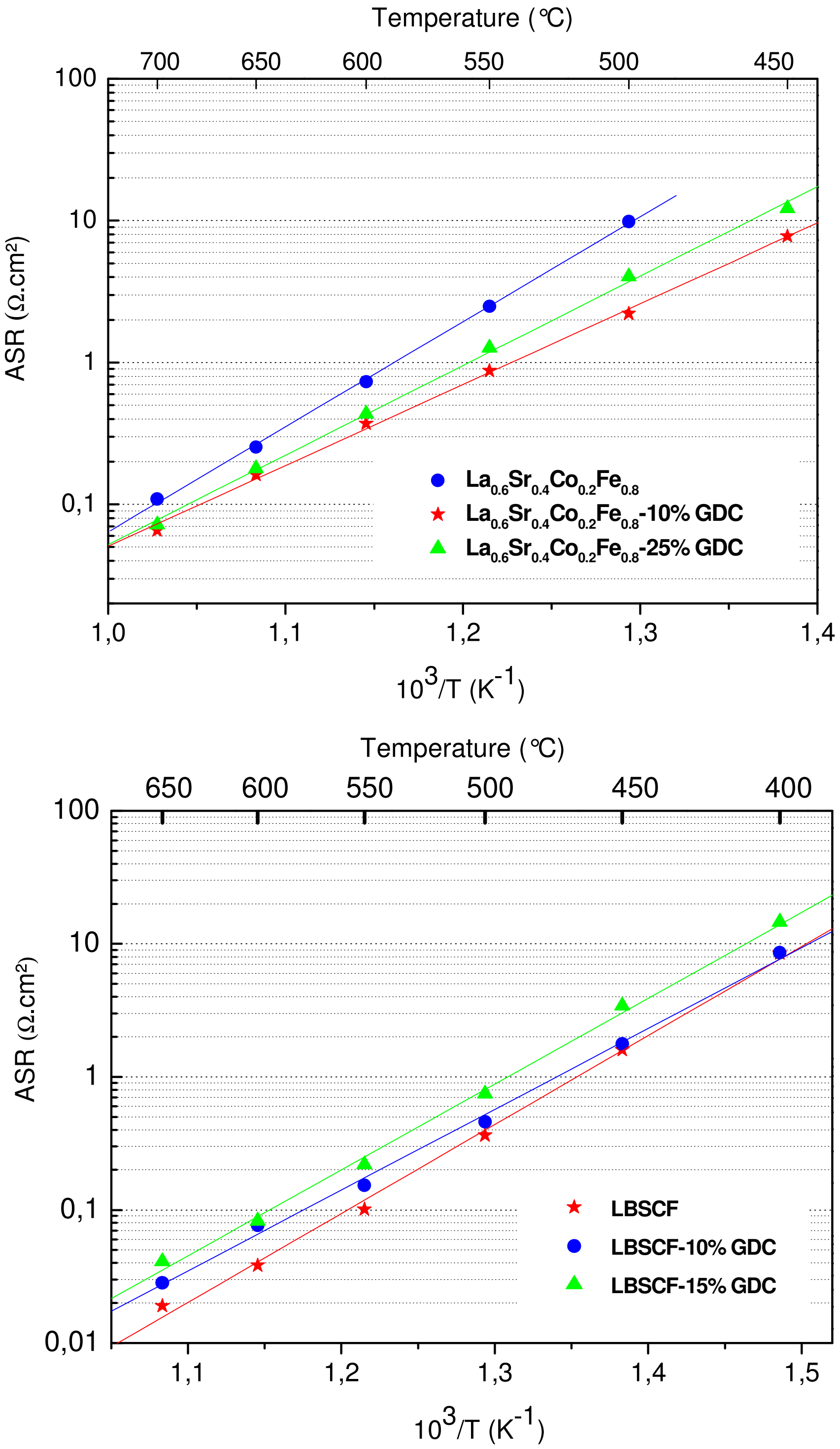

Figure 6-17: Area specific resistances obtained for mixed conductive (LSCF & LBSCF) cathodes.

This can be understood by the decrease of the electrical conductivity of the cathode as a result of loss of contact between LSCF particles. A change in activation energy from 1.55 eV (LSCF) to 1.27 eV (LSCF/CGO) composites with a dependence on the LSCF/CGO ratio has also been reported for thick film composite cathodes [84, 85]. The reason for this improved performance at lower temperature is given by the oxygen transport properties of LSCF and CGO. At high temperatures (800 °C), the oxygen self-diffusion coefficient of LSCF/CGO and CGO are the same [142] and close to the one of LSCF. However, the ionic conductivity of LSCF decreases strongly with decreasing temperature due to the high activation energy [84]. At lower temperatures (T<600 °C), the contribution of the ionic conductivity to the total conductivity of LSCF is low [142], thus an improvement of the cathode performance by the addition of CGO is related most likely to a higher diffusion coefficient of the composite material [142]. Furthermore, the oxygen surface exchange coefficient k of CGO is enhanced by two orders of magnitude in the presence of LSCF on the CGO surface [143, 144]. Consequently, faster oxygen transfer and consequently lower ASR are obtained when using composite cathodes.

The ASR values for the LBSCF thin cathodes are shown in Figure 6-17 Values of ASR of 19, 38, 101 and 363 mΩ.cm² are obtained at 650, 600, 550 and 500 °C, respectively. To our knowledge, values of the area specific resistance as low as the present data have not yet been reported for thin film (≤ 1 µm) cathodes. The low resistance reported by Shao was obtained with cathodes with thicknesses in the range from 10 to 20 µm, i.e. substantially larger than in the present experiments [145]. The lowest ASR values for LSCF and LBSCF porous thin film cathodes were reported so far by Beckel D. et al. [86]. The obtained ASR values were 0.6 and 0.3 Ω.cm² for LSCF and LBSCF cathodes at 650°C. Nevertheless, these values are still subsequently higher than this study.

The main reason for the improved performance originates from in the benefits of nanoparticles providing high specific surface area. In the case of the LBSCF cathode material, no further enhancement of the cathode performance could be achieved by the addition of GDC nanoparticles as it was the case for LSCF. Most likely this is due to the fact that the oxygen ion conductivity of the LBSCF material is higher than that of GDC [103, 142, 145, 146]. Hence, the introduction of a small amount of the electrolyte material decreases the cathode performance rather than increasing it. This indicates that the chosen composition, $La_{0.25}Ba_{0.25}Sr_{0.5}Co_{0.2}Fe_{0.8}O_{3-\delta}$, possesses the optimal ratio of electronic to ionic conductivity ratio.

The optimum sintering temperatures of 750 and 700 °C were found for LSCF and LBSCF cathodes, respectively. At lower sintering temperatures, the increased polarization resistance is indicative of a poor connection between the nanoparticles. At higher temperatures, the reduction of the specific surface area and porosity within the cathode layer are the most likely reasons for higher resistances.

Despite the low thickness of < 1 µm (which is less than 1/10 of that of conventional cathodes) of the nanocomposite cathodes prepared by this method, the ASR values are lower than values reported for the present ,cathode assemblies in the same composite system (LSCF and LBSCF - GDC) using conventional methods. Clearly, this indicates the high electrochemical activity of nanoparticulate cathodes and the high potential in applications in SOFC.

Table 6-1: Equivalent circuit parameters extracted from impedance data of LBSCF-10%GDC cathode at 650°C.

T=650°C	**R3 (Ω.cm²)**	**CPE3(Y_0), n3**	**C3 (F.cm²)**	f_3^0 **(Hz)**	**R4 (Ω.cm²)**	**CPE4, n4**	**C4 (F.cm²)**	f_4^0 **(Hz)**	**R5 (Ω.cm²)**	**CPE5, n5**	**C5 (F.cm²)**	f_5^0 **(Hz)**
0.01atm	0.006	0.005, 0.84	6.87E-4	38000	0.039	0.042, 0.7	0.0026	1519	0.047	0.545, 0.89	0.34	9
0.05atm	0.008	0.008, 0.78	5.25E-4	37900	0.026	0.02, 0.78	0.0023	2584	0.014	1.19, 0.86	0.61	18
0.1atm	0.01	0.012, 0.73	4.25E-4	37400	0.02	0.015, 0.81	0.0022	3558	0.006	1.93, 0.87	0.99	26

$Y^* = Y_0(j\omega)^n$, where j is the imaginary number, ω is the angular frequency and $0 \le n \le 1$.

Table 6-2: Activation energies estimated for various mixed conductive cathodes

Cathode	**Activation Energy**
LSCF	E_a=141 kJ/mol
LSCF -10%GDC	E_a=109 kJ/mol
LSCF -25%GDC	E_a=120 kJ/mol
LBSCF	E_a=128 kJ/mol
LBSCF -10%GDC	E_a=116 kJ/mol
LBSCF -15%GDC	E_a=124 kJ/mol

7 Summary

The thesis aimed at the investigation of the impact of variations of the morphological and compositional architectures on the enhancement of the electrochemical performance of different cathode materials for application in Solid Oxide Fuel Cells (SOFC). Nanocrystalline particles of cathode materials ($La_{0.75}Sr_{0.2}MnO_{3-\delta}$, $La_{0.6}Sr_{0.4}Co_{0.2}Fe_{0.8}O_{3-\delta}$ and $La_{0.25}Ba_{0.25}Sr_{0.5}Co_{0.2}Fe_{0.8}O_{3-\delta}$) with high phase purity and large specific surface area were synthesized via Nebulized Spray Pyrolysis method. The powders were characterized by various analytical methods, such as X-ray diffraction, electron microscopy, inductively coupled plasma and Nitrogen adsorption. The hollow sphere morphology of the as-prepared powder was modified into non-agglomerated nanoparticles by the application of ultrasonic energy. Stabilized dispersions of the cathode nanoparticles were prepared with the help of Zeta-potential measurements of the surface potential. Nanoporous thin films of the nanoparticulate cathode materials were prepared using spin-coating of the stabilized dispersions and subsequent annealing at elevated temperatures. Electrochemical characterization was performed in a half-cell geometry (symmetrical samples) using high-temperature impedance spectroscopy. The cathode performance was analyzed by the area normalized polarization resistance e.g. Area Specific Resistance (ASR).

$La_{0.75}Sr_{0.2}MnO_{3-\delta}$ (LSM) Cathodes

The progress achieved by using nanoparticles of the different cathode materials can be clearly seen in Figure 7-1 which summarizes the results for the LSM cathode architectures. The nanostructured LSM cathode in comparison to the conventional microstructured LSM cathode revealed a considerable reduction in polarization resistance by a factor of four at a temperature of 850 °C, resulting from the significant enlargement of the three phase boundary area, e.g. the electrochemically active area for the Oxygen reduction reaction. Furthermore, the introduction of a nanostructured gadolinium doped ceria (GDC) interlayer enhanced the cathode performance by an additional factor of four due to the continued improvement of the cathode/electrolyte interface. Further enhancement has been achieved by the addition of GDC nanoparticles into the cathode material, i.e. use of a LSM-GDC composite, which leads to a substantial extension of the electrochemically active zone from the cathode/electrolyte interface into the volume of the cathode. The lowest area specific resistance was obtained at the composition of LSM-25wt.% GDC. Further increase of the GDC fraction results in a continuous reduction of the cathode performance due to the effect of loosing contacts within thenetwork of electronically conducting particles.

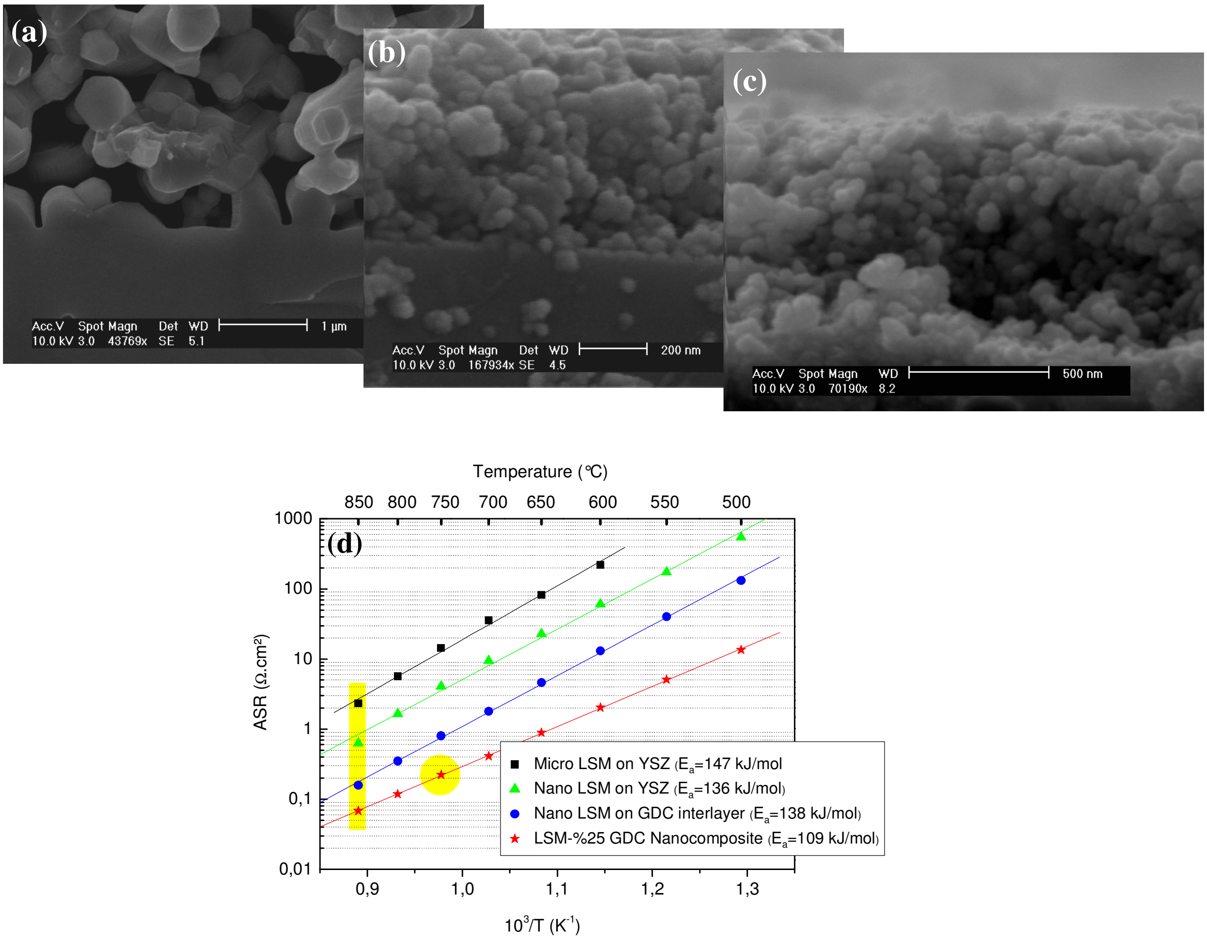

Figure 7-1: (a) cathode layer consisting of commercial micro-sized LSM particles (b) nanoparticulate thin film LSM cathode deposited directly on YSZ substrate (c) nanoparticulate thin film LSM cathode deposited on thin GDC interlayer (d) summary and comparison of cathode performance with various structural and compositional architecture.

As a result of the improvements of the cathode architecture, the typical working temperature of 850 °C for conventional LSM cathodes has been reduced to 750 °C by nanostructuring the cathode layer as well as the cathode/electrolyte interface.

$La_{0.6}Sr_{0.4}Co_{0.2}Fe_{0.8}O_{3-\delta}$ (LSCF) Cathodes

In the LSCF material system, the optimal cathode composition resulting in the lowest polarization resistance was obtained at 10 wt% GDC, with area specific resistances of 65, 161 and 371 mΩ.cm² obtained at 700, 650 and 600 °C, respectively. The addition of GDC nanoparticles to LSCF decreases the polarization resistance and the activation energies. The lower activation energy and polarization resistance of the nanocomposite LSCF-10 wt.% GDC cathode has been attributed to the high degree of dispersion of the LSCF and GDC nanoparticles. This results in a substantial extension of the TPB length and enhances the ionic conductivity. Using thin cathodes based on

LSCF material system a working temperature of below 600 °C was realized with ASR-values comparable to those obtained in state-of-the-art cathode materials at substantially higher temperatures.

$La_{0.25}Ba_{0.25}Sr_{0.5}Co_{0.2}Fe_{0.8}O_{3-\delta}$ (LBSCF) Cathodes

The addition of Barium to the perovskite structure increases substantially the ionic conductivity and as a result, pure LBSCF cathodes showed the highest electrochemical activity and very low values of the area specific resistances. Values of ASR of 19, 38, 101 and 363 mΩ.cm² were obtained at 650, 600, 550 and 500 °C, respectively. The addition of any amount of GDC to the LBSCF cathodes resulted in an increase of cathode polarization. Overall, a working temperature of 500 °C has been realized for a thin film system based on the LBSCF material system.

A new approach for the preparation of thin film functional cathode layers by spin coating of nanocomposite dispersions has been examined for mixed conductive cathode material systems. The cathodes prepared by this process achieved very high electrochemical activity, as a result of the precise control of the morphology and of the microstructure of the cathode layers by maximizing the surface area available for the oxygen exchange reaction. Very low cathode polarization resistance results in a reduction of SOFC working temperature to values below 500 °C. Therefore, several technical problems during the operation of SOFC's associated with ageing of seals, corrosion etc., during long term operation can be bypassed. Furthermore, the method offers a time saving and cost effective single step coating process compared to the conventional methods of fabrication of thin films, such as sputtering, pulsed laser deposition and metal organic chemical vapor deposition. Moreover, the thickness in the current structures (~1 µm) is at least 10–20 times smaller than that of cathode layers prepared by conventional methods. This represents not only a considerable reduction in ohmic resistance of the entire cell but also a significant reduction in material costs. Thus, the novel preparation technique for nanoparticulate thin cathode films provides an immense benefit for applications in Micro Solid Oxide Fuel Cells operating below 500°C.

8 Outlook

The new approach developed in the current study proposes a new method for fabrication of SOFCs, especially for miniaturized cells, so called Micro-SOFCs. In recent years, the ink-jet printing of nanodispersions has gained considerable interest in research and found enormous industrial applications. Thin films of organics (polymers) [147-149] for organic light emitting devices (OLED) and organic field-effect transistors (OFET), metal nanoparticles as contact electrodes for printed electronic devices [150-152] and metal oxides nanoparticles [153-155] for a wide range of applications from semiconductor electronics (transistors, solar cells etc.) up to gas sensors have been processed using ink-jet printing methods. Ink-jet printing has already been demonstrated as a method to deposit various ceramic layers [156-158] as well as three-dimensional structures [159, 160] and functionally-graded ceramic layers [161]. There are several attractive features to the ink-jet printing process suggesting a desirable fabrication method. Ink-jet systems have relatively fine resolution control and a precise deposition control. Ink-jet printing of stabilized dispersion containing cathode/ anode nanoparticles as well as metallic particles realizes a fully automatic single step micro-fabrication method. The films deposited by this approach are electrochemically highly active and require significantly lower sintering temperatures, which fulfill the requirements for fabrication of Micro-SOFCs based on free standing electrolytes.

9 References

1. Ryan O'Hayre, W.C., Suk-Won Cha, Fritz B. Prinz, *Fuel cell fundamentals* second ed. 2009.
2. Minh, N.Q., *Ceramic Fuel-Cells.* Journal of the American Ceramic Society, 1993. **76**(3): p. 563-588.
3. Minh, N.Q., *Solid oxide fuel cell technology-features and applications.* Solid State Ionics, 2004. **174**(1-4): p. 271-277.
4. Mogensen, M. and S. Skaarup, *Kinetic and geometric aspects of solid oxide fuel cell electrodes.* Solid State Ionics, 1996. **86-8**: p. 1151-1160.
5. Juhl, M., et al., *Performance/structure correlation for composite SOFC cathodes.* Journal of Power Sources, 1996. **61**(1-2): p. 173-181.
6. Serra, J.M., et al., *Nano-structuring of solid oxide fuel cells cathodes.* Topics in Catalysis, 2006. **40**(1-4): p. 123-131.
7. Jones, D.A., ed. *Principles and Prevention of Corrosion*. 1996, Prentice Hall, Upper Saddle River,

NJ.

8. Abdullah, M., et al., *Novel processing for softly agglomerated luminescent Y2O3\: Eu3+ nanoparticles using polymeric precursors.* Journal of the Ceramic Society of Japan, 2005. **113**(1313): p. 97-100.
9. [Anon], *SOFC development platform.* American Ceramic Society Bulletin, 2005. **84**(7): p. 8-8.
10. Aguiar, P., et al., *Oxide catalysts in indirect internal steam reforming of methane in SOFC.* Science and Technology in Catalysis 2002, 2003. **145**: p. 387-390.
11. W. Vielstich, A. and H.A.G. Lamm, eds. *Handbook of Fuel Cells: Fundamentals, Technology, and Applications*. 2003, Wiley.
12. Bassat, J.M., et al., *Oxygen isotopic exchange: A useful tool for characterizing oxygen conducting oxides.* Applied Catalysis a-General, 2005. **289**(1): p. 84-89.
13. M., G.V., *Die Gesetze der Krystallochemie.* Die Naturwissenschaften, 1926. **21**: p. 477-485.
14. Teraoka Y., N.T., Okamoto K., Miura N., Yamazoe N. , Solid State Ionics, 1991. **48**: p. 207-212.
15. Stevenson J. W., A.T.R., Carneim R. D., Pederson L. R., Weber W. J., *Electrochemical Properties of Mixed Conducting Perovskites La(1-X)M(X)Co(1-Y)Fe(Y)O(3-Delta) (M=sr,Ba,Ca).* Journal of the Electrochemical Society, 1996. **143**: p. 2722-2729.

16. Hammouche A., S.E.J.L., Henault M. , *Electrical and thermal properties of Sr-doped lanthanum manganites.* solid State Ionics, 1998. **28-30**: p. 1205-1207.

17. Bak T., N., J., Rekas M., Ringer S., Sorrell C. C., *Defect Chemistry and Electrical Properties of La(1-x)Sr(x)CoO(3-delta) II. Defect Diagrams.* Ionics. **7**(4-6): p. 370-379.

18. W., P.F., Solid State Ionics, 2000. **129**: p. 145-162

19. van Roosmalen J. A. M., C.E.H.P., J. Solid State Chem., 1994. **110**: p. 109-112.

20. Kuo J. H., A.H.U., Sparlin D. M., J. Solid State Chem., 1990. **87**: p. 55-63.

21. De Souza R. A., K.J.A., Solid State Ionics, 1998. **106**: p. 175-187.

22. Kamata H., Y.Y., Mizusaki J., Tagawa H., Naraya K., Sasamoto, J. Phys. Chem. Solids, 1995. **56**: p. 943-950.

23. Yasuda I., O.K., Hishinuma M., Kawada T., Dokiya M., Solid State Ionics, 1996. **86-88**: p. 1197-1201.

24. Endo A., F.H., Wen C., Yamada K. , Solid State Ionics, 2000. **135**: p. 353-358.

25. Hammouche A., S.E., Hammou A., Mat. Res. Bull., 1989. **24**: p. 367-380.

26. Singhal, S.C., *Advances in solid oxide fuel cell technology.* Solid State Ionics, 2000. **135**(1-4): p. 305-313.

27. Setoguchi T., I.T., Takebe H., Eguchi K., Morinaga K., Arai H., Solid State Ionics, 1990. **37**: p. 217-221.

28. H. Yokokawa, N.S., T. Kawada, and M. Dokiya,, edited by O. Yamamoto, M. Dokiya, H. Tagawa in Proc. of the Int. Symp. on Solid Oxide Fuel Cells (Tokyo, Japan), 1990: p. 118-134.

29. Akashi, T., et al., *Solid-state reaction kinetics of LaCrO3 from the oxides and determination of La3+ diffusion coefficient.* Journal of the Electrochemical Society, 1998. **145**(6): p. 2090-2094.

30. Mitterdorfer, A. and L.J. Gauckler, *La2Zr2O7 formation and oxygen reduction kinetics of the La0.85Sr0.15MnyO3, O-2(g)vertical bar YSZ system.* Solid State Ionics, 1998. **111**(3-4): p. 185-218.

31. J.-M. Bae, B.C.H.S., Solid State Ionics, 1998. **106**: p. 247-253.

32. Bae, B.C.H.S.a.J.-M., Solid State Ionics, 1998. **106**: p. 255-261.

33. Ralph, J.M., C. Rossignol, and R. Kumar, *Cathode materials for reduced-temperature SOFCs.* Journal of the Electrochemical Society, 2003. **150**(11): p. A1518-A1522.

34. Beckel, D., et al., *Thin films for micro solid oxide fuel cells.* Journal of Power Sources, 2007. **173**(1): p. 325-345.

35. Nikbin, D., Fuel Cell Rev., 2006: p. 21-24.

36. La, G.J., et al., *Microstructural. features of RF-sputtered SOFC anode and electrolyte materials.* Journal of Electroceramics, 2004. **13**(1-3): p. 691-695.

37. Wang, L.S., E.S. Thiele, and S.A. Barnett, *Sputter Deposition of Yttria-Stabilized Zirconia and Silver Cermet Electrodes for Sofc Applications.* Solid State Ionics, 1992. **52**(1-3): p. 261-267.

38. Gourba, E., et al., *Characterisation of thin films of ceria-based electrolytes for IntermediateTemperature - Solid oxide fuel cells (IT-SOFC).* Ionics, 2003. **9**(1-2): p. 15-20.

39. Gourba, E., et al., *Electrical properties of gadolinia-doped ceria thin films deposited by sputtering in view of SOFC application.* Journal of Solid State Electrochemistry, 2004. **8**(9): p. 633-637.

40. T. Tsai, S.A.B., *SPUTTER-DEPOSITION OF CERMET FUEL ELECTRODES FOR SOLID OXIDE FUEL-CELLS* J. Vac. Sci. Technol., 1995. **A** (13): p. 1073–1077.

41. Nagata, A. and H. Okayama, *Characterization of solid oxide fuel cell device having a three-layer film structure grown by RF magnetron sputtering.* Vacuum, 2002. **66**(3-4): p. 523-529.

42. Bieberle-Hutter, A.B. and H.L. Tuller, *Fabrication and structural characterization of interdigitated thin film La(1-x)SrcCoO(3)(LSCO) electrodes.* Journal of Electroceramics, 2006. **16**(2): p. 151-157.

43. Wang, L.S. and S.A. Barnett, *Sputter-Deposited Medium-Temperature Solid Oxide Fuel-Cells with Multilayer Electrolytes.* Solid State Ionics, 1993. **61**(4): p. 273-276.

44. Imanishi, N., et al., *Impedance spectroscopy of perovskite air electrodes for SOFC prepared by laser ablation method.* Solid State Ionics, 2004. **174**(1-4): p. 245-252.

45. Chen, X., et al., *Pulsed laser deposition of conducting porous La-Sr-Co-O films.* Thin Solid Films, 1999. **342**(1-2): p. 61-66.

46. Coccia, L.G., et al., *Pulsed laser deposition of novel materials for thin film solid oxide fuel cell applications: Ce0.9Gd0.1O1.95, La0.7Sr0.3CoOy and La0.7Sr0.3Co0.2Fe0.8Oy.* Applied Surface Science, 1996. **96-8**: p. 795-801.

47. Rupp, J.L.M. and L.J. Gauckler, *Microstructures and electrical conductivity of nanocrystalline ceria-based thin films.* Solid State Ionics, 2006. **177**(26-32): p. 2513-2518.

48. Manoravi, P., et al., *Laser ablation of La0.9Sr0.1Ga0.8Mg0.2O2.85 - Plume and film characterization.* Ionics, 2004. **10**(1-2): p. 32-38.

49. Chen, X., et al., *Thin-film heterostructure solid oxide fuel cells.* Applied Physics Letters, 2004. **84**(14): p. 2700-2702.

50. Will, J., et al., *Fabrication of thin electrolytes for second-generation solid oxide fuel cells.* Solid State Ionics, 2000. **131**(1-2): p. 79-96.

51. Garcia, G., et al., *Pulsed injection MOCVD of YSZ thin films onto dense and porous substrates.* Chemical Vapor Deposition, 2003. **9**(5): p. 279-284.

52. Seydel, J., et al., *Granular nanocrystalline zirconia electrolyte layers deposited on porous SOFC cathode substrates.* Materials Science and Engineering B-Advanced Functional Solid-State Materials, 2009. **164**(1): p. 60-64.
53. Liu, Y., et al., *Fabrication of Sm0.5Sr0.5CoO3-delta-Sm0.1Ce0.9O2-delta cathodes for solid oxide fuel cells using combustion CVD.* Solid State Ionics, 2004. **166**(3-4): p. 261-268.
54. Chen, C.H., E.M. Kelder, and J. Schoonman, *Effects of additives in electrospraying for materials preparation.* Journal of the European Ceramic Society, 1998. **18**(10): p. 1439-1443.
55. Taniguchi, I., R.C. van Landschoot, and J. Schoonman, *Fabrication of La1-xSrxCo1-yFeyO3 thin films by electrostatic spray deposition.* Solid State Ionics, 2003. **156**(1-2): p. 1-13.
56. Fu, C.Y., et al., *Electrostatic spray deposition of La0.8Sr0.2Co0.2Fe0.8O3 films.* Materials Chemistry and Physics, 2005. **91**(1): p. 28-35.
57. Princivalle, A., et al., *Porosity control of LSM/YSZ cathode coating deposited by electrospraying.* Chemistry of Materials, 2005. **17**(5): p. 1220-1227.
58. Princivalle, A. and E. Djurado, *Nanostructured LSM/YSZ composite cathodes for IT-SOFC: A comprehensive microstructural study by electrostatic spray deposition.* Solid State Ionics, 2008. **179**(33-34): p. 1921-1928.
59. Nomura, H., et al., *Fabrication of YSZ electrolyte using electrostatic spray deposition (ESD): I - a comprehensive parametric study.* Journal of Applied Electrochemistry, 2005. **35**(1): p. 61-67.
60. Neagu, R., et al., *Initial stages in zirconia coatings using ESD.* Chemistry of Materials, 2005. **17**(4): p. 902-910.
61. Yuan, F.L., et al., *Preparation of zirconia and yttria-stabilized zirconia (YSZ) fine powders by flame-assisted ultrasonic spray pyrolysis (FAUSP).* Solid State Ionics, 1998. **109**(1-2): p. 119-123.
62. Charojrochkul, S., K.L. Choy, and B.C.H. Steele, *Flame assisted vapour deposition of cathode for solid oxide fuel cells. 1. Microstructure control from processing parameters.* Journal of the European Ceramic Society, 2004. **24**(8): p. 2515-2526.
63. Setoguchi, T., et al., *Application of the Stabilized Zirconia Thin-Film Prepared by Spray Pyrolysis Method to Sofc.* Solid State Ionics, 1990. **40-1**: p. 502-505.
64. D. Perednis, O.W., S.E. Pratsinis, L.J. Gauckler, *Morphology and deposition of thin yttria-stabilized zirconia films using spray pyrolysis.* Thin Solid Films, 2005. **474**: p. 84-95.
65. I., M.Y.H.M.Y., *Growth of yttria stabilized zirconia thin films by metallo-organic, ultrasonic spray pyrolysis* Thin Solid Films, 1999 **340**: p. 72-76.

66. A. Furusaki, H.K., R. Furuichi, *Perovskite-type lanthanum chromium-based oxide films prepared by ultrasonic spray pyrolysis.* J. Mater. Sci, 1995. **30**: p. 2829-2834.

67. Wang S, W.W., Liu Q, Zhang M, Qian Y, *Preparation and characterization of cerium (IV) oxide thin films by spray prolysis method* Solid State Ionics, 2000. **133**: p. 211-215.

68. Peng, Z.Y. and M.L. Liu, *Preparation of dense platinum-yttria stabilized zirconia and yttria stabilized zirconia films on porous La0.9Sr0.1MnO3 (LSM) substrates.* Journal of the American Ceramic Society, 2001. **84**(2): p. 283-288.

69. Jia, L., et al., *Preparation of YSZ film by EPD and its application in SOFCs.* Journal of Alloys and Compounds, 2006. **424**(1-2): p. 299-303.

70. Matsuda, M., et al., *Direct EPD of YSZ electrolyte film onto porous NiO-YSZ composite substrate for reduced-temperature operating anode-supported SOFC.* Electrochemical and Solid State Letters, 2005. **8**(1): p. A8-A11.

71. Hayashi, K., et al., *La1-xSrxMnO3-YSZ composite film electrodes prepared by metal-organic decomposition for solid oxide fuel cells.* Materials Science and Engineering B-Solid State Materials for Advanced Technology, 1997. **49**(3): p. 239-242.

72. D.T. Morelli, A.M.M., J.V. Mantese, A.L. Micheli, *Magnetocaloric properties of doped lanthanum manganite films* Journal of Applied Physics 1996. **79**(1): p. 373 - 375

73. Zha, S.W., Y.L. Zhang, and M.L. Liu, *Functionally graded cathodes fabricated by sol-gel/slurry coating for honeycomb SOFCs.* Solid State Ionics, 2005. **176**(1-2): p. 25-31.

74. Barbucci, A., et al., *Impedance analysis of oxygen reduction in SOFC composite electrodes.* Electrochimica Acta, 2006. **51**(8-9): p. 1641-1650.

75. Mauvy, F., et al., *Oxygen electrode reaction on Nd2NiO4+delta cathode materials: impedance spectroscopy study.* Solid State Ionics, 2003. **158**(1-2): p. 17-28.

76. Yoon, S.P., et al., *Performance of anode-supported solid oxide fuel cell with La0.85Sr0.15MnO3 cathode modified by sol-gel coating technique.* Journal of Power Sources, 2002. **106**(1-2): p. 160-166.

77. Chiba, R., et al., *A study of cathode materials for intermediate temperature SOFCs prepared by the sol-gel method.* Solid State Ionics, 2004. **175**(1-4): p. 23-27.

78. Song, H.S., et al., *Electrochemical and microstructural characterization of polymeric resin-derived multilayered composite cathode for SOFC.* Journal of Power Sources, 2005. **145**(2): p. 272-277.

79. Hsu, C.S. and B.H. Hwang, *Microstructure and properties of the La0.6Sr0.4Co0.2Fe0.8O3 cathodes prepared by electrostatic-assisted ultrasonic spray pyrolysis method.* Journal of the Electrochemical Society, 2006. **153**(8): p. A1478-A1483.

80. Hart, N.T., et al., *Functionally graded cathodes for solid oxide fuel cells.* Journal of Materials Science, 2001. **36**(5): p. 1077-1085.

81. Hart, N.T., et al., *Functionally graded composite cathodes for solid oxide fuel cells.* Journal of Power Sources, 2002. **106**(1-2): p. 42-50.

82. Jiang, S.P., *A review of wet impregnation - An alternative method for the fabrication of high performance and nano-structured electrodes of solid oxide fuel cells.* Materials Science and Engineering a-Structural Materials Properties Microstructure and Processing, 2006. **418**(1-2): p. 199-210.

83. Hori, M., et al., *Evaluation of electrode performances of single-chamber solid oxide fuel cells.* Electroceramics in Japan Viii, 2005. **301**: p. 155-158.

84. Dusastre, V. and J.A. Kilner, *Optimisation of composite cathodes for intermediate temperature SOFC applications.* Solid State Ionics, 1999. **126**(1-2): p. 163-174.

85. H. Zhao, L.H.H., L. P. Sun, L. J. Yu, S. Gao, J. G. Zhao, *Preparation, Chemical Stability and Electrochemical Properties of LSCF-CBO Composite Cathodes.* Materials Chemistry and Physics, 2004. **88**(1): p. 160-166.

86. Beckel, D., et al., *Electrochemical performance of LSCF based thin film cathodes prepared by spray pyrolysis.* Solid State Ionics, 2007. **178**(5-6): p. 407-415.

87. Bi, Z.H., et al., *Electrochemical evaluation of La0.6Sr0.4CoO3-La0.45Ce0.55O2 composite cathodes for anode-supported La0.45Ce0.55O2-La0.9Sr0.1Ga0.8Mg0.2O2.85 bilayer electrolyte solid oxide fuel cells.* Solid State Ionics, 2005. **176**(7-8): p. 655-661.

88. R, M.J., ed. *Impedance Spectroscopy- Emphasizing Solid Materials and Systems*. 1987, John Wiley & Sons, New York

89. Huang, Q.A., et al., *A review of AC impedance modeling and validation in SOFC diagnosis.* Electrochimica Acta, 2007. **52**(28): p. 8144-8164.

90. Y. L. Yang, C.L.C., S. Y. Chen, C. W. Chu, and A. J. Jacobson, *Impedance studies of oxygen exchange on dense thin film electrodes of La0.5Sr0.5CoO3-delta.* J. Electrochem. Soc., 2000. **147**: p. 4001-4007.

91. Baumann, F.S., et al., *Strong performance improvement of La0.6Sr0.4Co0.8Fe0.2O3-delta SOFC cathodes by electrochemical activation.* Journal of the Electrochemical Society, 2005. **152**(10): p. A2074-A2079.

92. Cole, K.S.C.a.R.H., *Dispersion and absorption in dielectrics.* J. Chem. Phys., 1941. **9**: p. 341-351.

93. Chassaing, E., Sapoval, B., Daccord, G. and Lenormand, R., *Experimental Study of the impedance of blocking quasi-fractal and rough electrodes.* Journal of Electroanalytical Chemistry, 1990. **279**: p. 67

94. Pell, W.G., Zolfaghari, A. and Conway, B.E., *Capacitance of the Double-Layer at Polycrystalline Pt Electrodes Bearing a Surface Oxide Film.* Journal of Electroanalytical Chemistry, 2002. **532**(1-2): p. 13-23.

95. Hamann, C.H., Hamnett, A. and Vielstich, W., ed. *Electrochemistry*. 1 st ed. ed. 1998, Wiley-VCH, Weinheim.

96. Messing, G.L. and W.T. Minehan, *Synthesis of Ceramic Powders from Metal Alkoxides.* Nippon Seramikkusu Kyokai Gakujutsu Ronbunshi-Journal of the Ceramic Society of Japan, 1991. **99**(10): p. 1036-1046.

97. Messing, G.L., S.C. Zhang, and G.V. Jayanthi, *Ceramic Powder Synthesis by Spray-Pyrolysis.* Journal of the American Ceramic Society, 1993. **76**(11): p. 2707-2726.

98. Zhang, S.C. and G.L. Messing, *Solid Particle Formation during Spray Pyrolysis.* Ceramic Powder Science Iii, 1990. **12**: p. 49-57

995.

99. LANG, R.J., *Ultrasonic Atomization of Liquids* THE JOURNAL OF THE ACOUSTICAL SOCIETY OF AMERICA 1962. **34**(1): p. 6-8.

100. HSUAN-FU YU, W.-H.L., *Evaporation of solution droplets in spray pyrolysis* Inf. J. Hear Mass Transfer. , 1997. **41**(8-9): p. 993-1001.

101. Kikuo Okuyama, I.W.L., *Preparation of nanoparticles via spray route.* Chemical Engineering Science, 2003. **58**: p. 537–547.

102. Kakihana M, Y.M., *Synthesis and characteristics of complex multicomponent oxides prepared by polymer complex method.* BULLETIN OF THE CHEMICAL SOCIETY OF JAPAN 1999. **72**(7): p. 1427-1443

103. S. Brunauer, P.H.E., E. Teller, *Adsorption of gases in multimolecular layers.* Journal of the American Chemical Society, 1938. **60**: p. 309.

104. W, M., *Relative zeta functions, relative determinants and scattering theory.* Communications in Mathematical Physics, 1998. **192** (2): p. 309-47.

105. J, L., ed. *Fundamentals of interface and colloid science*. 1995.

106. Berne, P., ed. *Dynamic Light scattering*. 1975, John Wiley.

107. Noel A. Clark, J.H.L., and George B. Benedek *A Study of Brownian Motion Using Light Scattering* American Journal of Physics, 1970. **38**(5): p. 563.

108. Mineshige, A., et al., *Preparation of dense electrolyte layer using dissociated oxygen electrochemical vapor deposition technique.* Solid State Ionics, 2004. **175**(1-4): p. 483-485.

109. Zhou, W., et al., *Barium- and strontium-enriched (Ba0.5Sr0.5)(1+x)Co0.8Fe0.2O3-delta oxides as high-performance cathodes for intermediate-temperature solid-oxide fuel cells.* Acta Materialia, 2008. **56**(12): p. 2687-2698.

110. P. Gordes, N.C., E. J. Jensen and J. Villadsen, *Synthesis of perovskite-type compounds by drip pyrolysis.* Journal of Materials Science, 1995. **30**(4): p. 1053-1058.

111. S.A. Robbins, R.G.R., B.J. Weddle, T.R. Maull, P.K. Gallagher, *Some observations on the use of strontium carbonate as a temperature standard for DTA.* Thermochimica Acta, 1995. **269-270**: p. 43-49.

112. Basahel, S.N., *Kinetic analysis of thermal decomposition reactions. VII. Effect of radiation and doping on the thermal decomposition of BaC0,-TiO, and SrC0,-TiO, crystalline mixtures* Canadian Journal of Chemistry, 1992. **70**: p. 888.

113. P.K. Roy, J.B., *Formation of SrTiO3 from Sr-oxalate and TiO2.* Materials Research Bulletin, 2005. **40**: p. 599.

114. E. Jansen, W.S.a.G.W., *R Values in Analysis of Powder Diffraction Data using Rietveld Refinement.* J. Appl. Cryst., 1994. **27**: p. 492-496.

115. Charlesworth, D.H.a.M., *Evaporation from drops containing dissolved solids.* AIChE. J.,, 1960. **6**: p. 9-23.

116. H.-F. YU, W.-H.L., *Evaporation of solution droplets in spray pyrolysis* Inf. J. Hear Mass Transfer. , 1998. **41**(Nos 8-9): p. 993-1001.

117. R, L., *"Ultrasonic Atomization of Liquids.* J . Acoust. Soc. Am., 1952. **34**: p. 68.

118. Hinds, G., ed. *Aerosol Technology.* 1982, Wiley: New York.

119. Fuchs, N.A., ed. *Evaporafion and Droplet Growth in Gaseous Media.* 1959, Pergamon Press: New York.

120. C. Xia, Y.Z.a.M.L., *LSM-GDC Composite Cathodes Derived from a Sol-Gel Process, Effect of Microstructure on Interfacial Polarization Resistance.* Electrochemical and Solid State Letters, 2003. **6**(12): p. A290-A292.

121. Adler, S.B., *Factors governing oxygen reduction in solid oxide fuel cell cathodes.* Chemical Reviews, 2004. **104**(10): p. 4791-4843.

122. Barbucci, A., et al., *Characterisation of composite SOFC cathodes using electrochemical impedance spectroscopy. Analysis of Pt/YSZ and LSM/YSZ electrodes.* Electrochimica Acta, 2002. **47**(13-14): p. 2183-2188.

123. Kim, J.D., et al., *Characterization of LSM-YSZ composite electrode by ac impedance spectroscopy.* Solid State Ionics, 2001. **143**(3-4): p. 379-389.

124. J.H. Kim, R.H.S., J.H. Kim, T.H. Lim, Y.K. Sun, D.R. Shin, J, *Co-synthesis of nano-sized LSM-YSZ composites with enhanced electrochemical property* Journal of Solid State Electrochem., 2007. **11**(10): p. 1385.

125. J.D. Kim, e.a., *Characterization of LSM–YSZ composite electrode by ac impedance spectroscopy.* Solid State Ionics, 2001. **143**: p. 379.

126. Xu, X.Y., et al., *LSM-SDC electrodes fabricated with an ion-impregnating process for SOFCs with doped ceria electrolytes.* Solid State Ionics, 2006. **177**(19-25): p. 2113-2117.

127. J Q Li, P.X., *Fabrication and characterisation of La0.8Sr0.2MnO3/metal interfaces for application in SOFCs* Journal of the European Ceramic Society, 2001. **21**(5): p. 659-668.

128. Steele, B.C.H., *Appraisal of Ce1-yGdyO2-y/2 electrolytes for IT-SOFC operation at 500 degrees C.* Solid State Ionics, 2000. **129**(1-4): p. 95-110.

129. S. Wang, Y.J., Y. Zhang, J. Yan, W. Li, *Promoting effect of YSZ on the electrochemical performance of YSZ+LSM composite electrodes.* Solid State Ionics, 1998. **113-115**: p. 291.

130. Tsuneyoshi, K., et al., *Kinetic-Studies on the Reaction at the La0.6ca0.4mno3/Ysz Interface, as an Sofc Air Electrode.* Solid State Ionics, 1989. **35**(3-4): p. 263-268.

131. Feighery, A.J. and J.T.S. Irvine, *Effect of alumina additions upon electrical properties of 8 mol.% yttria-stabilised zirconia.* Solid State Ionics, 1999. **121**(1-4): p. 209-216.

132. P. Mondal, H.H., A. Klein, W. Jaegermann, *Enhanced specific grain boundary conductivity in nanocrystalline Y2O3-stabilized zirconia* Solid State Ionics, 1999. **118**: p. 331.

133. Jorgensen, M.J., et al., *Effect of sintering temperature on microstructure and performance of LSM-YSZ composite cathodes.* Solid State Ionics, 2001. **139**(1-2): p. 1-11.

134. M.C. Brant, T.M., L. Dessemond, R.Z. Domingues, *Electrical degradation of porous and dense LSM/YSZ interface* Solid State Ionics, 2006. **177**(9-10): p. 915-921.

135. Jiang, S.P., *A comparison of O2 reduction reactions on porous (La,Sr)MnO3 and (La,Sr)(Co,Fe)O3 electrodes.* 2002. **146**(1-2): p. 1-22.

136. Suzuki, S., H. Uchida, and M. Watanabe, *Interaction of samaria-doped ceria anode with highly dispersed Ni catalysts in a medium-temperature solid oxide fuel cell during long-term operation.* Solid State Ionics, 2006. **177**(3-4): p. 359-365.

137. S.B. Adler, J.A.L., B.C.H. Steele, *Electrode Kinetics of Porous Mixed-Conducting Oxygen Electrodes.* J. Electrochem. Soc., 1996. **143**(11): p. 3554-3564.

138. Adler, S.B., *Mechanism and kinetics of oxygen reduction on porous La 1-x Sr x CoO 3-δ electrodes.* Solid State Ionics, 1998. **111**: p. 125–134.

139. Yoon, S.P.N., S. W.; Kim, S.-G.; Hong, S.-A.; Hyun, S.-H, *Characteristics of cathodic polarization at Pt/YSZ interface without the effect of electrode microstructure* Journal of Power Sources, 2003. **115**: p. 27.

140. Koyama, M.W., C. J.; Masuyama, T.; Otomo, J.; Fukunaga, H.; Yamada, K.; Eguchi, K.; Takahashi, H., *The mechanism of porous Sm0.5Sr0.5CoO3 cathodes used in solid oxide fuel cells.* J. Electrochem. Soc., 2001. **148**: p. A795.

141. Tsai, T.P., E. Perry, and S. Barnett, *Low-temperature solid-oxide fuel cells utilizing thin bilayer electrolytes.* Journal of the Electrochemical Society, 1997. **144**(5): p. L130-L132.

142. Esquirol, A., J. Kilner, and N. Brandon, *Oxygen transport in La0.6Sr0.4Co0.2Fe0.8O3-delta/Ce0.8Ge0.2O2-x composite cathode for IT-SOFCs.* Solid State Ionics, 2004. **175**(1-4): p. 63-67.

143. Steele, B.C.H., K.M. Hori, and S. Uchino, *Kinetic parameters influencing the performance of IT-SOFC composite electrodes.* Solid State Ionics, 2000. **135**(1-4): p. 445-450.

144. Sirman J. D., K.J.A., *Surface exchange properties of Ce0.9Gd0.1O2-x coated with La1-xSrxFeyCo1-yO3-δ.* J. Electrochem. Soc., 1996. **143**: p. L229-L231.

145. Shao, Z.P. and S.M. Haile, *A high-performance cathode for the next generation of solid-oxide fuel cells.* Nature, 2004. **431**(7005): p. 170-173.

146. Lee, S., et al., *Ba0.5Sr0.5Co0.8Fe0.2O3-delta (BSCF) and La0.6Ba0.4Co0.2Fe0.8O3-delta (LBCF) cathodes prepared by combined citrate-EDTA method for IT-SOFCs.* Journal of Power Sources, 2006. **157**(2): p. 848-854.

147. Hebner, T.R., et al., *Ink-jet printing of doped polymers for organic light emitting devices.* Applied Physics Letters, 1998. **72**(5): p. 519-521.

148. Yu, J.S., et al., *Direct-Printed Organic Thin-Film Transistor Using PDMS Stamp and Low Viscosity Nanosilver Ink.* Journal of Nanoscience and Nanotechnology, 2008. **8**(10): p. 4940-4944.

149. Ueno, S., et al., *A new wettability-control technique for fabricating color OLED panels by an ink-jet-printing method.* Journal of the Society for Information Display, 2011. **19**(1): p. 87-93.

150. Park, B.K., et al., *Direct writing of copper conductive patterns by ink-jet printing.* Thin Solid Films, 2007. **515**(19): p. 7706-7711.

151. Gamerith, S., et al., *Direct ink-jet printing of Ag-Cu nanoparticle and Ag-precursor based electrodes for OFET applications.* Advanced Functional Materials, 2007. **17**(16): p. 3111-3118.

152. Cui, W.J., et al., *Gold nanoparticle ink suitable for electric-conductive pattern fabrication using in ink-jet printing technology.* Colloids and Surfaces a-Physicochemical and Engineering Aspects, 2010. **358**(1-3): p. 35-41.

153. Hong, S.J., Y.H. Kim, and J.I. Han, *Development of ultrafine indium tin oxide (ITO) nanoparticle for ink-jet printing by low-temperature synthetic method.* Ieee Transactions on Nanotechnology, 2008. **7**(2): p. 172-176.

154. Yu, J., et al., *Preparation of Indium Tin Oxide Inks for Electrically Conductive Transparent Oxide Film with Ink-Jet Printing Method.* Molecular Crystals and Liquid Crystals, 2010. **519**: p. 134-140.

155. Sahner, K. and H.L. Tuller, *Novel deposition techniques for metal oxide: Prospects for gas sensing.* Journal of Electroceramics, 2010. **24**(3): p. 177-199.

156. Pullar, R.C., et al., *Manufacture and measurement of combinatorial libraries of dielectric ceramics - Part I: Physical characterisation of Ba1-xSrxTiO3 libraries.* Journal of the European Ceramic Society, 2007. **27**(13-15): p. 3861-3865.
157. Pullar, R.C., et al., *Manufacture and measurement of combinatorial libraries of dielectric ceramics - Part II. Dielectric measurements of Ba1-xSrxTiO3 libraries.* Journal of the European Ceramic Society, 2007. **27**(16): p. 4437-4443.
158. Wang, T.M. and B. Derby, *Ink-jet printing and sintering of PZT.* Journal of the American Ceramic Society, 2005. **88**(8): p. 2053-2058.
159. Zhao, X., et al., *Ink-jet printing of ceramic pillar arrays.* Journal of Materials Science, 2002. **37**(10): p. 1987-1992.
160. Ainsley, C., N. Reis, and B. Derby, *Freeform fabrication by controlled droplet deposition of powder filled melts.* Journal of Materials Science, 2002. **37**(15): p. 3155-3161.
161. Shevchenko, A.V., et al., *Functional graded materials based on ZrO2 and Al2O3. Production methods.* Powder Metallurgy and Metal Ceramics, 2003. **42**(3-4): p. 145-153.
162. Taylor, A.D., et al., *Inkjet printing of carbon supported platinum 3-D catalyst layers for use in fuel cells.* Journal of Power Sources, 2007. **171**(1): p. 101-106.
163. Young, D., et al., *Ink-jet printing of electrolyte and anode functional layer for solid oxide fuel cells.* Journal of Power Sources, 2008. **184**(1): p. 191-196.

Danksagung

Ganz herzlich bedanken möchte ich mich bei Herrn Prof. Dr.-Ing. Horst Hahn, da er mir eine äußerst interessante und spannende Zeit als Doktorand an der TU Darmstadt ermölichte. Ein Höchstmaß an Freiheiten und das mir entgegengebrachte Vertrauen haben dazu beigetragen, mich für meine wissenschaftliche Arbeit zu motivieren.

Ferner möchte ich mich bei Frau Prof. Christina Roth für die Übernahme des Korreferates bedanken.

Ganz besonders möchte ich mich bei Herrn Prof. Jürgen Janek bedanken, der mich mit seinen Anregungen und Diskusionen motiviert hat.

Ein besonderer Dank gebührt allen, die mich bei verschiedenen Messungen unterstützt haben. Es sind an dieser Stelle zu nennen, Dr. Christiane Brockmann (ICP-OES), Dipl.-Ing. Claudia Fasel (DTA-TGA), Dr. Christian Kübel (TEM), Dr. Ruzica Djenadic (Zeta-Potential und DLS). In diese Reihe gehören auch Werkstattleiter Jochen Korzer und sein Team, besonders Herr Michael Weber, der eine hervorragende Unterstützung bei der Konstruktion der Messzelle für Hoch Temperatur Impedanz Spektroskopie geleistet hat.

Für die unzähligen kleinen und großen Hilfen unter Kollegen bedanke ich mich bei allen Mitgliedern des Gemeinschaftslabors Nanomaterialien, mit denen ich zusammen arbeiten durfte. Im einzelnen sind dies Dipl.-Ing. Sebastian Gottschalk, Dr. Thorsten Enz, Dr. Jens Suffner und aus anderen Fachgebiete, Dipl.-Ing. Mehrdad Baghaie Yazdi (Dünne Schichten), Dipl.-Ing. Stefan Schmid (Oberflächenforschung) und natürlich Renate Hernichel, die sich um alle nicht wissenschaftlichen Angelegenheiten gekümmert hat. Bei allen weiteren Arbeitskollegen und Freunden bedanke ich mich für das überaus angenehme Arbeitsklima und ihre Hilfsbereitschaft bei allen großen und kleinen Problemen. Unsere gemeinsame Zeit wird mir in guter Erinnerung bleiben.

Ganz Herzlich möchte ich mich bei Herrn Dr. Mohammad Ghafari für seine ununterbrochene moralische Unterstützung während meriner Promostionszeit bedanken.

Nicht zuletzt möchte ich meiner Familie besonders herzlich für die großartige Unterstützung in allen Lebenslagen danken. Ihr habt mir immer den nötigen Rückhalt und liebevolle Geduld entgegengebracht, vor allem in den anstrengenden und stressigen Phasen dieser Arbeit.

Curriculum Vitae

2009-2012	**Research Assistance** Joint Research Laboratory for Nanomaterials/ TU Darmstadt Institute for Nanotechnology/ Karlsruhe Institute for Technology EU Project: Materials for High Energy Accumulators in Traction and Tools (MAHEATT)
2006-2009	**PhD studies in Material Science** Joint Research Laboratory for Nanomaterials/ TU Darmstadt Institute for Nanotechnology/ Karlsruhe Institute for Technology Funded by Center for Functional Nanomaterials (CFN), Deutsche Forschungsgemeinschaft (DFG)
2002 – 2005	**MSc in Material Science (Metallurgical Engineering)** Iran University of Science and Technology (Tehran-Iran)
1997-2002	**BSc in Material Science and engineering** Iran University of Science and Technology (Tehran-Iran)

Publications

- A. J. Darbandi, Horst Hahn, "Nanoparticulate cathode films for low temperature SOFC applications with high electrochemical activity", Solid State Ionics 180 (2009) 1379-1387
- A. J. Darbandi, Thorsten Enz, Horst Hahn, "Synthesis and Characterization of Nanoparticulate Films for Intermediate Temperature Solid Oxide Fuel Cells", Solid State Ionics 180 (2009) 424-430
- A. Mishra, A. J. Darbandi, P. M. Leufke, R. Kruk, H. Hahn, "Reversible tuning of curie temperature in electrolyte gated LSMO nanoparticles", Submitted to Physical Review B
- D. J. Babu, A. J. Darbandi, J. Suffner, S.S. Bhattacharya, Horst Hahn, "Flame spray synthesis of nano lanthanum strontium manganite for solid oxide fuel cell applications ", Transactions of Indian The Institute of Metals, Vol. 64, Iss. 1-2, P 181-184 (2011)
- P. Nisha , S. S. Pillai, A. J. Darbandi, A. Misra, K. G. Suresh, M. R. Varma, H. Hahn,"Magnetism and magnetocaloric effect in nanocrystalline $La_{0.67}Ca_{0.33}Mn_{0.9}V_{0.1}O_3$ synthesized by nebulized spray pyrolysis" Journal of Physics D-Applied Physics, 43 (2010) 135001
- I. Stijepovic, A. J. Darbandi, V. V. Srdic, "Conductivity of doped LaGaO3 prepared by citrate sol-gel method", Journal of Optoelectronics and Advanced Materials, vol.12 [5] (2010) 1098-1104.

- Y. Ivanisenko, A. J. Darbandi, S. Dasgupta, R. Kruk and H. Hahn, "Bulk Nanostructured Materials: Non-Mechanical Synthesis", Advanced Engineering Materials 2010, 12, No. 8, 666-676

- S. Schmid, A. J. Darbandi, L. Konrad, R. Hausbrand, H. Hahn, W. Jaegermann, "Characterization of LiNi0.33Mn0.33Co0.33O2 thin films deposited by Ultrasonic Nebulized Chemical Vapor Deposition as cathode material for lithium ion batteries, to be submitted.

Conferences

- A. J. Darbandi, H. Hahn, "Thin Film Cathodes for low temperature SOFC", European Materials Research Society (EMRS), Nice (France), 9-13 May 2011 (Oral Presentation)

- A.J. Darbandi, H. Hahn, "Nanoparticulate cathode thin films with high electrochemical activity for low temperature SOFC", Materials for Energy, Karlsruhe (Germany), 4-8 July, 2010 (Oral presentation).

- A.J. Darbandi, H. Hahn, "Nanoparticulate cathode films for low temperature SOFC applications", Deutsche Physikalische Gesellschaft, Dresden (Germany), 23-27 March, 2009 (Poster presentation).

- A.J. Mishra, A.J. Darbandi, R. Kruk, H. Hahn, "Electrostatic doping of strongly correlated systems", Deutsche Physikalische Gesellschaft, Dresden (Germany), 23-27 March, 2009 (Oral presentation).

- I. Stijepovic, N. Pavlovic, V. Srdic, A.J. Darbandi, H. Hahn, "Conductivity of doped $LaGaO_3$ prepared by citrate sol-gel method", Electroceramics XI, Manchester, September 2008 (Oral Presentation).

- A.J. Darbandi, H. Hahn, "Synthesis and Characterization of Nanocomposite LSCF-GDC Thin Film for Low Temperature Micro-SOFC Applications", 9th International Conference on Nanostructured Materials (NANO), Rio de Janeiro (Brazil), 1-6June, 2008 (Oral presentation).

- A.J. Darbandi, H. Hahn, "Synthesis and Characterization of Nanocrystalline Lanthanum Strontium Manganite via Spray Pyrolysis for Solid Oxide Fuel Cell Applications", The 7th Students' Meeting (SM 2007) - Processing and Application of Ceramics, Novi Sad (Serbia), 2007 (Oral presentation).

- A.J. Darbandi, H. Sieger, H. Hahn, "Nanopowder of Sr-doped Lanthanum Manganite via Spray Pyrolysis for SOFC Applications", DGM-Tag, Karlsruhe, Germany 2007(Poster presentation).

Azad Jaberi Darbandi
Wilhelm-Glässing-Strasse 19
64287 Darmstadt

21.02.2012

Eidesstattliche Erklärung

Hiermit erkläre ich an Eides statt, dass ich meine Dissertation selbstständig und nur mit den angegebenen Hilfsmitteln angefertigt habe. Ich habe bisher noch keinen Promotionsversuch unternommen.

Azad Darbandi